nature methods

Registered Report

https://doi.org/10.1038/s41592-023-01975-z

Quantitative assessment of near-infrared fluorescent proteins

Received: 9 August 2021

Accepted: 29 June 2023

Published online: 4 September 2023

Check for updates

Hanbin Zhang[1,2,3,6], Stavrini Papadaki[1,2,3,6], Xiaoting Sun[1,2,3], Xinyue Wang[4], Mikhail Drobizhev[5], Luxia Yao[1,2,3], Michel Rehbock[4], Reinhard W. Köster[4], Lianfeng Wu[1,2,3], Kazuhiko Namikawa[4] & Kiryl D. Piatkevich[1,2,3]

Recent progress in fluorescent protein development has generated a large diversity of near-infrared fluorescent proteins (NIR FPs), which are rapidly becoming popular probes for a variety of imaging applications. However, the diversity of NIR FPs poses a challenge for end-users in choosing the optimal one for a given application. Here we conducted a systematic and quantitative assessment of intracellular brightness, photostability, oligomeric state, chemical stability and cytotoxicity of 22 NIR FPs in cultured mammalian cells and primary mouse neurons and identified a set of top-performing FPs including emiRFP670, miRFP680, miRFP713 and miRFP720, which can cover a majority of imaging applications. The top-performing proteins were further validated for in vivo imaging of neurons in *Caenorhabditis elegans*, zebrafish, and mice as well as in mice liver. We also assessed the applicability of the selected NIR FPs for multicolor imaging of fusions, expansion microscopy and two-photon imaging.

Fluorescent proteins (FPs) quickly became ubiquitous tools for optical imaging after the cloning of the green FP (GFP) from jellyfish *Aequorea victoria* in 1992 (ref. 1). Expanding spectral diversity of FPs into the near-infrared (NIR) range (~650–900 nm) of the electromagnetic spectrum enabled new imaging capabilities ranging from multiplexed super-resolution imaging of live cells to whole-body in vivo imaging[2]. The red-shifted fluorescence of NIR FPs enables efficient excitation with standard red lasers (630–640 nm), widely used light sources in microscopy, to unlock the standard Cy5 filter set for FPs, which was previously used only for red-shifted dyes imaging[3–6]. Correspondingly, NIR FPs can be readily imaged with other conventional FPs such as GFPs and red FPs (RFPs), enabling multiplexed structural[6] and functional imaging[7–9]. Further development of monomeric NIR FPs enabled their application as fluorescent tags for subcellular structures in cultured cells under conventional[6,10] and super-resolution microscopy[11–13]. In addition, NIR FPs are particularly beneficial for in vivo imaging of model organisms due to reduced autofluorescence, low light scattering, and minimal absorbance of tissue at longer wavelengths[14,15]. The unique photophysical properties of NIR FPs make them compatible with multiphoton microscopy[16,17] and photoacoustic imaging, thus further increasing the utility of these probes for in vivo imaging of mammals. However, the majority of currently available NIR FPs are derived from bacteriophytochromes and cyanobacteriochromes, which utilize a linear tetrapyrrole biliverdin IXα as a chromophore[14]. This feature makes the fluorescence of bacteriophytochrome photoreceptor (BphP)-based NIR FPs dependent on the heme metabolism in host cells[6,8,18]. As a result, the performance of BphP-based NIR FPs in cultured cells and in vivo preparations cannot be predicted based on the in vitro characteristics measured on proteins purified from bacteria, which is the most common way to select FPs for an imaging experiment[6,13]. Furthermore, intracellular brightness of BphP-based NIR FPs in one cell type is not necessarily retained in another cell type[6]. Altogether, this creates a need to test multiple NIR FPs in a particular preparation before selecting the one suitable for the desired application. To assist end-users to select the right NIR FPs, we performed a careful side-by-side quantitative assessment of the most popular NIR

[1]School of Life Sciences, Westlake University, Hangzhou, Zhejiang, China. [2]Westlake Laboratory of Life Sciences and Biomedicine, Hangzhou, Zhejiang, China. [3]Institute of Basic Medical Sciences, Westlake Institute for Advanced Study, Hangzhou, Zhejiang, China. [4]Division of Cellular and Molecular Neurobiology, Zoological Institute, Technische Universität Braunschweig, Braunschweig, Germany. [5]Department of Microbiology and Cell Biology, Montana State University, Bozeman, MT, USA. [6]These authors contributed equally: Hanbin Zhang, Stavrini Papadaki. e-mail: kiryl.piatkevich@westlake.edu.cn

FPs in HEK cells and primary neurons, characterizing their intracellular brightness, photostability, oligomeric state, chemical stability and cytotoxicity. Furthermore, the top-performing NIR FPs were expressed in vivo in *Caenorhabditis elegans*, zebrafish and mice for a side-by-side comparison of intracellular brightness and photostability. In addition, the proteins with the highest performance were tested for multicolor imaging and validated for expansion microscopy (by quantifying fluorescence retention in cultured cells) and two-photon imaging (by measuring action cross-section spectra).

Results

Characterization of NIR FPs in cultured mammalian cells

To perform the quantitative assessment in mammalian cells, we selected 22 NIR FPs: 19 biliverdin IXα-binding FPs and three GFP-like FPs (Extended Data Table 1, see Supplementary Note 1 for the selection criteria). The selected NIR FPs span more than 70 nm of the visible spectrum, and thus they can be subdivided into two spectral groups matching the Cy5 or Cy5.5 filter set with red (630–640 nm) or NIR (680 nm) excitation lasers, respectively (see Methods for the exact specification of the Cy5 and Cy5.5 filters). In this study we also used the Cy5-LP filter (with a 664 nm long-pass emission filter that enables the collection of as much NIR fluorescence as possible) and the Cy5-BP filter (with a 679/41 nm narrow bandpass filter to improve spectral separation with the Cy5.5 filter), which are the two most common emission filters for red lasers on standard imaging set-ups. We used a wide-field microscope equipped with all three filter sets to characterize intracellular brightness and photostability of the selected NIR FPs expressed under the CAG promoter in cultured HEK cells and primary mouse neurons. Quantification of intracellular brightness was done by normalization of the NIR fluorescence by fluorescence of the GFP co-expressed via P2A self-cleavage peptide, given that this approach was characterized by superior performance for brightness normalization compared with other co-expression strategies such as IRES2 and direct fusion of two FPs (Supplementary Note 2, Supplementary Table 1 and Supplementary Fig. 1).

All proteins were evenly localized both in the cytoplasm and nucleus of HEK cells except for E2-Crimson, which was excluded from the nucleus due to its tetrameric state (Supplementary Fig. 2). In live cultured neurons the fluorescence of the NIR FPs was evenly distributed in the cytosol, individual dendrites and nucleus without any noticeable aggregation or non-specific localization except for iRFP682, which showed small puncta in neuropils in both the Cy5 and green channels (Supplementary Fig. 3). Quantification of intracellular brightness and photostability identified the brightest and most photostable NIR FPs in each channel when expressed in HEK cells and neurons (Fig. 1a–f, Extended Data Fig. 1 and Supplementary Table 3 for HEK cells, and Extended Data Fig. 2 and Supplementary Table 4 for neurons, also see Supplementary Table 2 and Supplementary Dataset 1 for detailed descriptive statistics and statistical analysis). Further analysis showed low correlation in the relative brightness of NIR FPs between HEK cells and primary neurons, characterized by linear regression coefficients of 0.09, 0.27 and 0.33 for the Cy5-LP, Cy5-BP and Cy5.5 channels, respectively (Supplementary Fig. 4). The most notable was the low relative brightness of GFP-like NIR FPs in neurons compared with HEK cells. For example, while mCardinal and E2-Crimson were the brightest FPs in the Cy5-LP channel in live HEK cells, they ranked only 15th and 11th, respectively, in cultured neurons. In contrast, the relative brightness of miRFP713 and miRFP720 was 3.6- and 3.4-fold higher in neurons than in HEK cells. The emiRFP670, miRFP670-2 and miRFP680 proteins exhibited consistent brightness in both cell types and were among the top five FPs in Cy5 channels (Fig. 1a and Extended Data Fig. 1). We also noted a low correlation of intracellular brightness and effective molecular brightness (Supplementary Fig. 4). Use of exogenous biliverdin IXα at 25 μM increased intracellular brightness of all biliverdin IXα-binding NIR FPs by, on average, twofold in HEK cells and fivefold in neurons (Extended Data Fig. 1 and Supplementary Table 3 for HEK cells and Extended Data Fig. 2 and Supplementary Table 4 for neurons). Given that we encountered situations in which some NIR FPs had a high NIR-to-green fluorescence ratio but at the same time low absolute NIR fluorescence intensity (for example, compare BDFP1.6 and emiRFP670 in Supplementary Figs. 2 and 3), we conducted additional quality control experiments using western blot analysis as well as mass spectrometry for selected NIR FPs. According to western blot results, cleavage efficiency was more than 90% while the molecular ratio of NIR FP to GFP varied from 1:3 to 1:1 for most of the constructs (the miRFP713-P2A-GFP construct was an outlier with a 6:1 ratio) (Supplementary Fig. 5). Mass spectrometry analysis showed multiple post-translation modifications of the selected NIR FPs (Supplementary Fig. 6). To verify whether high intracellular brightness was associated with increased cytotoxicity, we determined the fraction of apoptotic and dead HEK cells at 48 hours after transient transfection. The cytotoxicity of the top five brightest NIR FPs from three spectral channels was comparable to the negative control (dummy plasmid transfection), while mCardinal, E2-Crimson, iRFP670 and SNIFP produced an approximately 1.5-fold larger fraction of apoptotic cells than the negative control (Supplementary Table 5 and Supplementary Fig. 7). smURFP and miRFP2 produced the largest fraction of apoptotic cells (>5-fold than the control) in the test NIR FPs.

Photobleaching rates measured under matching light powers in the Cy5 and Cy5.5 channels were consistent between HEK cells and neurons for all NIR FPs, with linear regression coefficients of >0.94 (Supplementary Fig. 4). On average, photobleaching half-times in neurons were 20–40% longer than in HEK cells except for E2-Crimson, smURFP, BDFP1.8 and miRFP713, which were slightly less photostable in neurons than in HEK cells (Fig. 1b,e, also see Extended Data Fig. 1 and Supplementary Table 3 for HEK cells and Extended Data Fig. 2 and Supplementary Table 4 for neurons). There was a more than 22-fold difference in photobleaching rates between the least photostable E2-Crimson and the most photostable mRhubarb713 both in HEK cells and neurons. Interestingly, the intracellular brightness in HEK cells had a moderately negative correlation with photostability (Pearson's coefficients, −0.46 and −0.5 in the Cy5-LP and Cy5.5 channels, respectively), while brightness and photostability in neurons were not correlated (Pearson's coefficients, 0.06 and 0.27 in the Cy5-LP and Cy5.5 channels, respectively; Supplementary Fig. 4). Given that brightness and photostability are the major considerations for choosing FPs, we compared the overall performance of NIR FPs using the product of intracellular brightness and photostability, and then selected the five variants with the highest such products for each tested channel for further validation in vivo (Fig. 1c,f, Extended Data Figs. 1 and 2 and Supplementary Table 6).

Chemical fixation with paraformaldehyde (PFA) is widely used for biological sample preservation and FPs that retain bright and photostable fluorescence after PFA fixation would be beneficial for structural fluorescence imaging[19,20]. To assess the applicability of NIR FPs for imaging in chemically fixed samples, we measured their intracellular brightness, fluorescence retention and intracellular photostability in PFA-fixed HEK cells (Fig. 1g–i, Extended Data Fig. 3, Supplementary Table 7 and Supplementary Fig. 8). The top five NIR FPs by brightness in fixed HEK cells mainly overlapped with that in live HEK cells, except that mCardinal and miRFP670-2 were replaced by iRFP670 and miRFP720 (Fig. 1g). All biliverdin IXα-binding NIR FPs retained more than 60% of their fluorescence after fixation, with miRFP2 > BDFP1.8 > SNIFP > miRFP680 > smURFP being the most stable (Extended Data Fig. 3f). The GFP-like NIR FPs mNeptune2.5 and mCardinal appeared to be among the least stable, retaining only 45% and 26% of the fluorescence, respectively (Supplementary Table 7), while GFP preserved approximately 85% of its fluorescence. Photostability in fixed HEK cells was on average 30–34% higher than in live HEK cells (Fig. 1h and Supplementary Tables 3 and 7). To further validate the chemical stability of NIR FPs, we used the protein retention expansion microscopy protocol[21] to process HEK cells

https://doi.org/10.1038/s41592-023-01975-z

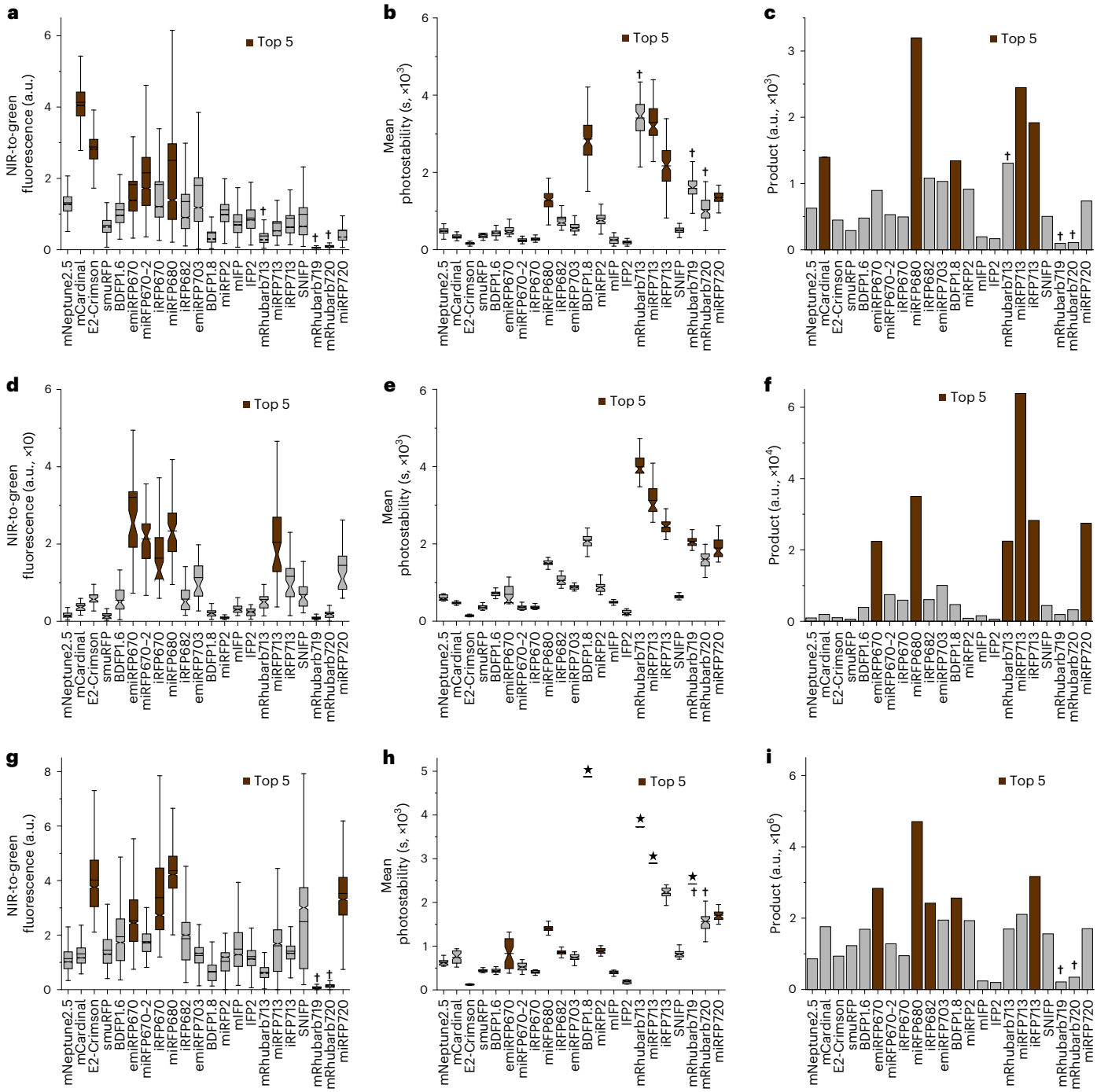

Fig. 1 | Quantitative characterization of NIR FPs in cultured mammalian cells. a, Normalized brightness of NIR FPs in live HEK cells imaged in the Cy5-LP channel ($n > 1{,}945$ cells for each NIR FP from three independent transfections). Brightness for each FP was normalized to the EGFP signal (used throughout the figure). Daggers (†) indicate signal-to-background ratio <2.0 throughout. **b**, Photobleaching half-times of NIR FPs in live HEK cells under Cy5 excitation ($n > 93$ cells for each NIR FP from four independent transfections). **c**, Single value product of mean brightness and mean photobleaching half-time in live HEK cells. **d**, Normalized brightness of NIR FPs in live neurons imaged in the Cy5-LP channel ($n > 44$ neurons for each NIR FP from two independent cultures). **e**, Photobleaching half-times of NIR FPs in live neurons under Cy5 excitation ($n > 41$ neurons for each NIR FP from two independent cultures). **f**, Single value product of mean brightness and mean photobleaching half-time in live neurons. **g**, Normalized brightness of NIR FPs in fixed HEK cells imaged in the Cy5-LP channel ($n > 1{,}974$ cells for each NIR FP from two independent transfections). **h**, Photobleaching half-times of NIR FPs in fixed HEK cells under Cy5 excitation ($n = 40$ cells for each NIR FP from two independent transfections). Stars (★) indicate photobleaching half-times estimated by extrapolation. **i**, Single value product of mean brightness and mean photobleaching half-time in fixed HEK cells. Excitation power for brightness imaging, 55 mW mm^{-2}; for photostability measurements in live HEK cells, 58 mW mm^{-2}; in live neurons and fixed HEK cells, 55 mW mm^{-2}. Box plots with notches: narrow part of notch, median; top and bottom of the notch, 95% confidence interval for the median; top and bottom horizontal lines, 25% and 75% percentiles for the data; whiskers extend 1.5-fold the interquartile range from the 25th and 75th percentiles; horizontal line, mean; outliers not shown but are included in all calculations and available in the source datasets. See **Statistics and Reproducibility**, Supplementary Table 2, Supplementary Data for detailed statistics and exact *P* values.

https://doi.org/10.1038/s41592-023-01975-z

Table 1 | Quantification of NIR FP monomeric state in live HeLa cells using OSER assay

Protein	MFI : NE MFI	Normal cells (%)	Product relative to miRFP720 (%)[g]
mNeptune2.5	4.4 ± 0.9[a]	76.0 ± 5.9[c]	34.1
mCardinal	3.3 ± 0.6	70.0 ± 2.4[d]	41.9
E2-Crimson	4.6 ± 0.3	1.9 ± 1.3[d]	0.8
smURFP	NA[b]	NA[e]	NA
BDFP1.6	2.4 ± 0.5[a]	74.7 ± 3.1[c]	61.5
emiRFP670	2.6 ± 0.2	72.4 ± 8.3[d]	55.0
miRFP670-2	1.9 ± 0.1	66.4 ± 6.2[d]	69.0
iRFP670	1.6 ± 0.1	68.7 ± 1.8[d]	84.8
miRFP680	1.8 ± 0.1[a]	78.7 ± 9.3[d]	86.4
iRFP682	2.3 ± 0.1	70.9 ± 3.5[d]	60.9
emiRFP703	2.1 ± 0.2	72.8 ± 4.7[c]	68.5
BDFP1.8	2.1 ± 0.1	60.8 ± 6.6[d]	57.2
miRFP2	NA[b]	80.5 ± 6.7[c]	NA
mIFP	NA[b]	NA[f]	NA
IFP2	NA[b]	86.5 ± 3.3[c]	NA
mRhubarb713	2.3 ± 1.1[a]	75.6 ± 9.9[c]	64.9
miRFP713	1.9 ± 0.1[a]	80.8 ± 5.6[d]	84.0
iRFP713	2.4 ± 1.8	48.5 ± 4.8[d]	39.9
SNIFP	2.8 ± 0.4[a]	69.8 ± 8.3[c]	49.2
mRhubarb719	NA[b]	NA[f]	NA
mRhubarb720	NA[b]	70.3 ± 8.1[c]	NA
miRFP720	1.6 ± 0.1	81.0 ± 5.6[d]	100

Data given as mean ± s.e.m. NA, not applicable. [a]Calculated using <10 cells due to few bright cells with whorls. [b]CytERM fusion is either too dim or mislocalized. [c]Calculated using 100–1,000 cells. [d]Calculated using >1,000 cells. [e]Less than 10 cells. [f]10–100 cells. [g]Calculated as the product of the reciprocal of the MFI: NE MFI value and the fraction of normal cells.

expressing emiRFP670, miRFP680, iRFP682, emiRFP703, BDFP1.8, miRFP713, iRFP713 and miRFP720, which possessed the highest product of absolute NIR fluorescence and photostability in the Cy5 and/or Cy5.5 channels (Fig. 1i and Extended Data Fig. 3d). The tested NIR FPs had a >3-fold lower fluorescence retention than GFP except for BDFP1.8, which preserved ~20% of its fixed fluorescence intensity versus 33% for GFP (Extended Data Fig. 3e,g,h). These results demonstrate that the biliverdin IXα-binding NIR FPs preserve brightness and photostability in PFA-fixed samples, although their chemical stability was limited in the expansion microscopy preparations.

The oligomeric state of NIR FPs was evaluated based on their performance in CytERM fusion in live HeLa cells. We calculated two parameters, the ratio of whorl structure mean fluorescent intensity (MFI) to nuclear envelope (NE) MFI (MFI : NE MFI), and the fraction of transfected cells without visible OSER (organized smooth endoplasmic reticulum) whorl structures, which were previously proposed for the quantification of the oligomerization tendency of FPs in live mammalian cells[22,23] (see Supplementary Figs. 9 and 10 for representative images). The top five proteins in intensity assay were miRFP720, iRFP670, miRFP680, miRFP670-2 and miRFP713, while in the percentage assay they were miRFP720, miRFP713, miRFP680, mNeptune2.5 and mRhubarb713 (Table 1). Several NIR FPs (smURFP, miRFP2, mIFP, IFP2, mRhubarb719 and mRhubarb720) were either too dim or did not form classical whorl structures and thus were excluded from further assessment. However, our final selection of monomeric NIR FPs was not based on either assay alone. The MFI : NE MFI ratio threshold set by Costantini et al. was based on the GFP-like proteins and thus may require additional validation for biliverdin IXα-binding FPs[23]. For example, in the present study emiRFP703 and BDFP1.8 scored the same mean MFI : NE MFI ratio of 2.1, even though emiRFP703 was characterized as a monomer through analytical centrifugation[13] and BDFP1.8 as a dimer through size-exclusion chromatography[24]. In another study using OSER assay for GFP-like FPs, Cranfill et al. set the threshold for the percentage of normal cells at 90%[22], which was not achieved by any of the tested NIR FPs in the present study. Moreover, we noted a low positive correlation between the fraction of normal cells and the MFI : NE MFI ratio ($r^2 = 0.33$; Supplementary Fig. 4). Therefore, we decided to use the product of both assays to select the most monomeric NIR FPs. According to these metrics, miRFP720, miRFP680, iRFP670, miRFP713 and miRFP670-2 were the top five monomeric NIR FPs (Table 1). To further validate the monomeric state of the selected NIR FPs we expressed them in fusions with β-actin, histone 2B, keratin, connexin-43 and α-tubulin in HeLa cells, which are often used for testing new FPs. These fusions showed overall correct localization except for connexin-43, which did not localize correctly with any NIR FPs; cytoplasmic fluorescence was observed for the α-tubulin fusions with iRFP670, miRFP670-2, miRFP713 and miRFP720 (Extended Data Fig. 4). The performance of the selected NIR FPs as tags for structural proteins was comparable to that of well-established monomeric GFP-like FPs, including mCherry, mRuby, mNeonGreen and so on,[25,26] suggesting that OSER assay was valid for biliverdin IXα-binding FPs.

In vitro characterization of selected NIR fluorescent proteins

The top-performing NIR FPs in neurons, namely emiRFP670, miRFP670-2, miRFP680, mRhubarb713, miRFP713, iRFP713 and miRFP720, were expressed in *Escherichia coli*, purified according to a standard protocol and used for spectroscopic and biochemical characterization in PBS at pH 7.4. The mCardinal protein, which was not among the best performers in neurons, was included as an additional control because it does not require biliverdin IXα. We measured absorbance and steady-state fluorescence spectra (Supplementary Fig. 11), extinction coefficients, quantum yields, fluorescence lifetime (Extended Data Table 2) and fluorescence pK_a (the pH at which fluorescence intensity drops to 50% of its maximum value; Supplementary Fig. 12). Overall, the obtained values matched those previously reported with some minor deviations (Extended Data Table 2). Extinction coefficients calculated using the Strickler–Berg equation[27] were on average 70% lower than those calculated based on the Soret band absorbance, although extinction coefficients for mCardinal measured using alkaline denaturation and calculated with the Strickler–Berg equation matched closely (Extended Data Table 2).

Previously we demonstrated that second-generation dimeric BphP-based NIR FPs can be used for dual-color multiphoton imaging using the standard titanium–sapphire laser[16,28]. To facilitate application of the top-performing NIR FPs for intravital multiphoton imaging we characterized their two-photon cross-section spectra in the range 800–1,300 nm (Extended Data Fig. 5). The recorded spectra had 7–10-fold larger absolute cross-sectional values at the Soret band (800–950 nm) than at the Q-band (1,100–1,300 nm), matching the spectral profiles of other BphP-based NIR FPs[16,28]. However, the absolute value of the cross-sections was approximately twofold smaller than our previously published data, which we attributed to the reduced value of two-photon absorption for the reference dye refined in the recent study[29] (Extended Data Table 2). Based on the recorded two-photon cross-section spectra the optimal two-photon excitation range for BphP-based NIR FPs was between 830 and 950 nm, which overlaps with the optimal wavelength for GFP.

Characterization in model organisms

Red-shifted spectra of biliverdin IXα-binding FPs are particularly beneficial for in vivo imaging due to low background autofluorescence,

reduced light scattering, and minimal absorbance of tissue in the NIR range of the spectrum. For quantitative assessment in vivo we expressed selected NIR FPs in neurons in mice, zebrafish and *C. elegans*, which are among the most popular model organisms in life science research. We also tested selected NIR FPs in liver in mice to evaluate tissue-specific variability of NIR FP performance. Given that the primary cell type for in vivo assessment was neurons, we chose to use all top five performing NIR FPs from three spectral channels (some proteins were among the best performing in more than one channel, resulting in a total of seven proteins) in neuronal culture, namely emiRFP670, miRFP670-2, miRFP680, mRhubarb713, miRFP713, iRFP713 and miRFP720 (Supplementary Table 4). Because the best-performing NIR FPs were BphP based, we included the GFP-like NIR FP mCardinal as a reference for biliverdin IXα availability in vivo. In addition, emiRFP2, an enhanced version of miRFP2 (ref. 30), was assessed in zebrafish.

To express selected NIR FPs in the cortex of mouse brain, we injected the rAAV2/9-CAG-NIR-FPs-P2A-GFP viruses into mouse brain at the neonatal stage and performed imaging of acute brain slices at 1 month, 2 months and 3 months after injection, and of fixed brain tissue at 1 month after injection. First, we acquired structural images of fixed brain slices from 1-month-old mice using confocal microscopy and qualitatively compared the co-localization of NIR FP and GFP fluorescence (Fig. 2a and Supplementary Fig. 13 for representative images at lower magnification). The emiRFP670 protein exhibited excellent localization in cortical neurons, enabling better visualization of small neuropils compared with GFP. The other NIR FPs provided a lower quality of neuropil visualization than GFP, with miRFP680 and miRFP713 showing significant aggregation. Minor aggregation in neuropils was observed for mCardinal and mRhubarb713. Moreover, miRFP680, mRhubarb713, miRF713, iRFP713 and miRFP720 exhibited noticeable nuclear accumulation, which was most prominent for miRFP713. Intracellular brightness measured at neuronal somas in the Cy5-LP channel achieved a maximum at the 2 month time point for all NIR FPs except for mRhubarb713 (Fig. 2b–d). The miRFP680 protein had superior brightness in both the Cy5-LP and Cy5-BP channels, outperforming other NIR FPs by ≥1.8-fold. In turn, miRFP720 was the brightest NIR FP in the Cy5.5 channel at the 1 month and 2 month time points, and miRFP713 at the 3 month time point (Extended Data Fig. 6 and Supplementary Table 8). The fluorescence of BphP-based NIR FPs was retained well in PFA-fixed brain tissue while mCardinal fluorescence diminished by ~4-fold, reminiscent of that measured in HEK cells (Fig. 2e and Extended Data Fig. 6). miRFP713 had superior photostability in both acute and fixed brain slices, however, the photostability of the brightest NIR FP, miRFP680, was reduced by sixfold upon PFA fixation. In contrast, the photostability of emiRFP670 was ~18-fold higher in fixed tissue than in live tissue (Fig. 2f,g, Extended Data Fig. 6 and Supplementary Table 9).

Despite their superior brightness and photostability, miRFP680 and miRFP713 were not optimal for neuron imaging in mice due to their poor neuronal labeling in vivo. To validate their performance in other cell types and tissues, we expressed selected NIR FPs in mouse liver using the same adeno-associated viruses (AAVs) as were used for expression in the brain. Quantification of brightness in live liver tissue showed a similar ranking by brightness to that observed in the cortical neurons at the 2 month time point, although the differences in relative brightness between the NIR FPs were less significant and mCardinal appeared to be the dimmest NIR FP (Extended Data Fig. 7 and Supplementary Table 8). Correspondingly, miRFP680 was the brightest NIR FP in the Cy5-LP and Cy5-BP channels, while miRFP720 was brightest in the Cy5.5 channel. Importantly, within the limitations of wide-field imaging in thick tissue, we did not observe accumulation of NIR FPs in the cell nucleus (Extended Data Fig. 7a).

Similar to mammals, the heme metabolism in zebrafish involves the formation of biliverdin IXα by the HMOX1a and HMOX1b enzymes homologous to heme oxygenase 1 (HO1)[31]. Furthermore, we previously demonstrated that the BphP-based NIR FPs can be visualized in zebrafish larvae without co-expression of recombinant HO1 (refs. 28,30). However, it is likely that biliverdin IXα concentration in zebrafish is a limiting factor for the intracellular brightness of BphP-based NIR FPs, because their fluorescence can be significantly enhanced by co-expression of HO1 (ref. 18). We therefore decided to investigate the effect of heterologous HO1 on intracellular brightness and photostability of BphP-based NIR FPs in zebrafish by co-expressing either functional wild-type HO1 (wtHO1) or its enzymatically inactive variant (HO1-H25A) together with each NIR FP, while mClover3 was used for brightness normalization. To enable co-expression of the proteins of interest across the nervous system in zebrafish larvae, we used expression constructs, which carried the genes of NIR FPs fused to P2A-mClover3 and wtHO1 or HO1-H25A under a bidirectional promoter controlled by the neuron-specific Gal4 transcription factor encoded in the same vector (Supplementary Fig. 14). The hindbrain and spinal cord regions of live zebrafish larvae at 4 days post-fertilization (dpf) were imaged in the Cy5-LP channel under a confocal scanning microscope to assess the intracellular brightness and photostability of NIR FPs in individual neurons (Fig. 3, see Supplementary Figs. 15 and 16 for dual-color images with mClover3). While all BphP-based FPs could be imaged in neurons when co-expressed with the inactive form of HO1, they were ~1.7–13-fold dimmer than mCardinal. Co-expression of wtHO1 enhanced the intracellular brightness of all BphP-based NIR FPs, and the most significant increase (≥2.5-fold) was observed for emiRFP670 and miRFP680, which were the two brightest NIR FPs, as well as for emiRFP2. By contrast, mRhubarb713, miRFP713 and iRFP713 showed the lowest intracellular brightness even when co-expressed with wtHO1 and were characterized by >4-fold and >8-fold lower relative brightness values in the hindbrain and spinal cord neurons, respectively, compared with mCardinal (Supplementary Table 10). All assessed NIR FPs, except for mRhubarb713, miRFP713 and iRFP713, had sufficient brightness and cytoplasmic distribution in both hindbrain and spinal cord neurons, further enabling visualization of their neurites. Furthermore, no aggregation was observed for any of the NIR FPs in neurons. Continuous confocal imaging of spinal cord neurons showed that the photostability of the BphP-based NIR FPs was ~1.7–2.9-fold higher when co-expressed with wtHO1 except for mRhubarb713 and emiRFP2, which were characterized by only an insignificant increase (<14%) in photostability with wtHO1 (Fig. 3e,f, see Supplementary Fig. 17 for representative images). The brightest NIR FP, miRFP680, exhibited limited photostability with a photobleaching half-time of ~87 s, which was almost threefold shorter than that of mCardinal, emiRFP670 and miRFP720, which are the next brightest NIR FPs. Based on the product of intracellular brightness and photostability, emiRFP670/wtHO1 was the best-performing NIR FP, followed by mCardinal and miRFP720/wtHO1, which were characterized by an approximately twofold lower product.

In contrast to mice and zebrafish, functional expression of BphP-based FPs in *C. elegans* requires a synthetic pathway for biliverdin IXα biosynthesis[30,32]. Therefore, we co-expressed the codon-optimized genes of the selected BphP-based NIR FPs with HO1 in neurons using extrachromosomal array expression systems. mNeonGreen, co-expressed from an independent plasmid, was used as a co-expression marker for NIR fluorescence normalization. The fluorescence of the NIR FPs was well co-localized with mNeonGreen (Supplementary Fig. 18) and was distributed evenly in neuronal cell bodies and processes without formation of fluorescent aggregates or puncta (Fig. 4a). While all tested NIR FPs were imageable in the Cy5-LP channel, miRFP680 showed superior brightness with an approximately 3–10-fold higher relative fluorescence than most of the other NIR FPs and was approximately 1.5-fold brighter than the second brightest NIR FP, emiRFP670 (Fig. 4b and Supplementary Table 11). The miRFP713 protein was the brightest in the Cy5.5 channel, outperforming iRFP713, mRhubarb713 and miRFP680 by 13%, 50% and 59%, respectively (Fig. 4c). The miRFP720, emiRFP670 and miRFP670-2 proteins were more than 3.5-fold dimmer than miRFP713,

https://doi.org/10.1038/s41592-023-01975-z

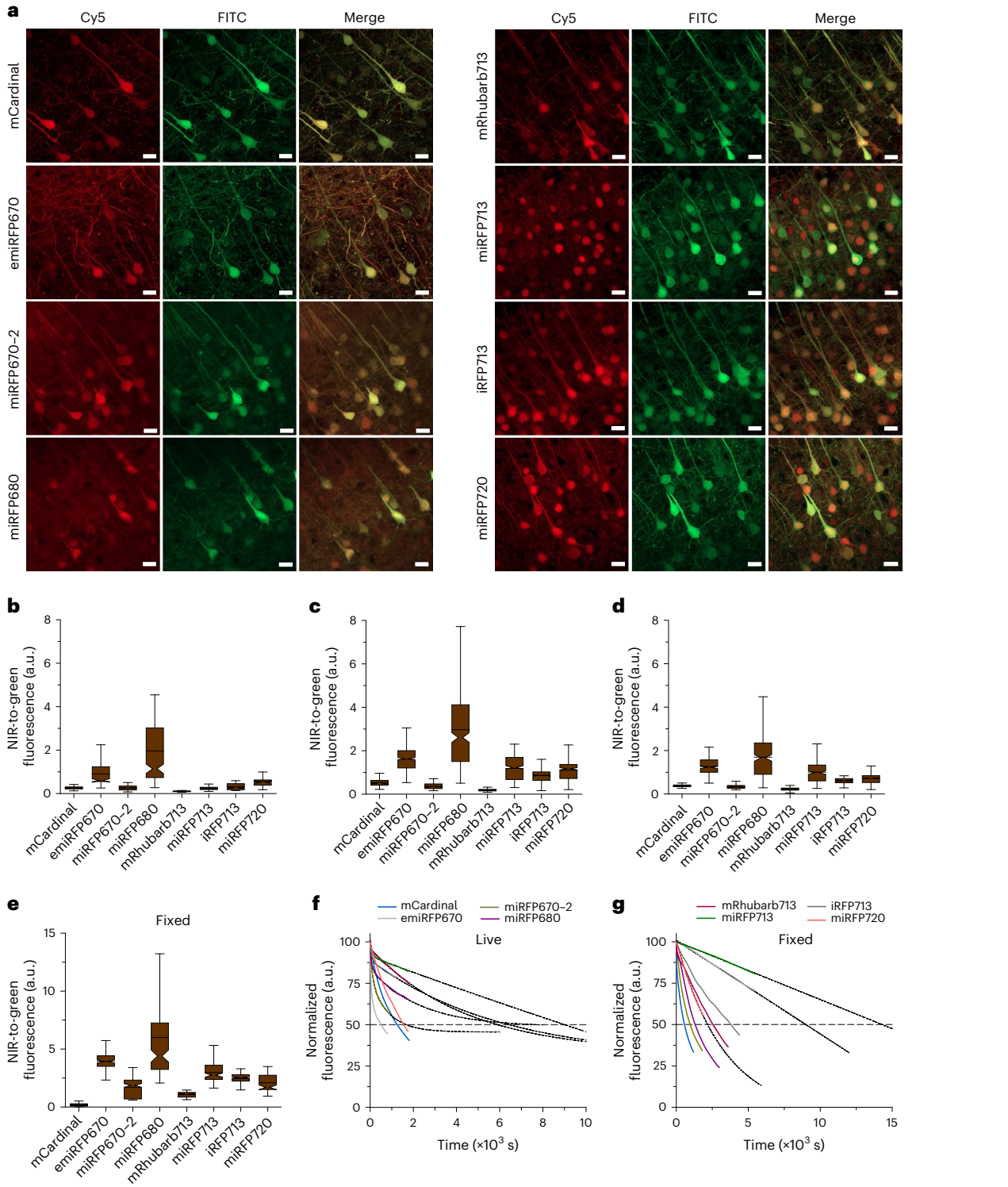

Fig. 2 | Quantitative characterization of the selected NIR FPs expressed in L2/3 cortical neurons in mouse brain tissue. a, Representative confocal fluorescence images of fixed brain slices expressing NIR-FPs-P2A-GFP ($n = 2$ slices from one or two mice for each protein). Imaging conditions, Cy5: excitation 639 nm, emission 655–735 nm; FITC: excitation 488 nm, emission 500–550 nm. To facilitate visual comparison of FP localization, the dynamic range was adjusted independently for each image and images were generated through maximum projection. Scale bars, 20 µm. **b**–**d**, Intracellular normalized brightness of NIR FPs imaged in acute brain slices from 1-month-old (**b**), 2-month-old (**c**) and 3-month old (**d**) mice in Cy5-LP channels (excitation power 55 mW mm^{-2}; $n \geq 100$ neurons from three mice for each protein at each time point). Brightness for each FP was normalized to the EGFP signal (here and in **e**). **e**, Intracellular normalized brightness of NIR FPs imaged in PFA-fixed brain slices from 1-month-old mice in Cy5-LP (excitation power 55 mW mm^{-2}; $n > 90$ neurons from two mice for each protein). **f**,**g**, Normalized photobleaching curves of NIR FPs measured in acute brain slices (**f**) and PFA-fixed brain slices (**g**) in Cy5-LP (excitation power 55 mW mm^{-2}; $n > 40$ neurons from two mice for each protein in each channel; solid lines, experimental data; short dashed line, extrapolation; dashed line, 50% of initial intensity). Fluorescence was normalized to the intensity value of the corresponding FP at $t = 0$ s. Box plots with notches: narrow part of notch, median; top and bottom of the notch, 95% confidence interval for the median; top and bottom horizontal lines, 25% and 75% percentiles for the data; whiskers extend 1.5-fold the interquartile range from the 25th and 75th percentiles; horizontal line, mean; outliers not shown but are included in all calculations and available in the source datasets. See Methods (**Statistics and Reproducibility** section) and Supplementary Data 1 for detailed descriptive statistics and exact *P* values.

https://doi.org/10.1038/s41592-023-01975-z

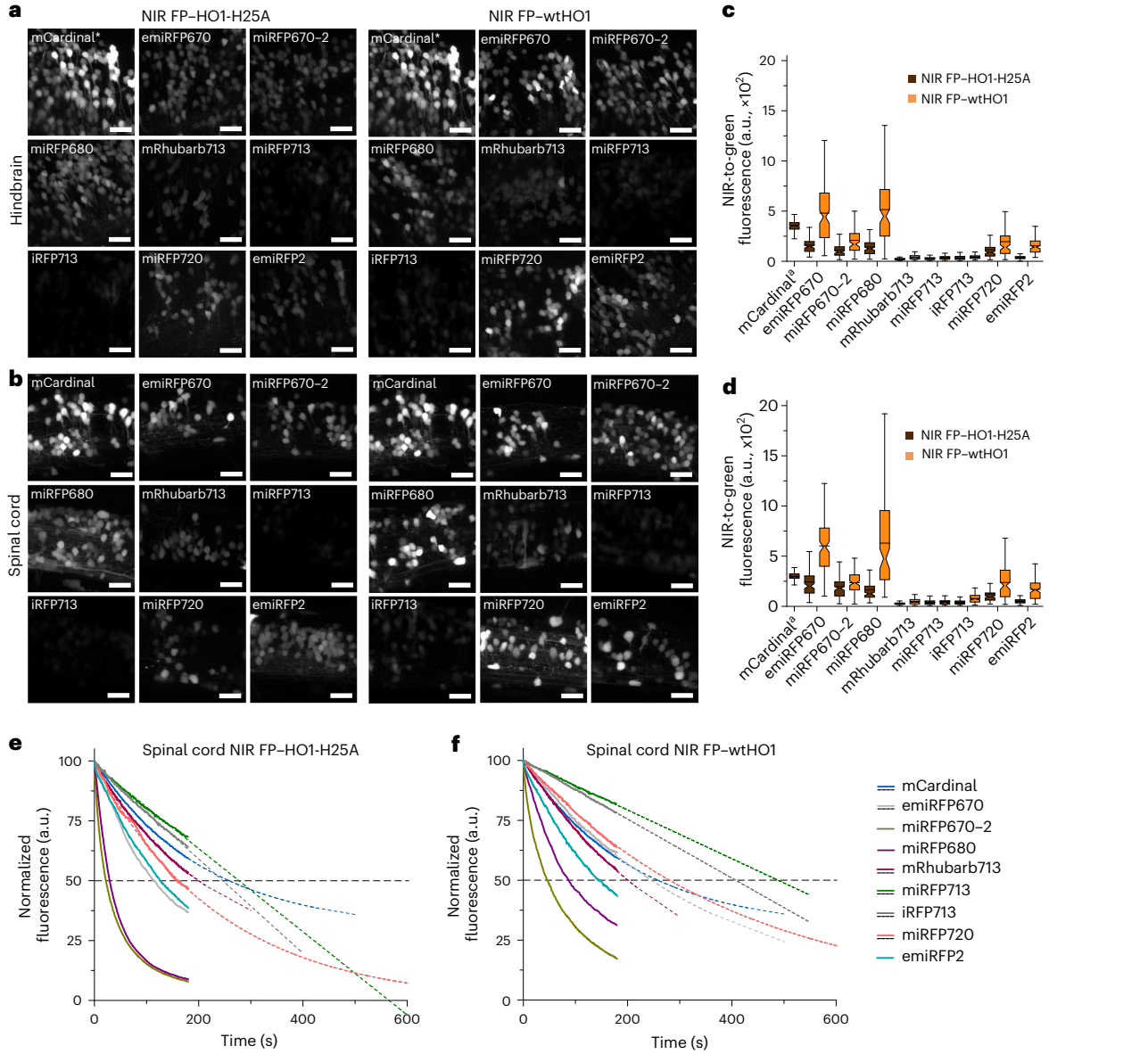

Fig. 3 | Characterization of the selected NIR FPs in neurons in live larval zebrafish at 4 dpf. a,**b**, Representative confocal fluorescence images of hindbrain (**a**) and spinal cord (**b**) neurons co-expressing each NIR FP with an inactive variant of HO1 (HO1-H25A; left panel), or its active form (wtHO1; right panel; $n = 4$ fish for each protein). Imaging conditions: excitation, 633 nm; emission, 645–780 nm. Z-stack projected images were generated, followed by adjustment of the image dynamic range, which was the same for all images (Fiji software). Scale bars, 20 µm. **c**,**d**, Intracellular normalized brightness of NIR FPs in hindbrain neurons (**c**) and spinal cord neurons (**d**) co-expressed with HO1-H25A or wtHO1. [a]mCardinal was expressed without HO1 ($n = 120$ neurons from four fish for each protein). Brightness for each FP was normalized to the mClover3 signal. **e**,**f**, Normalized photobleaching curves of NIR FPs in spinal cord neurons co-expressed with HO1-H25A (**e**) or wtHO1 (**f**). Fluorescence was normalized to the intensity value of the corresponding FP at $t = 0$ s. mCardinal was expressed without HO1 ($n = 40$ neurons from four fish for each construct). Fitting curves are presented as dashed lines where necessary. Box plots with notches: narrow part of notch, median; top and bottom of the notch, 95% confidence interval for the median; top and bottom horizontal lines, 25% and 75% percentiles for the data; whiskers extend 1.5-fold the interquartile range from the 25th and 75th percentiles; horizontal line, mean; outliers not shown but are included in all calculations and available in the source datasets. See Supplementary Data 1 for the detailed descriptive statistics and exact *P* values.

while mCardinal fluorescence was not detectable in the Cy5.5 channel. Under continuous wide-field illumination in the Cy5-LP and Cy5.5 channels at ~12 mW mm^{-2} light power (which was ~4-fold lower than that used in cultured cells), the fluorescence of miRFP680, mRhubarb713, miRFP713, iRFP713 and miRFP720 was stable for more than 20 min (less than 10% of fluorescence decline from initial values; Fig. 4d,e). mCardinal, emiRFP670 and miRFP670-2 were less photostable, losing approximately 20%, 40–50% and 45–60% of their initial fluorescence in 20 min, respectively (Fig. 4d,e and Supplementary Table 11). Based on the results, miRFP680 and miRFP713 are the proteins of choice for *C. elegans* imaging in the Cy5-LP and Cy5.5 channels, respectively.

Multicolor imaging with NIR fluorescent proteins

Analysis of intracellular brightness suggested a possibility for dual-color NIR imaging of subcellular structures using a combination of blue-shifted and red-shifted NIR FPs. In particular, NIR FPs with emission maxima below ~680 nm or beyond ~700 nm had a signal-to-background ratio of <2 in the Cy5.5 and Cy5-BP channels, respectively (Extended Data Fig. 1). To validate dual-color NIR imaging we selected two pairs

https://doi.org/10.1038/s41592-023-01975-z

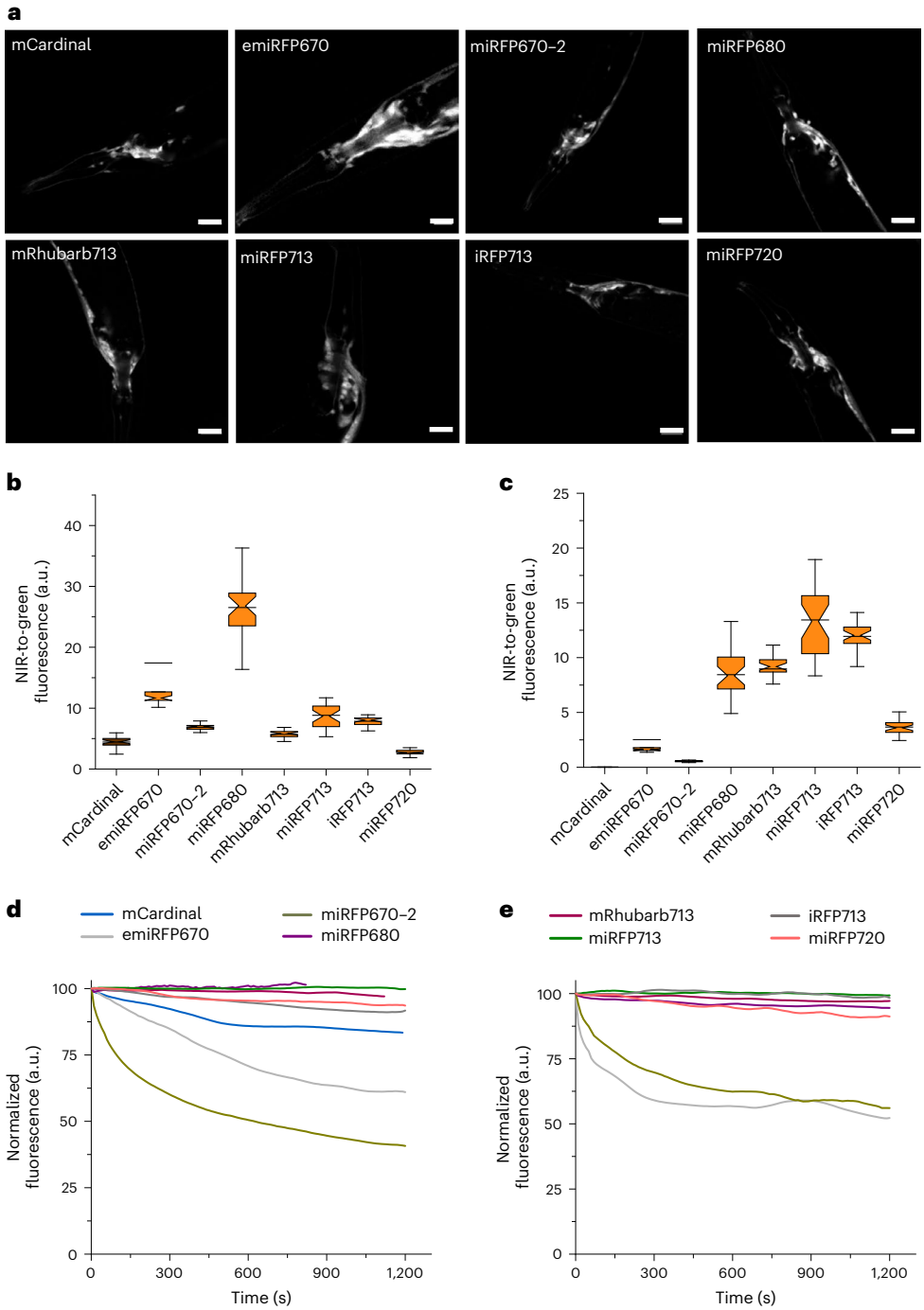

Fig. 4 | Characterization of the selected NIR FPs in neurons in live *C. elegans*. **a**, Representative confocal images of NIR FPs in the neuronal ring in the Cy5 channel ($n = 30$ worms for each protein from one transgenic line). All worms are co-expressing NIR FPs with HO1, except the ones expressing mCardinal. Imaging conditions, Cy5: excitation 639 nm, emission 655–735 nm. Dynamic range was adjusted independently for each image to facilitate visualization and images were generated using maximum projection. Scale bars, 25 µm. **b**,**c**, Intracellular normalized brightness of NIR FPs imaged in the Cy5-LP (**b**) and Cy5.5 (**c**) channels (excitation power 12.5 mW mm^{-2}; $n = 30$ worms for each protein from one transgenic line in each channel). Brightness for each FP was normalized to the mNeonGreen signal. **d**,**e**, Normalized photobleaching curves of NIR FPs imaged in the Cy5-LP (**d**) and Cy5.5 (**e**) channels (excitation power 12.5 mW mm^{-2}; $n > 10$ worms for each protein from one transgenic line for each channel). Fluorescence was normalized to the intensity value of the corresponding FP at $t = 0$ s. Box plots with notches: narrow part of notch, median; top and bottom of the notch, 95% confidence interval for the median; top and bottom horizontal lines, 25% and 75% percentiles for the data; whiskers extend 1.5-fold the interquartile range from the 25th and 75th percentiles; horizontal line, mean; outliers not shown but are included in all calculations and available in the source datasets. See Supplementary Data 1 for the detailed descriptive statistics and exact *P* values.

of NIR FPs, namely iRFP670–miRFP720 and miRFP670-2–miRFP720, which had the largest spectral separation among the NIR FPs characterized by high performance in OSER assay (Table 1). The H2B and keratin fusions with the selected NIR FPs were co-expressed in HeLa cells and imaged in the Cy5-LP–Cy5.5 and Cy5-BP–Cy5.5 channels (Fig. 5a,b, see Supplementary Fig. 19 for more representative images). The images from the separate channels clearly demonstrated the correct localization pattern of the target fusions, however, we also observed a minor

bleed-through of iRFP670 and miRFP670-2 fluorescence into the Cy5.5 channel, as well as miRFP720 fluorescence into the Cy5-LP and Cy5-BP channels. Application of dual-color imaging with BphP-based NIR FPs may require optimization of filter sets or further validation of the crosstalk; advanced spectral unmixing strategies can be also applied[33,34].

Next, we performed quadruple-color imaging of subcellular structures and organelles in zebrafish neurons using combinations of emiRFP670 with bright cyan, green and red FPs, which can be visualized under standard imaging set-ups without spectral crosstalk. emiRFP670 was selected due to its superior performance in zebrafish larvae (Fig. 3). Co-expression of the fusions of the four FPs with subcellular localization peptides or structural proteins was achieved using a single UAS (upstream activation sequence) plasmid, either co-injected with a construct driving neuron-specific expression of Gal4 or injected into specific Gal4 transgenic zebrafish one-cell stage embryos. First, we co-expressed emiRFP670 fused to EB3, a microtubule plus-end-tracking protein[35], which enables monitoring of the microtubule growth of axons in neurons, with the Lifeact-mClover3 fusion, which marks filamentous actin[36]. Using a conventional confocal microscope we were able to observe the real-time dynamics of actin-microfilaments and comet-like EB3-emiRFP670 microtubule structures at the growing axon tip of developing primary motoneurons (Supplementary Video 1). Additional co-expression of the cyan FP mTurquoise2 fused with H2B (H2B-mTurquoise2) and the membrane-targeted red FP mScarlet-I (Fyn-mScarlet-I) enabled visualization of the nuclei of primary motoneurons as well as their highly branched axonal projections, illustrating the normal outgrowth of EB3-emiRFP670 expressing motor axons (Fig. 5c).

Next, to monitor neuronal autophagy in differentiating Purkinje cells in larval zebrafish cerebellum we generated a UAS construct carrying LAMP1-emiRFP670, which labels lysosomal membranes, with a derivative of the tandem fluorescent pH-sensitive autophagic flux sensor[37], TagRFP-T-mClover3-LC3, and cytoplasmic mTurquoise2. Purkinje cell-specific Gal4 transgenic embryos[38] were injected with the construct, and subsequently autophagy was induced in 4 dpf larvae by inhibiting mTOR using bath incubations with the compound Rapalink-1 (ref. 39). Using confocal microscopy imaging with an Airyscan detector, three different vesicles associated with the autophagic fusion process were easily distinguished in the cytoplasm of Purkinje cells: autophagosomes, autolysosomes and lysosomes (Fig. 5c, see Supplementary Fig. 20 for negative control experiment).

Finally, synaptic labeling of Purkinje cells in larval zebrafish was achieved with a UAS reporter plasmid co-expressing the presynaptic and excitatory post-synaptic markers[40,41], synaptophysin b-emiRFP670 and PSD95-mScarlet-I, respectively. Expression of synaptic proteins including synaptophysin and PSD95 was reported to be reduced by HO1 overexpression in mice neurons, causing synaptic alterations[42]. Thus, the reporter construct without the HO1 gene was injected into Purkinje cell-specific Gal4 transgenic embryos[38], which resulted in detectable expression of both synaptic markers in Purkinje cells with appropriate localization, together with Fyn-mClover3 and H2B-mTurquoise2 (Supplementary Fig. 21). This showed that emiRFP670 is sufficiently bright and can be used to label synaptic structures together with additional FPs, even without boosting its NIR fluorescence by HO1 expression. Taken together, emiRFP670 is a superior NIR FP for the use of multicolor cellular compartment labeling in zebrafish and is useful for multiplex imaging of in vivo cell biological studies.

Discussion

A systematic characterization of NIR FPs enabled us to identify the best-performing FPs for applications in cultured cells and in vivo in model organisms. Although there was no single best FP for every tested condition, a small set of NIR FPs can cover the majority of potential applications. For example, for imaging of non-neuronal cells in culture and in vivo, miRFP680 has proven to be reliable due to its superior brightness and high photostability both in live and fixed samples. In addition, its monomeric behavior in cells is advantageous for the most demanding applications. For neuroimaging in mice, particularly if the goal is to image neuronal morphology, emiRFP670 is the only suitable choice due to its exceptional neuronal labeling and high intracellular brightness in acute brain slices (it ranked second in brightness following miRFP680). The photostability of emiRFP670 in PFA-fixed brain tissue appeared to be almost 20-fold higher than in live tissue, making it more suitable for imaging in preserved samples. emiRFP670 can be used as a fluorescent tag for structural proteins and organelle labeling suitable for real-time imaging in zebrafish larvae. However, in *C. elegans* neurons, miRFP680 significantly outperformed emiRFP670 in both brightness and photostability while demonstrating high-quality neuronal labeling. As a result, miRFP680 and emiRFP670 can perhaps cover the majority of applications unless imaging in the Cy5.5 channel is required. In that case, miRFP720, miRFP713 or iRFP713 are the potential candidates. miRFP720 is a protein of choice for structural imaging in preserved samples given that it appeared to be the most monomeric FP by the OSER assay and demonstrated high performance in fixed cells. For live sample imaging, miRFP720 is optimal for neuronal labeling in zebrafish. miRFP720 might also be useful when fast cellular labeling is needed given that it demonstrated superior brightness during short-term expression in the brain and liver. In turn, miRFP713 is beneficial for long-term imaging (more than 2–3 months) in mammalian neurons if neuropil labeling is not required (note that miRFP720 demonstrated better neuronal labeling than miRFP713). miRFP713 should also be used for *C. elegans* imaging in the Cy5.5 channel. iRFP713 can be applied for cytoplasmic labeling when live imaging of non-neuronal cells in Cy5.5 channels is needed. However, if downstream sample processing requires PFA fixation, miRFP713 would be a better choice due to its higher performance in fixed samples and only slightly lower brightness in live cells. In short, miRFP680 and emiRFP670 are the most optimal for imaging in the Cy5-LP and Cy5-BP channels, while miRFP720, miRFP713 and iRFP713 (to a lower degree than the former two NIR FPs) should be selected for imaging in the Cy5.5 channel based on the particular cell type or model organism requirements, as well as the sample preparation method. The use of BphP-based NIR FPs in small model organisms, including zebrafish, flies and worms, requires an additional experimental consideration such as co-expression of HO1. First, heme metabolism is tightly controlled, and expression of recombinant HO1 may interfere with cellular physiology. Second, expression cassettes need to include an addition of ~1 kbp (size of the HO1 gene), which further increases the size of the DNA cargo for intracellular delivery (BphP-based genes are 1.5-fold bigger than GFP-like FPs). These factors should be taken into account during experimental design.

Besides characterization in cultured cells and in vivo, the selected NIR FPs were assessed under different imaging modalities. We demonstrated the potential applicability of blue- and red-shifted NIR FPs for dual-color imaging of fusion proteins, however, minor cross-bleed was observed between the Cy5-LP and Cy5.5 channels. Optimization of filter sets or selection of NIR FPs with a larger spectral separation are potential options for improving dual-color NIR imaging. Alternatively, advanced spectral unmixing algorithms can be applied at the image processing step[33,34]. Based on the measured two-photon absorption spectra, the NIR FPs are suitable for dual-color imaging with GFPs using the standard titanium–sapphire laser. However, two-photon photostability cannot be readily predicated based on one-photon photobleaching data, and therefore end-users may need to estimate two-photon photostability to choose an optimal NIR FP. Despite high performance in PFA-fixed samples, the chemical stability of biliverdin IXα-binding FPs is insufficient for super-resolution imaging with expansion microscopy. Further development of NIR FPs might be required to extend their applicability for imaging techniques that involve harsh chemical treatment of samples. We suggest emiRFP670 and BDFP1.8 as promising starting templates for the development of chemically stable NIR FPs.

https://doi.org/10.1038/s41592-023-01975-z

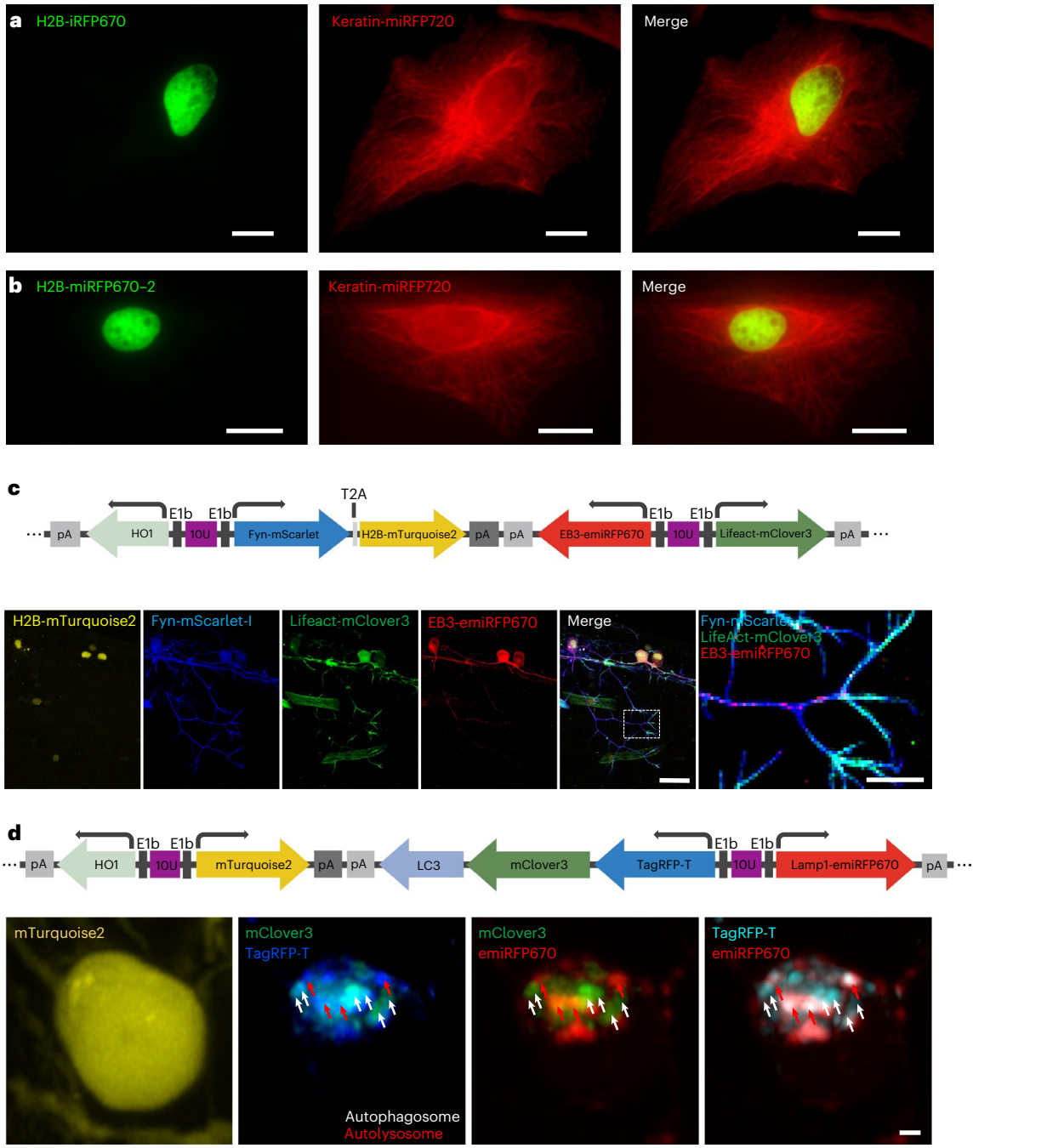

Fig. 5 | Multicolor imaging with NIR FPs. a, Representative dual-color NIR imaging of live HeLa cells co-expressing H2B-iRFP670 and keratin-miRFP720 acquired in the Cy5-BP and Cy5.5 channels ($n = 30$ cells from two independent transfections). **b**, Representative dual-color NIR imaging of live HeLa cells co-expressing H2B-miRFP670-2 and keratin-miRFP720 acquired in the Cy5-BP and Cy5.5 channels ($n = 30$ cells from two independent transfections). **c**, Schematic representation (top) of the expression cassette used for co-expression of quadruple reporters with HO1, and (bottom) representative pseudocolor fluorescence images from 33 hours post-fertilization (hpf) zebrafish larva in which the primary spinal motor neurons co-express EB3-emiRFP670 (red) and three additional fluorescent markers labeling nucleus (H2B-mTurquoise2, yellow), plasma membrane (Fyn-mScarlet-I, blue) and F-actin (LifeAct-mClover3, green; $n = 8$ fish). Right, higher magnification image of the boxed region showing that signals for EB3-emiRFP670 marking the microtubule plus-end (red) are distributed along the axons (blue) where F-actin was visualized with LifeAct-mClover3 (green) and concentrated highly at the axon terminals. Imaging conditions: see Methods section for the exact optical set-up. Z-stack projected images were generated, followed by adjustment of the dynamic ranges independently for each image from four different channels. The images are further processed to facilitate visualization in different colors in four different channels (Fiji software). **d**, Schematic representation (top) of the expression cassette used for co-expression of triple reporters with HO1, and (bottom) representative pseudocolor fluorescence images of a Purkinje cell in 4 dpf zebrafish exposed to Rapalink-1, showing co-expression of cytoplasmic mTurquoise2 (yellow), autophagy flux sensor TagRFP-T-mClover3-LC3 (blue and green) and LAMP1-emiRFP670 (red), which enables identification of autophagosomes (white arrows) and autolysosomes (red arrows; $n = 8$ fish). Each image was processed directly using the Zeiss Airyscan image processing algorithm in the Zen black software, allowing for linear deconvolution with the Wiener filter and alignment of each offset detector to the central element. Z-stack projected images were generated, followed by adjustment of the dynamic range independently. To facilitate visualization, images are further processed in four different channels to discriminate each signal in the merged images (Fiji software). Scale bars: **a**,**b**, 20 µm; **c**, 30 µm (merge), 10 µm (inset); **d**, 1 µm.

We are confident that protein engineers will continue to develop improved NIR FPs for both general and specialized applications. This study may provide certain guidelines for future protein engineering efforts. First, the molecular brightness of NIR FPs expressed by *E. coli* should not be considered as a screening parameter during protein evolution because it has low correlation with intracellular brightness (Supplementary Fig. 4). Second, relative intracellular brightness in one cell type does not necessarily translate to another cell type. Therefore, expression host systems for NIR FP screening should be selected based on the intended applications. Co-expression of a reference FP via P2A peptide is an acceptable approach for intracellular brightness quantification both in cell culture and in vivo. Brightness in cultured neurons can be used as a selection criterion for imaging neurons in vivo in mammals, however, the quality of neuronal labeling in vivo is not possible to predict from neuronal culture results. Third, relative photostability measured under matching illumination is highly correlated between different cell types, however, PFA fixation may alter photobleaching rates considerably. Fourth, the OSER assay is valid for BphP-based NIR FPs, and we suggest using miRFP720 as a control; however, the values reported in Table 1 should not be interpreted as absolute values. Finally, we suggest that newly developed NIR FPs are benchmarked against miRFP680 and emiRFP670 in Cy5 channels and against miRPF720 and miRFP713 in the Cy5.5 channel.

Protocol registration

The study was conducted according to the registered peer-reviewed protocol available at https://springernature.figshare.com/articles/journal_contribution/Piatkevich_AIP_pdf/17213501. Other than pre-registered and approved pilot data, all data reported in the paper were acquired after the date of the registered protocol publication.

Online content

Any methods, additional references, Nature Portfolio reporting summaries, source data, extended data, supplementary information, acknowledgements, peer review information; details of author contributions and competing interests; and statements of data and code availability are available at https://doi.org/10.1038/s41592-023-01975-z.

References

1. Prasher, D. C., Eckenrode, V. K., Ward, W. W., Prendergast, F. G. & Cormier, M. J. Primary structure of the *Aequorea victoria* green-fluorescent protein. *Gene* **111**, 229–233 (1992).
2. Shcherbakova, D. M., Stepanenko, O. V., Turoverov, K. K. & Verkhusha, V. V. Near-infrared fluorescent proteins: multiplexing and optogenetics across scales. *Trends Biotechnol.* **36**, 1230–1243 (2018).
3. Filonov, G. S. et al. Bright and stable near-infrared fluorescent protein for in vivo imaging. *Nat. Biotechnol.* **29**, 757–761 (2011).
4. Chu, J. et al. Non-invasive intravital imaging of cellular differentiation with a bright red-excitable fluorescent protein. *Nat. Methods* **11**, 572–578 (2014).
5. Shcherbakova, D. M. & Verkhusha, V. V. Near-infrared fluorescent proteins for multicolor in vivo imaging. *Nat. Methods* **10**, 751–754 (2013).
6. Babakhanova, S. et al. Rapid directed molecular evolution of fluorescent proteins in mammalian cells. *Protein Sci.* **31**, 728–751 (2022).
7. Qian, Y. et al. A genetically encoded near-infrared fluorescent calcium ion indicator. *Nat. Methods* **16**, 171–174 (2019).
8. Qian, Y. et al. Improved genetically encoded near-infrared fluorescent calcium ion indicators for in vivo imaging. *PLoS Biol.* **18**, e3000965 (2020).
9. Shcherbakova, D. M., Cox Cammer, N., Huisman, T. M., Verkhusha, V. V. & Hodgson, L. Direct multiplex imaging and optogenetics of Rho GTPases enabled by near-infrared FRET. *Nat. Chem. Biol.* **14**, 591–600 (2018).
10. Shcherbakova, D. M. et al. Bright monomeric near-infrared fluorescent proteins as tags and biosensors for multiscale imaging. *Nat. Commun.* **7**, 12405 (2016).
11. Kamper, M., Ta, H., Jensen, N. A., Hell, S. W. & Jakobs, S. Near-infrared STED nanoscopy with an engineered bacterial phytochrome. *Nat. Commun.* **9**, 4762 (2018).
12. Wegner, W. et al. In vivo mouse and live cell STED microscopy of neuronal actin plasticity using far-red emitting fluorescent proteins. *Sci. Rep.* **7**, 11781 (2017).
13. Matlashov, M. E. et al. A set of monomeric near-infrared fluorescent proteins for multicolor imaging across scales. *Nat. Commun.* **11**, 239 (2020).
14. Piatkevich, K. D., Subach, F. V. & Verkhusha, V. V. Engineering of bacterial phytochromes for near-infrared imaging, sensing, and light-control in mammals. *Chem. Soc. Rev.* **42**, 3441–3452 (2013).
15. Shcherbakova, D. M., Baloban, M. & Verkhusha, V. V. Near-infrared fluorescent proteins engineered from bacterial phytochromes. *Curr. Opin. Chem. Biol.* **27**, 52–63 (2015).
16. Piatkevich, K. D. et al. Near-infrared fluorescent proteins engineered from bacterial phytochromes in neuroimaging. *Biophys. J.* **113**, 2299–2309 (2017).
17. Shemetov, A. A. et al. A near-infrared genetically encoded calcium indicator for in vivo imaging. *Nat. Biotechnol.* **39**, 368–377 (2021).
18. Yu, D. et al. A naturally monomeric infrared fluorescent protein for protein labeling in vivo. *Nat. Methods* **12**, 763–765 (2015).
19. Paez-Segala, M. G. et al. Fixation-resistant photoactivatable fluorescent proteins for CLEM. *Nat. Methods* **12**, 215–218 (2015).
20. Campbell, B. C., Paez-Segala, M. G., Looger, L. L., Petsko, G. A. & Liu, C. F. Chemically stable fluorescent proteins for advanced microscopy. *Nat. Methods* **19**, 1612–1621 (2022).
21. Tillberg, P. W. et al. Protein-retention expansion microscopy of cells and tissues labeled using standard fluorescent proteins and antibodies. *Nat. Biotechnol.* **34**, 987–992 (2016).
22. Cranfill, P. J. et al. Quantitative assessment of fluorescent proteins. *Nat. Methods* **13**, 557–562 (2016).
23. Costantini, L. M., Fossati, M., Francolini, M. & Snapp, E. L. Assessing the tendency of fluorescent proteins to oligomerize under physiologic conditions. *Traffic* **13**, 643–649 (2012).
24. Li, X. D. et al. Design of small monomeric and highly bright near-infrared fluorescent proteins. *Biochim. Biophys. Acta Mol. Cell Res.* **1866**, 1608–1617 (2019).
25. Shaner, N. C. et al. A bright monomeric green fluorescent protein derived from *Branchiostoma lanceolatum*. *Nat. Methods* **10**, 407–409 (2013).
26. Day, R. N. & Davidson, M. W. The fluorescent protein palette: tools for cellular imaging. *Chem. Soc. Rev.* **38**, 2887–2921 (2009).
27. Drobizhev, M., Makarov, N. S., Tillo, S. E., Hughes, T. E. & Rebane, A. Two-photon absorption properties of fluorescent proteins. *Nat. Methods* **8**, 393–399 (2011).
28. Piatkevich, K. D. et al. A robotic multidimensional directed evolution approach applied to fluorescent voltage reporters. *Nat. Chem. Biol.* **14**, 352–360 (2018).
29. Mikhaylov, A. et al. Hot-band absorption can mimic entangled two-photon absorption. *J. Phys. Chem. Lett.* **13**, 1489–1493 (2022).
30. Babakhanova, S. et al. Rapid directed molecular evolution of fluorescent proteins in mammalian cells. *Protein Sci.* **31**, 728–751 (2022).
31. Holowiecki, A., O'Shields, B. & Jenny, M. J. Characterization of heme oxygenase and biliverdin reductase gene expression in zebrafish (*Danio rerio*): basal expression and response to pro-oxidant exposures. *Toxicol. Appl. Pharmacol.* **311**, 74–87 (2016).

32. Qian, Y. et al. Improved genetically encoded near-infrared fluorescent calcium ion indicators for in vivo imaging. *PLOS Biol.* **18**, e3000965 (2020).
33. Seo, J. et al. PICASSO allows ultra-multiplexed fluorescence imaging of spatially overlapping proteins without reference spectra measurements. *Nat. Commun.* **13**, 2475 (2022).
34. Chiang, H. J. et al. HyU: Hybrid Unmixing for longitudinal in vivo imaging of low signal-to-noise fluorescence. *Nat. Methods* **20**, 248–258 (2023).
35. Stepanova, T. et al. Visualization of microtubule growth in cultured neurons via the use of EB3-GFP (end-binding protein 3-green fluorescent protein). *J. Neurosci.* **23**, 2655–2664 (2003).
36. Riedl, J. et al. Lifeact: a versatile marker to visualize F-actin. *Nat. Methods* **5**, 605–607 (2008).
37. Kimura, S., Noda, T. & Yoshimori, T. Dissection of the autophagosome maturation process by a novel reporter protein, tandem fluorescent-tagged LC3. *Autophagy* **3**, 452–460 (2007).
38. Namikawa, K. et al. Modeling neurodegenerative spinocerebellar ataxia type 13 in zebrafish using a Purkinje neuron specific tunable coexpression system. *J. Neurosci.* **39**, 3948–3969 (2019).
39. Rodrik-Outmezguine, V. S. et al. Overcoming mTOR resistance mutations with a new-generation mTOR inhibitor. *Nature* **534**, 272–276 (2016).
40. Meyer, M. P. & Smith, S. J. Evidence from in vivo imaging that synaptogenesis guides the growth and branching of axonal arbors by two distinct mechanisms. *J. Neurosci.* **26**, 3604–3614 (2006).
41. Niell, C. M., Meyer, M. P. & Smith, S. J. In vivo imaging of synapse formation on a growing dendritic arbor. *Nat. Neurosci.* **7**, 254–260 (2004).
42. Li, L. et al. Overexpression of heme oxygenase 1 impairs cognitive ability and changes the plasticity of the synapse. *J. Alzheimers Dis.* **47**, 595–608 (2015).

Methods

Molecular cloning

Synthetic DNA oligonucleotides used for cloning were synthesized by Tsingke Biotechnology. PrimeStar Max master mix (Takara) or 2×Hieff PCR Master Mix (Yeasen) was used for high-fidelity polymerase chain reaction (PCR) amplifications. Restriction endonucleases were purchased from New England BioLabs and used according to the manufacturer's protocols. DNA ligations were performed using T4 DNA ligase (New England BioLabs) or the NovoRec plus one step cloning kit (Novoprotein). The ligation products were chemically transformed into the TOP10 *E. coli* strain (Biomed) and cultured according to the standard protocols. Sequencing of bacterial colonies and purified plasmids was performed using Sanger sequencing (Zhejiang Youkang Biological Technology). Small-scale isolation of plasmid DNA was performed with commercially available Mini-Prep kits (Qiagen or Tiangend); large-scale DNA plasmid purification was done with Midi-Prep kits (Qiagen).

The mammalian codon-optimized genes of NIR FPs were de novo synthesized by Tsingke Biotechnology or Shanghai Generay Biotech based on the amino acid sequences reported in the original publications. Oligonucleotides for cloning were purchased from Tsingke Biotechnology or Zhejiang Youkang Biological Technology (see the list of all primers used in this study in Supplementary Dataset 2). To clone pAAV-CAG-NIR-FPs-P2A-EGFP plasmids, the complementary DNA of the NIR FPs was PCR amplified with *Kpn*I/*Age*I flanking sites and swapped with the TagRFP658 gene in the pAAV-CAG-TagRFP658-P2A-EGFP plasmid (Addgene 178971). To clone pAAV-CAG-NIR-FP plasmids, the cDNA of the NIR FPs was PCR amplified with *Kpn*I/*EcoR*I flanking sites and swapped with the GFP gene in the pAAV-CAG-GFP (Addgene 37825). To construct CytERM (cytoplasmic end of an endoplasmic reticulum signal anchor membrane protein) fusions, the NIR FPs were PCR amplified with *Age*I/*Not*I flanking sites and swapped with the mScarlet gene in the pCytERM-mScarlet-N1 (Addgene plasmid 85066). To construct plasmids for expression of structural protein fusions, the cDNA of the selected NIR FPs was PCR amplified and swapped with the corresponding FP genes in the mRuby-Cx43-7 (Addgene 55856), pKeratin-miRFP670nano (Addgene 127437), pActin-Electra1 (Addgene 184941), pH2B-Electra1 (Addgene 179478) and pTubuiln-Electra1 (Addgene 184929) plasmids. All plasmids used in this study are available from Addgene and WeKwikGene (https://wekwikgene.wllsb.edu.cn).

Characterization in cultured mammalian cells

All animal maintenance and experimental procedures were conducted according to the Westlake University Animal care guidelines, and all animal studies were approved by the Institutional Animal Care and Use Committee (IACUC) of Westlake University, Hangzhou, China under animal protocol 19-044-KP. For all experiments involving mice throughout, the C57BL/6J strain (supplied by the animal facility of Westlake University) was used regardless of sex. HEK293FT (Invitrogen) and HeLa (ATCC CCL-2) cells were authenticated by the manufacturer using STR (short tandem repeat) profiling, re-authenticated in our lab by inspecting the stereotypical morphological features under wide-field microscope, and tested to ensure negativity for mycoplasma contamination to their standard levels of stringency. Authentication by morphology was performed every time before transient transfection.

The intracellular brightness and photostability were measured in HEK cells and in primary hippocampal mouse neurons using a Nikon Ti2-E wide-field fluorescence microscope equipped with a Spectra III Light Engine (LumenCore), 680 nm CNI laser, and an ORCA-Flash 4.0 V3 sCMOS camera (Hamamatsu) with ×10 0.45 numerical aperture (NA) and ×20 0.75NA objective lenses (Nikon) controlled by NIS Elements AR 5.21.00 (Nikon). To facilitate unbiased comparison of NIR FPs in cell culture, we used blinding and randomization. The experimentors were blinded to protein identity; all vials with plasmids were barcoded, and the identity of the proteins was shown only after data collection and analysis were finished. The transfection and imaging of the samples were performed in random order; all vials with plasmids were pooled together and randomly picked one by one during transfection. Independent transfections were randomized independently.

HEK293FT cells were cultured in DMEM supplemented with 10% fetal bovine serum (FBS) and 1% penicillin–streptomycin, and seeded in a 24-well glass-bottom plate (P24-0-N Cellvis) after Matrigel (356235, BD Biosciences) coating. Cells were transfected at 80–90% confluency using Hieff Trans Liposomal Transfection Reagent (Yeasen Biotechnology, 40802ES02) according to the manufacturer's protocol, and imaged using a fluorescence wide-field microscope at 36–48 h after transfection. First, transfected cells were imaged without exogenous biliverdin IXα, then 25 μM biliverdin IXα was added to the cell medium and incubated for 3 h at 37 °C in a cell incubator. Before imaging, cells were washed once with PBS to remove excess biliverdin IXα and the same fields of view were imaged again in fresh culture media under the same imaging settings. Cells were imaged in the FITC (excitation 475/28 nm at 5.30 mW mm^{-2} from SpectraIII LumenCor; emission 535/46 nm), Cy5-BP (excitation: 635/22 nm at 56–58 mW mm^{-2} from SpectraIII LumenCor; emission 679/41 nm), Cy5-LP (excitation: 635/22 nm at 56–58 mW mm^{-2} from SpectraIII LumenCor; emission 664LP), and Cy5.5 (excitation: 680/13 nm at 56–58 mW mm^{-2} from 680 nm CNI laser; emission 710LP) channels. To obtain statistically significant datasets, we performed three independent transfections and analyzed more than 100 regions of interest (ROIs) from each transfection (at least 300 ROIs for analysis in total per construct). ROIs were determined using the auto-detect function of NIS Elements software and limiting the smallest ROI to 50 μm^2 (the size of an HEK cell). The mean fluorescence intensity in the green, Cy5-BP, Cy5-LP and Cy5.5 channels for ROIs was extracted and the Cy5-BP-to-green, Cy5-LP-to-green and Cy5.5-to-green fluorescence ratios were calculated for each construct after background subtraction for each channel, and used for further comparison of intracellular brightness under corresponding imaging conditions. The data were excluded from analysis if the cells died after transfection or if the cell culture was contaminated with bacteria or yeast.

To measure photostability in live HEK cells, HEK cells were transfected as described above and imaged under continuous Cy5 and Cy5.5 wide-field excitation. The photobleaching curves were calculated for each cell individually, and average photobleaching half-time with standard deviation was reported for each protein. Photobleaching was performed for at least a 50% fluorescence drop, when possible, and reported as the mean photobleaching curve for each protein (averaged from all individual curves). Cells that detached or died during photobleaching experiments were excluded from data analysis.

To quantify intracellular brightness in live primary mouse hippocampal neurons, cultured neurons were prepared as previously described[43] and transfected with pAAV-CAG-NIR-FPs-P2A-EGFP plasmids using the calcium phosphate transfection method or transduced using rAAV2/9-CAG-NIR-FPs-P2A-EGFP viruses (Shanghai Sunbio Medical Biotechnology). In brief, hippocampal neurons were transfected at DIV (days in vitro) 4–5 using the calcium phosphate transfection kit (K278001, Invitrogen) according to the previously described protocol[28]. To obtain a high density of neurons expressing NIR FPs, transduction was performed with ~1 μl rAAV2/9 viruses (>10^{12} vector genome (v.g.) ml^{-1}) per well, in 1 ml culture medium at DIV 4–5 (this procedure was not proposed during stage 1 but was included in the final version to compensate for the low density of calcium phosphate transfection). Neurons expressing NIR FPs were imaged at DIV 12–18 using the same imaging set-up as described above for HEK cells. Mean fluorescence intensity was calculated for neuronal soma only. Intracellular brightness with and without biliverdin IXα, and photostability were measured and quantified using the same procedure as described for HEK cells above. The culture was excluded from the analysis if cells died after transfection or if the culture was contaminated with bacteria or yeast.

Bottom-up proteomic analysis was performed using liquid chromatography with tandem mass spectrometry (LC-MS/MS). In brief, ~10^6 HEK cells transiently transfected with pAAV-CAG-NIR-FPs-P2A-GFP plasmids as described above were lysed using RIPA buffer (89900, Thermo Fisher) and the extracted peptides were analyzed using an Orbitrap Fusion Lumos mass spectrometer (Thermo Fisher) in data-independent acquisition (DIA) mode. The precolumn (75 µm inner diameter (i.d.), 360 µm outer diameter (o.d.), 2 cm long) was packed with 3 µm C18 packing material (100 Å pore size, 164946, Thermo Scientific) and liquid chromatograph columns (75 µm i.d., 360 µm o.d., 25 cm long) were packed with 1.9 µm C18 particles (164941, Thermo Scientific). The flow rate of the liquid chromatography separation was 300 nl min^{-1} using a nanoUPLC pump (UltiMate 3000 RSLC-nano, Thermo Scientific). A linear 60 min gradient of 5–98% buffer B (0.1% formic acid in 80% acetonitrile) was used for the liquid chromatography separation. All samples were analyzed using an Orbitrap Fusion Lumos mass spectrometer (Thermo Fisher Scientific, tune version 3.4 and Xcalibur version 4.4) with high-field asymmetric waveform ion mobility spectrometry pro (FAIMS pro). The peptide precursors were first isolated by Orbitrap (60,000 resolution) and interrogated by MS2 in the Orbitrap (15,000 resolution) using high energy collisional dissociation at a collision energy of 30. The MS/MS spectra were recorded at a target value of 5×10^4 with a 30 ms maximum ion injection time. Acquired data were processed with DIA-NN software (https://github.com/vdemichev/diann) for protein identification and quantification, and PEAKS Studio Xpro software (Bioinformatics Solutions) was used to identify post-translational modifications. Here, we report protein identity for each analyzed sample as well as identified post-translational modifications.

For western blot analysis (which was not proposed during stage 1 but was included in the final version to complement the mass spectrometry results), HEK cells transfected with pAAV-CAG-NIR-FPs-P2A-GFP were washed twice with ice-cold PBS and then lysed for 10 min in 200 l RIPA Lysis Buffer I (lot no. C500005-0010, Sangon Biotech) containing protease inhibitor cocktail (buffer B) and phosphatase inhibitor cocktail (buffer C). The cell lysates were sonicated with an ultrasonic liquid processor (VCX150, Sonics) and the protein concentration was determined using a BCA Protein Quantification Kit (20201ES76, Yeasen Biotechnology). A 5X Sample Buffer (lot no. MB01015, GenScript) was used as a tracking dye for SDS–PAGE gel loading. For each sample, 20 µg total protein was loaded onto an SDS-polyacrylamide gel (M00669, GenScript) and transferred to a PVDF membrane (ISEQ00010, Millipore) using a wet electro-transfer method (at 300 mA for 80 min). The membrane was blocked in TBST containing 5% FBS for 1 h at room temperature before being treated overnight at 4 °C with the following primary antibodies: rabbit anti-GFP (1:1,000, 2956T, Cell Signaling Technology) and mouse anti-P2A (1:1000, NBP3-09171SS, Novus Biologicals). Proteins were detected using an enhanced chemiluminescence (ECL) detection system (Yeasen Biotechnology, 36222ES60) and documented using an Amersham Imager 680 imager (GE Healthcare). The Amersham Imager 680 Analysis software was used to calculate band intensity and area.

To perform the cytotoxicity assay of the NIR FPs, HEK cells were transiently transfected with pAAV-CAG-NIR-FP plasmids and dummy DNA (pUC19) as a negative control, using Hieff Trans Liposomal Transfection Reagent (40802ES02, Yeasen Biotechnology), and assessed at 36–48 h after transfection using Annexin V, Alexa Fluor 568 conjugate (A13202, ThermoFisher) and Live/Dead reagent (L34958, Viability/Vitality Kit, ThermoFisher), according to the manufacturer's protocol with minor adjustments. Annexin V conjugates are designed to detect the externalization of phosphatidylserine, one of the earliest indicators of apoptosis. In brief, we prepared annexin-binding buffer: 10 mM HEPES, 140 mM NaCl and 2.5 mM $CaCl_2$, pH 7.4, and added dyes indicating live and dead cells into the buffer at working concentrations. The HEK cells were collected at a concentration of 1×10^6 cells ml in each 1.5 ml tube using EDTA-free Trypsin (BL527A, Biosharp) and washed in cold PBS. The washed cells were centrifuged, and supernatant was removed. One tube of non-transfected cell pellet was heated at 50 °C for 10 min to obtain the heat-killed cells as a positive control for apoptotic and dead cells. The HEK cells including the positive control were resuspended in 100 µl annexin-binding buffer containing Live/Dead dyes. After incubating the cells on ice for 15 min, 5 µl annexin V conjugate were added into each 100 µl cell suspension and the cells were further incubated at room temperature for 15 min. A total of 400 µl annexin-binding buffer without Live/Dead dyes was added, mixed gently, and cells were briefly kept on ice. The stained cells were analyzed using a flow cytometer (CytoFLEX LX, Beckman Coulter) equipped with a 405 nm laser and 450/45 bandpass for calcein violet-labeled live cells (Live V450-PB-A), and 525/40 bandpass for the aqua fluorescent reactive dye-labeled dead cells (Dead V525-KrO-A); a 561 nm laser and 585/42 bandpass (Apoptosis Y585-PE-A) were used for Annexin V-labeled live cells. The channels Cy5-BP R660-APC-A and Cy5-LP R712-APCA700-A were used to analyze the NIR FP-positive cells with a 638 nm laser. Cytotoxicity was quantified as the fraction of dead cells and cells in the early stage of apoptosis in the total transfected cells. Given that the NIR FP signal exhibited crosstalk into the channels used for detection of the dye signals, the signals were compensated correspondingly.

To quantify fluorescence retention upon PFA fixation, HEK cells were transfected as described above, and imaged using a fluorescence wide-field microscope at 36–48 h after transfection without exogenous biliverdin IXα. After imaging in the Cy5-LP and Cy5.5 channels, cells were washed with PBS twice and fixed with 4% PFA (15714, Electron Microscopy Sciences) in PBS at room temperature for 15 min. Fixed cells were gently washed with PBS twice and the same fields of view were imaged under identical imaging settings. Image analysis was performed as described above for live cells. To obtain statistically significant datasets, we performed two independent transfections and analyzed more than 1,000 ROIs for each transfection.

The protein retention expansion microscopy (proExM) experiments were conducted according to a previously described protocol[21]. HEK cells, seeded and transfected in glass-bottom dishes (MatTek) as described above, were treated with 4% PFA in PBS for 15 min, washed three times for 5 min with PBS, and imaged in FITC and Cy5-LP channels with a ×20 0.75NA objective lens under a Nikon wide-field microscope. After imaging, fixed cells were incubated with 0.1 mg ml^{-1} AcX (A20770, Life Technologies) for at least 6 h at 23 °C. After washing with PBS, cells were incubated with activated monomer solution (8.625% (w/w) sodium acrylate, 2.5% (w/w) acrylamide, 0.15% (w/w) N,N′-methylenebisacrylamide, PBS, 2 M NaCl, 0.2% (w/w) APS and 0.2% (v/v) TEMED) and gelled for 2 h in a humidified incubator at 37 °C in a nitrogen atmosphere. Formed sample–hydrogel composites were digested with proteinase K (New England Biolabs) in digestion buffer (50 mM Tris, 1 mM EDTA, 0.5% Triton X-100, 1 M NaCl, pH 8.0) overnight at 23 °C. Following digestion, the samples were processed by extensively washing with PBS, and then shrunk in 1 M NaCl and 60 mM $MgCl_2$. Digested samples were imaged using the same setting as fixed cells. The same cells before and after proExM treatment were identified manually and analyzed using NIS Elements software.

To quantify the monomeric state of NIR FPs in mammalian cells, the OSER assay[23] was used as previously described[22]. In brief, HeLa (ATCC CCL-2) cells were cultured and transfected with the pCytERM-NIR-FPs-N1 plasmids as described for HEK cells and imaged 12–18 h after transfection using the Cy5-LP channel. For each NIR FP we performed at least two independent transfections and analyzed at least 250 individual cells for each transfection. Following the protocol described by Cranfill et al.[22], positive cells selected for analysis had overall similar fluorescence brightness, and cells that were significantly brighter were excluded (indications of unhealthy or highly stressed cells). Cells with non-spherical nuclei, endoplasmic reticulum sheet architectures, or condensed nuclei were also excluded from the assay

(see Supplementary Fig. 10 for representative images of cells excluded from the analysis). Image analysis was performed by three blinded independent researchers, using NIS Elements software, and mean values with standard errors were calculated. Moreover, each NIR FP was further assessed by calculating the ratio of structure MFI (mean fluorescence intensity) to NE (nuclear envelope) MFI as proposed by Costantini et al.[23]. Structures visibly distinct from the endoplasmic reticular networks were manually traced using the free cycle selection tool in ImageJ, and the MFI for the selected area was measured. Using the freehand line selection tool in ImageJ, three separate regions of the nuclear envelope were manually traced avoiding karmellae, and the NE MFI was measured and averaged. Live HeLa cells expressing NIR FP fusions with structural proteins were imaged at 24–36 h after transfection using an Olympus FV3000 inverted confocal microscope (except miRFP680, which was additionally imaged in fixed cells using a Nikon CSU-W1 SoRa), acquiring on average four fields of view in the Cy5 channel (excitation 640 nm; emission ~660–735 nm). Dual-color NIR imaging was performed in the Cy5-LP–Cy5.5 and Cy5-BP–Cy5.5 channels using the Nikon wide-field microscope described above.

In vitro characterization

For protein purification, the NIR FPs genes were inserted between the *Xho*I and *Pst*I sites of the pBAD vector that encodes HO1 from the cyanobacteria *Synechocystis sp*. CACIAM 05 to convert an endogenous heme in bacteria into biliverdin IXα, as previously described[7]. The plasmids were transformed into the TOP10 *E. coli* strain (Biomed) and grown in RM medium supplemented with ampicillin and 0.06% arabinose for 18–20 h at 37 °C followed by incubation for 24 h at 18 °C. Proteins were purified with metal affinity chromatography using Ni-NTA resin (20503ES50, Yeasen Biotechnology) according to the manufacturer's protocol. Proteins were eluted with PBS containing either 400 mM imidazole or 100 mM EDTA (EDTA was used for mRhubarb713 elution given that 400 mM imidazole resulted in protein discoloration, perhaps due to the chromophore substitution). The purified proteins were dialyzed against PBS at pH 7.4 and adjusted to the required concentration for spectroscopy. The UV–visible absorption spectra were measured in the range 250–800 nm using the UV-VIS-NIR UV3600Plus spectrophotometer (Shimadzu). The steady-state fluorescence spectra were measured using the Photoluminescence Spectrometer FS5 (Edinburgh Instruments). Absolute fluorescence quantum yields (QYs) were measured with an integrating sphere fluorometer (Quantaurus-QY, Hamamatsu) using 1 cm quartz cuvettes at a set of excitation wavelengths from 530 nm to 700 nm with 10 nm steps. Quantum yields were plotted against excitation wavelength for each protein and the region where the dependence was flat (QY did not depend on wavelength) was selected. QYs are presented as an average of the data obtained in these regions. The peak optical density of the samples was <0.1. The reference (1x PBS buffer only) measurements were done in the same cuvette as was used for the sample measurements.

Fluorescence lifetimes were measured with a digital frequency domain system, ChronosDFD (ISS), as previously described[44]. In brief, fluorescence was excited with a 635 nm laser diode (ISS), modulated at a number of harmonics. LDS798 dye (Exciton) in ethanol (τ = 0.15 ns) was used as a reference standard to obtain the instrumental response function[45]. Fluorescence was collected through a 675/20 filter (Chroma) for emiRFP670, miRFP670, miRFP680 and mCardinal, and through a 700/13 filter (Semrock) for mRhubarb713, iRFP713, miRFP713 and miRFP720. In all cases the fluorescence could be well described with a single exponential decay (χ^2 = 0.6–1.4). Fluorescence lifetimes obtained for mCardinal (τ = 1.38 ns) and iRFP713 (τ = 0.78 ns) were in good agreement with previous measurements (τ = 1.3 ns and 0.63 ms, respectively)[46].

To determine the extinction coefficients, we compared the absorbance for the protein at the Q-band peak with the absorbance of the short wavelength of the Soret peak centered at 370–390 nm assuming the latter to have the extinction coefficient of free biliverdin IXα, which is 39,900 M^{-1} cm^{-1} (ref. 3). Correction to the scattering background ~λ^{-4} was made. The extinction coefficient of mCardinal was measured using the alkaline denaturation method[44]. In addition, the extinction coefficients were calculated using the Strickler–Berg equation. pH titrations were done in the pH range 2.0–11.0 using a series of commercially available pH buffers (Hydron), and fluorescence was measured with the Varioskan LUX plate reader for three technical replicates from one protein purification sample.

For two-photon spectral characterization, we used a previously described optical set-up and protocol[47]. In brief, the set-up includes a tunable (680–1,300 nm) InSight DeepSee Dual femtosecond laser (Spectra Physics) and a photon-counting spectrofluorometer, PC1 (ISS). The same measurement protocol[47] was used for a whole series of the selected NIR FPs to enable a robust direct comparison of their two-photon absorption properties. To measure the two-photon excitation spectrum, the laser wavelength is automatically stepped and the corresponding total fluorescence signal is recorded at each wavelength using our customized LabView program. Well-characterized two-photon standard dye solutions of Coumarin 540A in dimethylsulfoxide and LDS798 in chloroform were used to correct the two-photon spectral profile of the sample for wavelength-to-wavelength variations of laser parameters (spatial intensity distribution and pulse duration).

We used a modification of the previously described method[47] of measurement of the two-photon absorption cross-section (σ_2). In particular, we collected a total (without monochromator) fluorescence signal of the sample and reference, first upon two-photon excitation at a certain wavelength, and then upon one-photon excitation (with a continuous-wave laser) with a visible wavelength matching the absorption spectra of the sample and reference. In these measurements, the sample and the reference solutions are contained in 3 × 3 mm SOG (special optical glass) cuvettes (Starna) and have a maximum optical density of <0.1. The fluorescence is collected at 90° to the excitation laser beam through a set of filters that block both the femtosecond NIR and the visible laser wavelengths, typically including FF01-770/SP, or FF01-842/SP in combination with 561 nm EdgeBasic best-value long-pass filters (all Semrock) using the left emission channel of the spectrofluorometer. We first collected the two-photon excited fluorescence signal I as a function of laser power P for both the sample and reference solutions and fitted them to a quadratic function $I = aP^2$. From these fits, the coefficients a_S and a_R are obtained for the sample (index S) and reference (index R) solutions, respectively. Second, we measured the one-photon excited fluorescence signals as a function of laser power for the same solutions and in the same registration conditions as in the two-photon experiment, and fitted them to a linear function: $I = bP$. The best fits provide coefficients b_S and b_R. The two-photon absorption cross-section was then calculated as follows:

$$\sigma_{2,S}(\lambda_2) = \frac{a_S}{a_R}\frac{b_R}{b_S}\frac{\varepsilon_S(\lambda_1)}{\varepsilon_R(\lambda_1)}\sigma_{2,R}(\lambda_2)$$

Here, λ_1 is the wavelength used for one-photon excitation (561 nm), λ_2 is the wavelength used for two-photon excitation (1,060 or 1,064 nm), and $\varepsilon_{R/S}(\lambda_1)$ are the corresponding extinction coefficients, measured at λ_1. This approach enables us to automatically correct for the laser beam properties (pulse duration and spatial intensity distribution), fluorescence collection efficiencies for one- and two-photon modes, photomultiplier tube spectral sensitivity, and differences in quantum yield and concentration between the sample and reference solutions.

The two-photon absorption cross-sections were measured at 1,060 nm relative to LDS798 in deuterated chloroform, the value of which is 220 GM[29].

Characterization in mice

All animal maintenance and experimental procedures for mice were conducted according to the Westlake University Animal care

guidelines, and all animal studies were approved by the IACUC of Westlake University, Hangzhou, China under animal protocol 19-044-KP. Procedures involving experimental animals are reported in accordance with Animal Research: Reporting of In Vivo Experiments (ARRIVE). Mice were maintained at strict barrier facilities with macroenvironmental temperature and humidity ranges of 20–26 °C and 40–70%, respectively. Food and water were provided ad libitum. The rooms had a 12 h light–12 h dark cycle. The housing conditions were closely monitored and controlled. The selected NIR FPs were expressed in brain and liver of mice and assessed for brightness in vivo and ex vivo. We used C57BL/6 mice supplied by the Animal Facility at Westlake University without regard for sex. For expression of NIR FPs in the brain, we used the neonatal intraventricular injections of custom-made recombinant AAVs, serotype 2/9 (rAAV2/9-CAG-NIR-FPs-P2A-GFP, titer: $>10^{12}$ v.g. ml^{-1}; Shanghai Sunbio Medical Biotechnology) as described previously[48]. In brief, viruses were injected pan-cortically into pups at postnatal day 0 regardless of sex with a Hamilton microliter syringe. To induce hypothermic anesthesia, the pups were put on soft tissue with ice underneath under close monitoring until they stopped responding to gentle squeezing on the limbs. For each hemisphere, 0.5 µl virus solution (titer: $>10^{12}$ v.g. ml^{-1}) supplemented with 0.1% FastGreen dye (Sigma-Aldrich) was injected under the skull manually. After injections in both hemispheres, the pups were moved onto a heating pad maintained at 37°C for a 5 min recovery. After the pups regained response to gentle squeezing, they were returned to the home cages. The whole injection process for each pup was controlled within a few minutes to prevent cannibalism. At least 11 postnatal day 0 mice were injected for each NIR FP. Acute brain slices were obtained from mice injected with AAVs at postnatal days 20–30 as well as at 2 months and 3 months of age using standard techniques as described previously[28].

To assess the intracellular brightness of each protein in the Cy5 and Cy5.5 channels, at least nine live brain slices from three mice were imaged for each time point. To quantify the photostability of each protein, at least three live brain slices were obtained from three 1-month-old mice for each protein. In brief, mice were deeply anesthetized with 1% pentobarbital sodium (8 µl g^{-1}) and perfused transcardially using cold saline (oxygenated with 95% O_2 and 5% CO_2) containing 194 mM sucrose, 30 mM NaCl, 4.5 mM KCl, 1.2 mM NaH_2PO_4, 0.2 mM $CaCl_2$, 2 mM $MgCl_2$, 26 mM $NaHCO_3$, 10 mM D-(+)-glucose, pH 7.4, adjusted with NaOH, 320–340 mOsm l^{-1}. Coronal slices (300–500 µm thick) were cut using a slicer (VT1200 S, Leica Microsystems) and then incubated for 10–15 min in a holding chamber (BSK4, Scientific System Design) at room temperature with regular artificial cerebrospinal fluid (oxygenated with 95% O_2 + 5% CO_2) containing 136 mM NaCl, 3.5 mM KCl, 1 mM $MgCl_2$, 2.5 mM $CaCl_2$, 26 mM $NaHCO_3$ and 11 mM glucose. Slices were then imaged under the incubation of artificial cerebrospinal fluid continuously gassed with 95% O_2 and 5% CO_2 at room temperature. The mean fluorescence intensity was extracted for individual neuronal cell bodies using Nikon Elements software and used for further side-by-side protein comparison. For assessment of intracellular brightness and photostability in fixed brain tissue, we perfused mice using 4% PFA according to the protocol described previously[16]. For the PFA-fixed brain tissue assessment, at least three slices were imaged from two mice for each protein (age of mice was postnatal days 20–30).

For expression of NIR FPs in mouse liver, three 3-month-old mice were injected i.v. via the tail vein with 1 µl rAAV2/9-CAG-NIR-FPs-P2A-GFP (titer: $>10^{12}$ v.g. ml^{-1}) diluted in 100 µl sterile PBS and imaged 5–6 days after injection. Mice were deeply anesthetized and transcardiac perfusion with PBS was carried out to remove blood. Immediately after perfusion, the liver was dissected and imaged using a wide-field microscope in the Cy5 and Cy5.5 channels as described before[49]. For each construct we tested at least three livers. The mean fluorescence intensity was calculated for individual cells. Animals that show no GFP fluorescence were excluded from the study.

Characterization of NIR FPs in neurons of living zebrafish larvae

All experiments involving zebrafish were performed according to European Union guidelines and German legislation (EU Directive 2010_63 and license AZ 325.1.53/56.1-TU-BS). Zebrafish husbandry and breeding were performed according to the standard procedures[50]. The NIR FPs that showed high performance in cultured neurons were expressed transiently in neurons of zebrafish larvae and assessed for their brightness and photostability using zebrafish-specific expression vectors. The neuronal expression vector for these experiments carries two expression components flanked by Tol2 recognition sites[51]. The neuron-specific Gal4 expression unit includes a Gal4 variant KalNFB[38], the expression of which is regulated by a compact, 377-bp-long promoter (*nbt*^{300}*2n*): a 300-bp-long *Xenopus* neuron-specific β-tubulin (*nbt*) gene core promoter (gene bank accession; EF989124, 3182-3481), followed by a 2× neuron restrictive silencer element (2× NRSE: *2n*) in the 5′ untranslated region (5′UTR). The KalNFB gene was linked to three copies of the target site of microRNA1 (3×mir1T) to suppress ectopic expression in muscles[52], followed by SV40 (simian virus 40) polyA. Furthermore, the predicted 3′UTR of zebrafish synaptotagmin 2a was inserted between 3×mir1T and SV40 polyA to enhance the level of expression in neurons (C. Riegler, personal communication). The final construct, named pTol2-*nbt*^{300}*2n*:KalNFB-3xmir1T-syt2a (Addgene 196900) successfully enhanced the neuron specificity of Gal4-UAS-mediated reporter expression by eliminating muscle expression while maintaining high levels of neuronal expression. The resultant construct, designated pTol2-*nbt*^{300}*2n*:KalNFB-3xmir1T-syt2a, was used to insert the following reporter genes as below. The second expression module carries a regulatory element composed of the 10×UAS flanked by two E1b minimal promoters (10×UAS), inducing bidirectional co-expression of transgenes in a Gal4-dependent, cell type-specific manner. To validate neuron-specific co-expression of two reporters inserted into pTol2-*nbt*^{300}*2n*:KalNFB-3xmir1T-syt2a, TagRFP-T and EGFP were cloned into the left hand and right hand of 10×UAS, respectively (Addgene 196116) (Supplementary Fig. 14). For expression of NIR FPs, the mammalian codon-optimized NIR FPs linked to P2A-mClover3 (NIR-FPs-P2A-mClover3) were cloned as one cistron into the right hand of bidirectional 10×UAS (Addgene 196118-196133). As the other cistron, the zebrafish codon-optimized open reading frame (ORF) of wild-type human heme oxygenase 1 (wtHO1), or its catalytically inactive form (HO1-H25A)[53] was inserted into the left hand of 10×UAS (see Supplementary Fig. 14 for the schematics of the expression cassette). The obtained Gal4/UAS construct drove multicistronic transgene expression, enabling the assessment of NIR FP fluorescence in Gal4-expressing neurons with or without HO1 activity. As a control, a construct carrying mCardinal-P2A-mClover3 with neither HO1 nor HO1-H25A was cloned, the expression of which is under the control of 6×UAS (Addgene 196117) (Supplementary Fig. 14).

The generated expression constructs were co-injected with Tol2 transposase mRNA (1.5 nl injection mix containing 25 ng $µl^{-1}$ of both Tol2 plasmid and pTol2 mRNA) into pigmentation-compromised *brass* mutant embryos at the single-cell stage. Injection of this construct together with Tol2 mRNA into zebrafish embryos led to Tol2-transposon-mediated early genomic integration of the transgene, followed by broad expression in neuronal cells of larval zebrafish in a semi-mosaic manner. Injected larvae were screened for green fluorescence throughout the nervous system at 2–3 dpf using a stereomicroscope (Leica Microsystems). Subsequently, larval zebrafish at 4 dpf were sedated with 0.02% Tricain (E10521, Sigma-Aldrich) and embedded in 1.0% low-melting agarose (A9414, Sigma-Aldrich) for imaging. Fluorescence signals of TagRFP-T and EGFP were captured with a fluorescence stereomicroscope (MZ205FA, Leica Microsystems), whereas those for NIR FPs and mClover3 were imaged using a confocal microscope (Leica SP8, Leica Microsystems) with a ×40 1.1NA water immersion objective in the green channel (excitation, 488 nm from

an argon laser; emission, 496–530 nm) and cfCy5-LP channel (excitation, 633 nm from an HeNe laser; emission, 645–780 nm). To quantify the intracellular brightness of NIR FPs in neurons, reconstructions and projections from z-stacks of images were generated, and further processed with Fiji to measure the mean fluorescence intensity in the green and cfCy5-LP channels and calculate the mean NIR FP/mClover3 ratio for individual neurons in the hindbrain and spinal cord. Four individual larval fish were imaged to collect the data from 120 neurons for analysis in total per construct. The mean fluorescence intensity of each NIR FP was calculated, followed by the evaluation of statistically significant differences in brightness and compared with their behavior in cultured cells.

To quantify the photostability of NIR FP fluorescence in zebrafish neurons, four independent 4 dpf larvae co-expressing HO1 and the respective NIR FP underwent confocal microscopy imaging using a ×40 NA1.1 water immersion objective in the cfCy5-LP channel; an ROI was selected (96.88 × 96.88 µm) encompassing 5–10 positive neurons. To collect photobleaching data from 40 neurons (10 cells per larvae), a single plan image (optical section, 1.271 µm) was recorded continuously for 3 min with 70% laser power. Acquired images were processed with Fiji to measure the fluorescence intensity in individual neurons for each time point. The data were excluded from the analysis if zebrafish moved during image recording. Statistically significant differences in brightness were evaluated as described in the **Data Analysis and Statistics** section.

Characterization of NIR FPs in *C. elegans* neurons

The selected NIR FPs were expressed using extrachromosomal arrays in *C. elegans* and assessed for intracellular localization, brightness and photostability in the Cy5-LP and Cy5.5 channels. For expression in *C. elegans*, the target genes were codon-optimized using the *C. elegans* Codon Adapter application (https://worm.mpi-cbg.de/codons/cgi-bin/optimize.py) with insertion of two introns[54] and synthesized de novo (Tsingke Biotechnology). The optimized genes of NIR FPs were cloned into pSF11 vector (Addgene plasmid 179485) under the pan-neuronal *tag-168* promoter in frame with the T2A-HO1 gene (HO1 from *Homo sapiens*). In addition, we cloned the mCardinal gene into the pSF11 vector without the T2A-HO1 gene. The codon-optimized gene of mNeonGreen cloned into the pSF11 vector was used as a reporter marker for screening positive worms and for normalizing NIR fluorescence (cloned by GenScript USA). The establishment of transgenic lines was done by SunyBiotech according to standard protocols. In brief, wild-type N2 worms were co-injected with two plasmids encoding wNIR-FPs-T2A-HO1::wmNeonGreen with a 10 ng µl^{-1} final concentration each. Transgenic lines were selected by green fluorescence and confirmed with sequencing of the target. Selected worms were maintained and grown on nematode growth medium (NGM) plates seeded with *E. coli* OP50-1 at 20 °C following standard protocols. Positive worms with green fluorescence (used without regard to sex) at the L4 stage of development were selected for further imaging. Worms were mounted on immunofluorescence assay slides (Jiangsu Shitai Zhenduan Jishu, 80383-0209-01), immobilized with 25 mM levamisole and imaged using a wide-field Nikon microscope with a ×10 0.45NA objective lens for quantification (exact microscope configuration described above; for Fig. 4b–d and Supplementary Fig. 18) and a Zeiss 980 confocal microscope for structural imaging (×10 0.45NA, ×40 0.95NA, 639 nm excitation laser for NIR, 635–757 nm emission range; for Fig. 4a) controlled by ZEN blue v3.5. Individual neurons were selected manually, and mean fluorescence intensity was calculated using Nikon Elements software.

Multicolor imaging in live zebrafish larvae

To examine the use of NIR FPs for multicolor imaging in vivo, emiRFP670 was chosen based on the result of the intracellular brightness and photostability analysis in zebrafish neurons, and its fusion proteins were co-expressed together with cyan, green and red FPs, each of which labels a different neuronal compartment. To further enhance the expression level, the zebrafish codon-optimized genes of the selected FPs were used. Zebrafish codon-optimized cDNAs of emiRFP670, mClover3 (green FP) and mScarlet-I (red FP) were synthesized de novo by Tsingke Biotechnology. A zebrafish codon-optimized mTurquoise2 (cyan FP) was generated by site-directed mutagenesis of the zebrafish codon-optimized Cerulean gene (Addgene 61389). A zebrafish codon-optimized TagRFP-T (red FP) was kindly provided by H. Burgess (Eunice Kennedy Shriver National Institute of Child Health and Human Development).

The expression cassette encoding dual subcellular reporters labeling plasma membrane and nucleus were composed of an amino-terminal 15-amino acid sequence of Fyn kinase (fused to mScarlet-I or mClover3) and H2B-mTurquoise2, which were linked via a T2A self-cleaving peptide. The resultant cassette was followed by the ocean pout antifreeze protein 3′UTR containing predicted polyadenylation signal (AFP polyA), and further assembled with HO1-SV40 polyA and E1b-10xUAS-E1b into the pTol2-MCS vector backbone[38]. The inserted sequences were flanked by Tol2 transposase recognition sequence (pTol2-HO1-10U-Fyn-mScarlet-I/mClover3-H2B-mTurquoise2; see Fig. 5c for the expression cassette schematics). Similarly, pTol2-HO1-10U-mTurquoise2 and pTol2-10U-Fyn-mClover3-H2B-mTurquoise2 were generated for the cloning of autophagosome–lysosome (Fig. 5d) and synapse (Supplementary Fig. 21) reporters, respectively.

To monitor actin–microtubule cytoskeletal dynamics in growing axons of zebrafish neurons, Lifeact-mClover3–emiRFP670 fusions and microtubule plus-end binding protein 3 (EB3)–emiRFP670 fusions[35,36] were generated for the labeling of F-actin and microtubule plus-ends, respectively.

Lysosomal-associated membrane protein 1 (LAMP1) was fused to the N-terminus of emiRFP670 to generate a reporter labeling the outer lysosomal membrane. A tandem fluorescent autophagic flux sensor, TagRFP-T-mClover3-zebrafish microtubule-associated protein 1-light chain 3 (LC3)-beta (TagRFP-T-mClover3-LC3) mimics mRFP1-EGFP-LC3 (ref. 37) but showed much brighter fluorescence than mRFP1-EGFP-LC3. This sensor visualizes autophagosomes marked with both green and red fluorescence, whereas acidic autolysosomes formed by autophagosome and lysosome fusion, are detected with only red fluorescence based on the different pH stability of these proteins (pK_a = 6.5 and 4.5, for mClover3 and TagRFP-T, respectively, according to the data in FPbase (https://www.fpbase.org)). To visualize presynaptic vesicles, emiRFP670 was fused to the carboxy terminus of zebrafish synaptophysin b (Addgene 74316)[40], followed by 3′UTR of zebrafish tubulinβ5 microtubule subunit gene *(tubb5)* (kindly provided by F. Giudicelli), enhancing the axonal transport of mRNA[55] . Excitatory post-synapse reporter was generated by mScarlet-I fused to zebrafish post-synaptic density protein 95 (PSD95)[41].

Each reporter attached to the SV40 polyA sequence was assembled into pTol2-HO1-10U-Fyn-mScarlet-I-H2B-mTurquoise2, pTol2-HO1-10U-mTurquoise2 or pTol2-10U-Fyn-mClover3-H2B-mTurquoise2 to generate pTol2-F-actin–microtubule plus-ends (1), autophagosome–lysosome (2) or synapse reporters (3), respectively, as below. These constructs carry an insert composed of two bidirectional expression units regulated by 10×UAS, leading to the expression of quadruple fluorescent reporters with or without HO1 (Fig. 5c,d and Supplementary Fig. 21).

1. pTol2-F-actin–microtubule plus-ends reporters, mediating co-expression of Fyn-mScarlet-I, H2B-mTurquoise2, EB3-emiRFP670 and Lifeact-mClover3 together with HO1 (Addgene 196134).
2. pTol2-autophagosome–lysosome reporters, mediating co-expression of cytoplasmic mTurquoise2,

TagRFP-T-mClover3-LC3 and Lamp1-emiRFP670 together with HO1 (Addgene 196135).

3. pTol2-Synapse reporters, mediating co-expression of Fyn-mClover3, H2B-mTurquoise2, synaptophysin b-emiRFP670 and mScarlet-I-PSD95 (Addgene 196899).

pTol2-F-actin–microtubule reporters and pTol2-*nbt*^{300}*2n*:KalNFB-syt2a (Addgene 196901) were co-injected into brass embryos with Tol2 mRNA (1.5 nl injection mix containing 25 ng µl^{-1} for each pTol2 plasmid and Tol2 mRNA). At thirty-three hours post-fertilization (33 hpf), larval fish expressing these reporters were sorted, followed by confocal microscopy image recording of primary motoneurons and their axons using a ×63 1.2NA water immersion objective (Leica SP8). For synapse imaging, pTol2-synapse reporters together with Tol2 mRNA (1.5 nl injection mix containing 25 ng µl^{-1} for each pTol2 plasmid and Tol2 mRNA) were injected into *Tg*(*2xen.cpce-E1B:KALNFB,he1.1:mTagBFP2*) embryos in which KalNFB induces reporter expression in Purkinje cells restrictively[38]. Injected larval fish showing green fluorescence in the cerebellum were sorted at 4 dpf, followed by confocal microscopy image recording of Purkinje cells at 5 dpf using a ×63 1.2NA water immersion objective (Leica SP8). Green and NIR fluorescent emission signals were recorded simultaneously (mClover3: excitation, 488 nm using an argon laser; emission, 490–550 nm; emiRFP670: excitation, 633 nm using a HeNe laser; emission, 641–765 nm), followed by image recording in the cyan (mTurquoise2: excitation, 405 nm using a UV laser; emission, 421–482 nm) and red (mScarlet-I: DPSS 561 nm laser, emission, 570–616 nm) emission ranges. Reconstructions and projections from z-stacks of images were generated by Fiji. For time-lapse imaging of a growing axon tip of a primary motoneuron, images were recorded every 1.29 s in a single focal plane. Acquired images were processed with Fiji, followed by their animation (25 frames per s) using the QuickTime player (Apple). For autophagosome–lysosome imaging, pTol2-autophagosome–lysosome reporters were injected into *Tg*(*2xen.cpce-E1B:KALNFB,he1.1:mTagBFP2*) embryos together with Tol2 mRNA (1.5 nl injection mix containing 25 ng µl^{-1} for each pTol2-plasmid and Tol2 mRNA). At 4 dpf, larval fish expressing each reporter were sorted, sedated with 0.02% Tricain, and embedded in 1.5% low-melting agarose. The larvae were treated with 1.5 µM Rapalink-1 (AmBeed) in 30% Danieau containing 0.02% Tricain for 4 h, followed by imaging of cerebellar Purkinje cells using the Airyscan mode of a ZEISS LSM 880 microscope with an LD C-Apochromat ×63 1.15NA water immersion objective (Zeiss). Each emission signal of the green (mClover3: excitation, 488 nm using an argon laser), cyan (mTurquoise2: excitation, 405 nm using a UV laser), red (TagRFP-T: excitation. 561 nm using a DPSS laser) and NIR (emiRFP670: excitation, 633 nm using a HeNe laser) FP was recorded separately. For the adjustable light path in the Airyscan system, the main beam splitter for the wavelength of 488/561/633 nm was chosen in the visible light path and 405 nm for the invisible light path. To narrow down the detectable fluorescence spectrum, different emission dual filters were used for the detection of blue (BP 465–505 nm and LP 525 nm) and green (BP 495–550 nm and LP 570 nm) fluorophores, while the same filters could be used to detect the emission of both red and NIR (BP 570–620 nm and LP 645 nm) fluorescence, respectively. For image acquisition, the system-defined optimal settings for pixel resolution and Z-stack slice thickness (0.23 µm) were used. The acquired images were processed with the ZEN 2.3 black software and the Zeiss Airyscan processing option. The brightness and contrast were later evenly adjusted across the image with ImageJ.

Data analysis and statistics

Data were analyzed offline using NIS Elements Advance Research software (versions 5.21.00 and 5.30.00), Excel (Microsoft), OriginPro (2019b, OriginLab), GraphPad Prism 8, Fiji ImageJ 2.9.01/1.53t, CytExpert 2.4, Amersham Imager 680 analysis software and the Microscope online application (https://www.fpbase.org/microscope). For fluorescence signal intensity analysis, an ROI including cells, or cell bodies in the case of neurons, and a neighboring cell-free region (as a background) were selected either manually or automatically using NIS Elements Advance Research software. Mean intensity was extracted for each ROI in the Cy5-LP, Cy5-BP, Cy5.5 and FITC channels, and the corresponding background was subtracted. The means of ratios (NIR to green) indicating the normalized intracellular brightness of the fluorescent proteins are reported in all experiments . For OSER assay analysis we counted the total number of cells and the number of cells that contain whorl fluorescent structures, which are visibly distinct from endoplasmic reticular networks. For photostability in *C. elegans* the data were corrected for movement using the ImageJ plugin Time Series Analyzer V3 (https://imagej.nih.gov/ij/plugins/time-series.html). For photostability in cultured neurons and live brain slices, the data were corrected for movement using the ImageJ plugin Template matching (https://imagej.nih.gov/ij/plugins/template-matching.html). All statistics were performed in JMP (SAS), OriginPro or R (the R Foundation). The Shapiro–Wilk test was used for the normal distribution test for datasets with $n < 5{,}000$. For datasets where sample size exceeded 5,000, the Kolmogorov–Smirnov test for normality was used instead of the Shapiro–Wilk test. The Kolmogorov–Smirnov and Dunn's tests were used for pairwise comparison instead of the Nemenyi test, given that the datasets under comparison did not have equal size. Moreover, we performed a power analysis using 5 out of 22 proteins spanning from mNeptune2.5 to miRFP720 to determine the minimum sample size needed to produce a statistically significant experiment (Supplementary Table 1). $P < 0.05$ was considered statistically significant (see Supplementary Data 1 for detailed statistics).

Statistics and reproducibility

Due to limited space in the figure legends, we present in detail in this section the sample size, number of independent experiments, statistical tests used with their parameters and exact *P* values. For Fig. 1a three independent transfections were performed for each protein and a total of $n = 1{,}945$ cells for mNeptune2.5, $n = 4{,}841$ cells for mCardinal, $n = 3{,}562$ cells for E2-Crimson, $n = 5{,}930$ cells for smURFP, $n = 6{,}230$ cells for BDFP1.6, $n = 6{,}658$ cells for emiRFP670, $n = 6{,}035$ cells for miRFP670-2, $n = 8{,}911$ cells for iRFP670, $n = 4{,}770$ cells for miRFP680, $n = 5{,}118$ cells for iRFP682, $n = 3{,}325$ cells for emiRFP703, $n = 5{,}970$ cells for BDFP1.8, $n = 4{,}417$ cells for miRFP2, $n = 5{,}439$ cells for mIFP, $n = 6{,}060$ cells for IFP2, $n = 4{,}831$ cells for mRhubarb713, $n = 4{,}819$ cells for miRFP713, $n = 5{,}771$ cells for iRFP713, $n = 5{,}965$ cells for SNIFP, $n = 6{,}192$ cells for mRhubarb719, $n = 4{,}619$ cells for mRhubarb720, and $n = 4{,}116$ cells for miRFP720 were analyzed. Kruskal–Wallis ANOVA was performed with 95% confidence intervals (alpha = 5%, one-sided), d.f. = 21, chi-squared = 74,637.94216, $P = 0$. For pairwise comparison the Kolmogorov–Smirnov was performed with 95% confidence intervals, two-sided. Exact D, Z and *P* values are provided in Supplementary Dataset 1 for each pair.

For Fig. 1b three independent transfections were performed for each protein and a total of $n = 99$ cells for mNeptune2.5, $n = 100$ cells for mCardinal, $n = 94$ cells for E2-Crimson, $n = 100$ cells for smURFP, $n = 113$ cells for BDFP1.6, $n = 117$ cells for emiRFP670, $n = 111$ cells for miRFP670-2, $n = 110$ cells for iRFP670, $n = 98$ cells for miRFP680, $n = 113$ cells for iRFP682, $n = 98$ cells for emiRFP703, $n = 98$ cells for BDFP1.8, $n = 110$ cells for miRFp2, $n = 101$ cells for mIFP, $n = 110$ cells for IFP2, $n = 97$ cells for mRhubarb713, $n = 103$ cells for miRFP713, $n = 96$ cells for iRFP713, $n = 110$ cells for SNIFP, $n = 107$ cells for mRhubarb719, $n = 114$ cells for mRhubarb720 and $n = 108$ cells for miRFP720 were analyzed. Kruskal–Wallis ANOVA was performed with 95% confidence intervals (alpha = 5%, one-sided), d.f. = 21, chi-squared = 2,154.8492, $P = 0$. For pairwise comparison the Kolmogorov–Smirnov test was performed with 95% confidence intervals, two-sided. Exact D, Z and *P* values are provided in Supplementary Dataset 1 for each pair.

For Fig. 1d two independent transductions were performed for each protein and a total of $n = 44$ neurons for mNeptune2.5, $n = 48$ neurons for mCardinal, $n = 45$ neurons for E2-Crimson, $n = 50$ neurons for smURFP, $n = 50$ neurons for BDFP1.6, $n = 51$ neurons for emiRFP670, $n = 57$ neurons for miRFP670-2, $n = 53$ neurons for iRFP670, $n = 53$ neurons for miRFP680, $n = 51$ neurons for iRFP682, $n = 48$ neurons for emiRFp703, $n = 46$ neurons for BDFP1.8, $n = 52$ neurons for miRFP2, $n = 51$ neurons for mIFP, $n = 53$ neurons for IFP2, $n = 46$ neurons for mRhubarb713, $n = 50$ neurons for miRFP713, $n = 49$ neurons for iRFP713, $n = 50$ neurons for SNIFP, $n = 45$ neurons for mRhubarb719, $n = 47$ neurons for mRhubarb720 and $n = 51$ neurons for miRFP720 were analyzed. Kruskal–Wallis ANOVA was performed with 95% confidence intervals (alpha = 5%, one-sided), d.f. = 21, chi-squared = 887.75808, $P = 2.14 \times 10^{-174}$. For pairwise comparison Dunn's test was used. Exact Z and P values are provided in Supplementary Dataset 1 for each pair.

For Fig. 1e two independent transductions were performed for each protein and a total of $n = 45$ neurons for mNeptune2.5, $n = 46$ neurons for mCardinal, $n = 50$ neurons for E2-Crimson, $n = 50$ neurons for smURFP, $n = 53$ neurons for BDFP1.6, $n = 54$ neurons for emiRFP670, $n = 51$ neurons for miRFP670-2, $n = 56$ for iRFP670, $n = 52$ neurons for miRFP680, $n = 44$ neurons for iRFP682, $n = 53$ neurons for emiRFP703, $n = 54$ neurons for BDFP1.8, $n = 53$ neurons for miRFP2, $n = 46$ neurons for mIFP, $n = 43$ neurons for IFP2, $n = 43$ neurons for mRhubarb713, $n = 49$ neurons for miRFP713, $n = 55$ neurons for iRFP713, $n = 54$ neurons for SNIFP, $n = 50$ for mRhubarb719, $n = 41$ neurons for mRhubarb720 and $n = 49$ neurons for miRFP720 were analyzed. Kruskal–Wallis ANOVA was performed with 95% confidence intervals (alpha = 5%, one-sided), d.f. = 21, chi-squared = 1,056.94323, $P = 2.04 \times 10^{-210}$. For pairwise comparison Dunn's test was used. Exact Z and P values are provided in Supplementary Dataset 1 for each pair.

For Fig. 1g two independent transfections were performed for each protein and a total of $n = 3{,}540$ cells for mNeptune2.5, $n = 3{,}670$ cells for mCardinal, $n = 3{,}494$ cells for E2-Crimson, $n = 5{,}642$ cells for smURFP, $n = 3{,}511$ cells for BDFP1.6, $n = 2{,}610$ cells for emiRFP670, $n = 3{,}437$ cells for miRFP670-2, $n = 4{,}554$ cells for iRFp670, $n = 2{,}372$ cells for miRFP680, $n = 4{,}525$ cells for iRFP682, $n = 4{,}328$ cells for emiRFP703, $n = 4{,}596$ cells for BDFP1.8, $n = 1{,}974$ cells for miRFP2, $n = 5{,}483$ cells for mIFP, $n = 3{,}291$ cells for IFP2, $n = 5{,}539$ cells for mRhubarb713, $n = 2{,}364$ cells for miRFP713, $n = 3{,}297$ cells for iRFP713, $n = 4{,}958$ cells for SNIFP, $n = 2{,}997$ cells for mRhubarb719, $n = 2{,}351$ cells for mRhubarb720 and $n = 2{,}309$ cells for miRFP720 were analyzed. Kruskal–Wallis ANOVA was performed with 95% confidence intervals (alpha = 5%, one-sided), d.f. = 21, chi-squared = 62,899.97851, $P = 0$. For pairwise comparison the Kolmogorov–Smirnov test as performed with 95% confidence intervals, two-sided. Exact D, Z and P values are provided in Supplementary Dataset 1 for each pair.

For Fig. 2b three mice were used for each protein and a total of $n = 212$ neurons for mCardinal, $n = 171$ neurons for emiRFP670, $n = 316$ neurons for miRFP670-2, $n = 281$ neurons for miRFP680, $n = 221$ neurons for mRhubarb713, $n = 276$ neurons for miRFP713, $n = 272$ neurons for iRFP713 and $n = 206$ neurons for miRFP720 were analyzed. Kruskal–Wallis ANOVA was performed with 95% confidence intervals (alpha = 5%, one-sided), d.f. = 7, chi-squared = 1,386.5542, $P = 3.13 \times 10^{-295}$. For pairwise comparison Dunn's test was used. Exact Z and P values are provided in Supplementary Dataset 1 for each pair.

For Fig. 2c three mice were used for each protein and a total of $n = 324$ neurons for mCardinal, $n = 279$ neurons for emiRFp670, $n = 386$ neurons for miRFP670-2, $n = 344$ neurons for miRFP680, $n = 442$ neurons for mRhubarb713, $n = 346$ neurons for miRFP713, $n = 420$ neurons for iRFP713 and $n = 406$ neurons for miRFp720 were analyzed. Kruskal–Wallis ANOVA was performed with 95% confidence intervals (alpha = 5%, one-sided), d.f. = 7, chi-squared = 2,167.50951, $P = 0$. For pairwise comparison Dunn's test was used. Exact Z and P values are provided in Supplementary Dataset 1 for each pair.

For Fig. 2d three mice were used for each protein and a total of $n = 100$ neurons for mCardinal, $n = 237$ neurons for emiRFP670, $n = 349$ neurons for miRFP670-2, $n = 213$ neurons for miRFP680, $n = 310$ neurons for mRhubarb713, $n = 204$ neurons for miRFP713, $n = 182$ neurons for iRFP713 and $n = 386$ neurons for miRFP720 were analyzed. Kruskal–Wallis ANOVA was performed with 95% confidence intervals (alpha = 5%, one-sided), d.f. = 7, chi-squared = 1,454.88547, $P = 0$. For pairwise comparison Dunn's test was used. Exact Z and P values are provided in Supplementary Dataset 1 for each pair.

For Fig. 2e two mice were used for each protein and a total of $n = 213$ neurons for mCardinal, $n = 98$ neurons for emiRFP670, $n = 252$ neurons for miRFP670-2, $n = 146$ neurons for miRFP680, $n = 190$ neurons for mRhubarb713, $n = 124$ neurons for miRFP713, $n = 149$ neurons for iRFP713 and $n = 92$ neurons for miRFP720 were analyzed. Kruskal–Wallis ANOVA was performed with 95% confidence intervals (alpha = 5%, one-sided), d.f. = 7, chi-squared = 1,019.60205, $P = 7.00 \times 10^{-216}$. For pairwise comparison Dunn's test was used. Exact Z and P values are provided in Supplementary Dataset 1 for each pair.

For Supplementary Fig. 1g $P_{\text{miRFP680-P2A-EGFP}} = 0.06645$, $P_{\text{miRFP680-IRES-EGFP}} = 0.00114$, $P_{\text{miRFP680-Linker-EGFP}} = 4.04404 \times 10^{-21}$, $P_{\text{miRFP680-Linker-EGFP-P2A-FusionRed}} = 1.69504 \times 10^{-4}$, inset $P_{\text{miRFP680-Linker-EGFP-P2A-FusionRed}} = 4.87479 \times 10^{-147}$.

Reporting summary

Further information on research design is available in the Nature Portfolio Reporting Summary linked to this article.

Data availability

The mass spectrometry proteomics data generated in this study have been deposited in the iProX database with the dataset identifier IPX0005767000 (https://www.iprox.cn//page/SCV017.html?query=IPX0005767000). The total size of the files acquired for this study was about 2 TB, which exceeds the limit of the FigShare repository, therefore only the most essential raw datasets, that is, the raw images with metadata supporting the results in Figs. 1–5, Extended Data Figs. 1–7 and Supplementary Figs. 2, 3, 5, 7, 9, 11 are available at FigShare (https://figshare.com/authors/Hanbin_Zhang/14524646 and https://doi.org/10.6084/m9.figshare.21975770). The rest of the files are available from the corresponding author upon request. Source data files are provided with this paper. All plasmids used in this study are available from Addgene and WeKwikGene (https://wekwikgene.wllsb.edu.cn/). Source data are provided with this paper.

Code availability

The custom MatLab code for analysis photostability data is available at Zenodo (https://doi.org/10.5281/zenodo.7992722).

References

43. Papadaki, S. et al. Dual-expression system for blue fluorescent protein optimization. *Sci. Rep.* **12**, 10190 (2022).
44. Drobizhev, M. et al. Local electric field controls fluorescence quantum yield of red and far-red fluorescent proteins. *Front. Mol. Biosci.* **8**, 633217 (2021).
45. Luchowski, R. et al. Instrument response standard in time-resolved fluorescence. *Rev. Sci. Instrum.* **80**, 033109 (2009).
46. Canty, L., Hariharan, S., Liu, Q., Haney, S. A. & Andrews, D. W. Peak emission wavelength and fluorescence lifetime are coupled in far-red, GFP-like fluorescent proteins. *PLoS One* **13**, e0208075 (2018).
47. Drobizhev, M., Molina, R. S. & Hughes, T. E. Characterizing the two-photon absorption properties of fluorescent molecules in the 680–1300 nm spectral range. *Bio Protoc.* **10**(2), e3498 (2020).
48. Kim, J.-Y., Grunke, S. D., Levites, Y., Golde, T. E. & Jankowsky, J. L. Intracerebroventricular viral injection of the neonatal mouse brain for persistent and widespread neuronal transduction. *J. Vis. Exp.* **15**(91), 51863 (2014).

49. Shu, X. et al. Mammalian expression of infrared fluorescent proteins engineered from a bacterial phytochrome. *Science* **324**, 804–807 (2009).
50. Westerfield, M. *The Zebrafish Book. A Guide for the Laboratory Use of Zebrafish* (Danio rerio), 5th edn (Univ. Oregon Press, 2007).
51. Urasaki, A., Morvan, G. & Kawakami, K. Functional dissection of the Tol2 transposable element identified the minimal cis-sequence and a highly repetitive sequence in the subterminal region essential for transposition. *Genetics* **174**, 639–649 (2006).
52. Mishima, Y. et al. Zebrafish miR-1 and miR-133 shape muscle gene expression and regulate sarcomeric actin organization. *Genes Dev.* **23**, 619–632 (2009).
53. Ishikawa, K., Sato, M., Ito, M. & Yoshida, T. Importance of histidine residue 25 of rat heme oxygenase for its catalytic activity. *Biochem. Biophys. Res. Commun.* **182**, 981–986 (1992).
54. Green, R. A. et al. Expression and imaging of fluorescent proteins in the *C. elegans* gonad and early embryo. *Methods Cell Biol.* **85**, 179–218 (2008).
55. Baraban, M., Anselme, I., Schneider-Maunoury, S. & Giudicelli, F. Zebrafish embryonic neurons transport messenger RNA to axons and growth cones in vivo. *J. Neurosci.* **33**, 15726–15734 (2013).
56. Strack, R. L. et al. A rapidly maturing far-red derivative of DsRed-Express2 for whole-cell labeling. *Biochemistry* **48**, 8279–8281 (2009).
57. Rodriguez, E. A. et al. A far-red fluorescent protein evolved from a cyanobacterial phycobiliprotein. *Nat. Methods* **13**, 763–769 (2016).
58. Ding, W. L. et al. Far-red acclimating cyanobacterium as versatile source for bright fluorescent biomarkers. *Biochim. Biophys. Acta Mol. Cell Res.* **1865**, 1649–1656 (2018).
59. Yu, D. et al. An improved monomeric infrared fluorescent protein for neuronal and tumour brain imaging. *Nat. Commun.* **5**, 3626 (2014).
60. Rogers, O. C., Johnson, D. M. & Firnberg, E. mRhubarb: engineering of monomeric, red-shifted, and brighter variants of iRFP using structure-guided multi-site mutagenesis. *Sci. Rep.* **9**, 15653 (2019).

Acknowledgements

The authors thank J. Pan, J. Hu, X. Bai and the Mass Spectrometry and Metabolomics Core Facility of Westlake University for protein sample mass spectrometry analysis. The authors also thank Z. Dong from Westlake University for help with the interpretation of the mass spectrometry results; the Laboratory Animal Resources Center, the Flow Cytometry Core Facility and the Microscopy Core Facility in Westlake University. Henrietta Lacks, and the HeLa cell line that was established from her tumor cells without her knowledge or consent in 1951, have made significant contributions to scientific progress and advances in human health. We are grateful to Henrietta Lacks, now deceased, and to her surviving family members for their contributions to biomedical research. This work is supported by start-up funding from the Foundation of Westlake University, National Natural Science Foundation of China grant 32050410298 and 32171093, 2020 BBRF Young Investigator Grant 28961, and MRIC Funding 103536022023 to K.D.P., the German Research Foundation (DFG, K1949/7-2) project 241961032 and VW-Vorab des Landes Niedersachsen (project HomeoHirn(ZN3673)) to R.W.K., the Foundation of Westlake University and the National Natural Science Foundation of China grant 32071151 to L.W., and the NIH BRAIN program U24NS109107 grant to M.D.

Author contributions

H.Z. and S.P. performed characterization in cultured mammalian cells. X.S. characterized proteins in the expansion microscopy protocols. M.D. and H.Z. characterized proteins in vitro. H.Z. and X.S. performed the mouse experiments, X.W., M.R., R.W.K. and K.N. performed the zebrafish experiments, S.P., L.Y. and L.W. performed the *C. elegans* experiments. H.Z., S.P. and K.D.P. analyzed the data and wrote the manuscript with input from all of the authors. K.D.P. designed and oversaw all aspects of the project.

Competing interests

K.D.P. is the co-founder of a company that pursues commercial applications of expansion microscopy and is listed as an inventor on several patent applications concerning development of new expansion microscopy methods. All other authors have no competing interests.

Additional information

Extended data are available for this paper at https://doi.org/10.1038/s41592-023-01975-z.

Supplementary information The online version contains supplementary material available at https://doi.org/10.1038/s41592-023-01975-z.

Correspondence and requests for materials should be addressed to Kiryl D. Piatkevich.

Peer review information *Nature Methods* thanks Erik Snapp, Lin Tian, and the other, anonymous, reviewer for their contribution to the peer review of this work. Primary Handling Editor: Rita Strack, in collaboration with the *Nature Methods* team.

https://doi.org/10.1038/s41592-023-01975-z

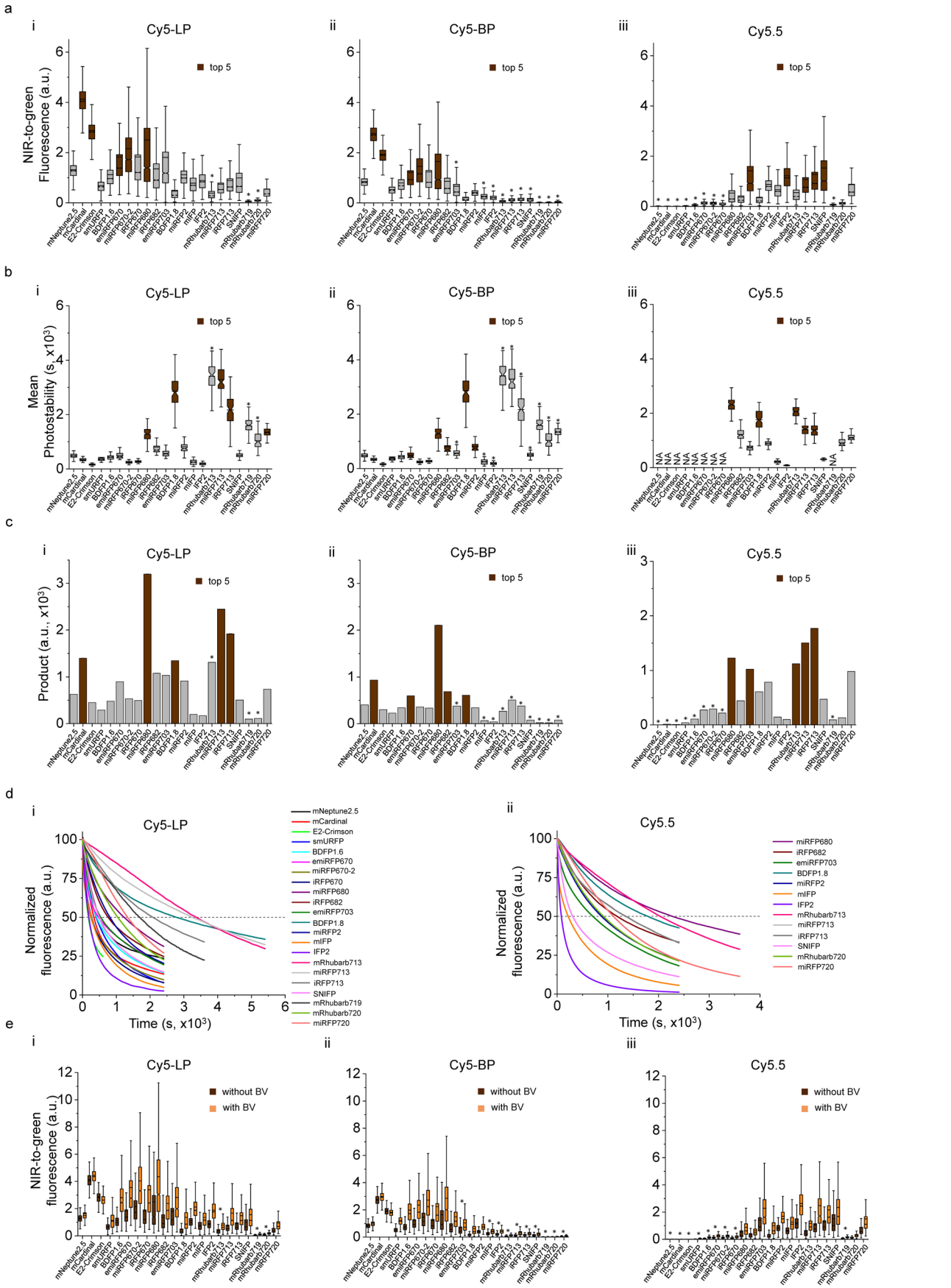

Extended Data Fig. 1 | See next page for caption.

https://doi.org/10.1038/s41592-023-01975-z

Extended Data Fig. 1 | Quantitative assessment of intracellular brightness and photostability of NIR FPs in live HEK cells. (**a**) Intracellular normalized brightness of NIR FPs imaged in three channels: (i) Cy5-LP, (ii) Cy5-BP and (iii) Cy5.5 under 55 mW/mm^2 excitation power (n > 2000 cells for each NIR-FP from three independent transfections in each channel). Brightness for each FP was normalized to the EGFP signal (here and in panel **e**). Asterisks (*) indicate signal-to-background ratio <2.0 throughout; in panels **a-c** box plots highlighted with brown correspond to top 5 NIR FPs for each panel. (**b**) Photobleaching half-times of NIR-FPs under Cy5 (i and ii, excitation power 58 mW/mm^2) and Cy5.5 (iii, excitation power 56–58 mW/mm^2; n > 93 cells for each NIR-FP from four independent transfections). (**c**) Product of mean brightness and mean half-time fluorescence presented as bar graph (mean ± SEM) (due to small value of SEM the error bars are not visible for some bars). (**d**) Normalized photobleaching curves of NIR FPs under (i) Cy5 (excitation power 58 mW/mm^2) and (ii) Cy5.5 (excitation power 56–58 mW/mm^2) illumination for the results shown in panel **b** (n > 93 cells for each NIR-FP from four independent transfections in each channel). Fluorescence was normalized to the intensity value of corresponding FP at t = 0 s. NIR FPs that exhibited signal-to-background ratio lower than 2.0 in Cy5.5 channel are not shown in the graph, however the corresponding curves are available in the source datasets except for mNeptune2.5, which was not visible in Cy5.5 channel at all and thus was not measured. (**e**) Side-by-side normalized brightness comparison without and with BV administration imaged in (i) Cy5-LP, (ii) Cy5-BP and (iii) Cy5.5 under 55 mW/mm^2 excitation power (n > 2000 cells for each NIR-FP from three independent transfections in each channel). Outliers not shown but included in all calculations and available in the source datasets. See Supplementary Table 2 and Supplementary Dataset 1 for the detailed descriptive statistics and exact p-values.

https://doi.org/10.1038/s41592-023-01975-z

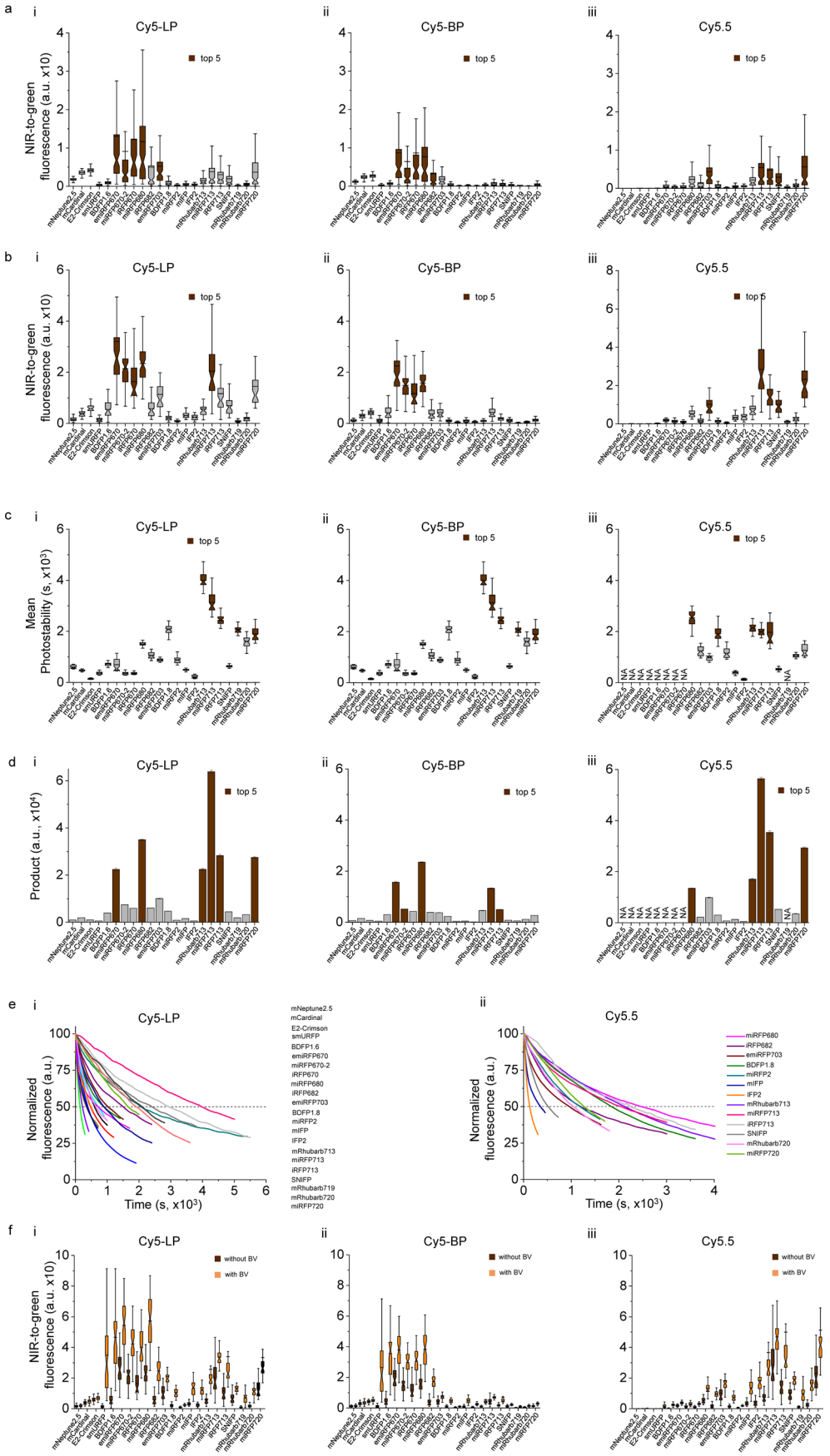

Extended Data Fig. 2 | See next page for caption.

https://doi.org/10.1038/s41592-023-01975-z

Extended Data Fig. 2 | Quantitative assessment of intracellular brightness and photostability NIR FPs in live primary cultured mouse neurons. (**a**, **b**) Intracellular normalized brightness of NIR FPs imaged after (**a**) Calcium Phosphate transfection and (**b**) viral transduction in Cy5-LP, (ii) Cy5-BP and (iii) Cy5.5 under 55 mW/mm^2 excitation power (n > 40 neurons for each NIR FP from two independent cultures). Brightness for each FP was normalized to the EGFP signal (here and in panel **f**). In panels **a**-**d** box plots highlighted with brown correspond to top 5 NIR FPs for each panel. (**c**) Photobleaching half-times of NIR FPs under Cy5 (i and ii, excitation power 55 mW/mm^2) and Cy5.5 (iii, excitation power 55 mW/mm^2; n > 42 neurons for each NIR FP from two independent cultures). NA – not applicable due to low fluorescence signal. (**d**) Product of mean brightness and mean half-time fluorescence presented in bar graph (mean ± SEM) (due to small value of SEM the error bars are not visible for some bars). (**e**) Normalized photobleaching curves of NIR-FPs under (i) Cy5 (excitation power 55 mW/mm^2) and (ii) Cy5.5 (excitation power 55 mW/mm^2) illumination for the results shown in **c**. Fluorescence was normalized to the intensity value of corresponding FP at t = 0 s. (**f**) Side-by-side normalized brightness comparison before and after BV administration imaged in (i) Cy5-LP, (ii) Cy5-BP and (iii) Cy5.5 under 55 mW/mm^2 power (n > 20 neurons for each NIR FP from two independent cultures). see Supplementary Dataset 1 for the detailed descriptive statistics and exact p-values.

https://doi.org/10.1038/s41592-023-01975-z

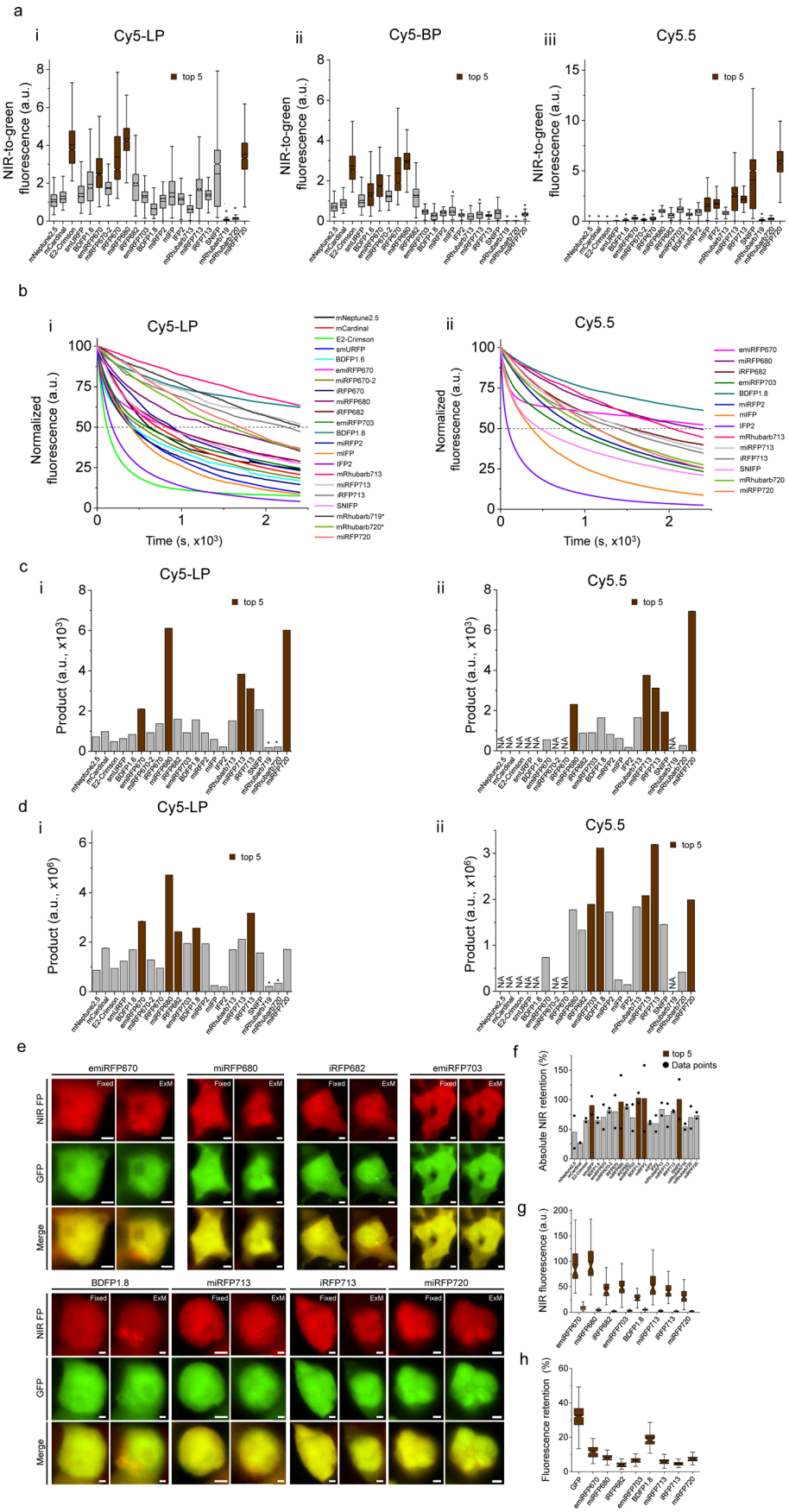

Extended Data Fig. 3 | See next page for caption.

https://doi.org/10.1038/s41592-023-01975-z

Extended Data Fig. 3 | Quantitative characterization of NIR FPs in fixed HEK cells. (**a**) NIR-to-green fluorescence ratio in fixed HEK cells imaged in (i) Cy5-LP, (ii) Cy5-BP and (iii) Cy5.5 under 55 mW/mm^2 excitation power (n > 1976 cells for each NIR FP from two independent transfections in each channel). Brightness for each FP was normalized to the EGFP signal. Asterisks (*) indicate signal-to-background ratio <2.0 throughout the figure based on brightness of fixed HEK cells; in panels **a**, **c**, **d** box plots highlighted with brown correspond to top 5 NIR FPs for each panel. (**b**) Normalized photobleaching curves of NIR FPs under (i) Cy5 (excitation power 55 mW/mm^2) and (ii) Cy5.5 (excitation power 55 mW/mm^2) illumination in fixed HEK cells (n = 40 cells for each NIR FP from two independent transfections in each channel). Fluorescence was normalized to the intensity value of corresponding FP at t = 0 s. NIR FPs that exhibited lower than 2.0 signal-to-background ratio in Cy5.5 channel are not shown in the graph; however, the corresponding curves are available in the source datasets. (**c**) The products of mean NIR-to-green fluorescence ratio and mean fluorescence half-time in (i) Cy5-LP and (ii) Cy5.5 are presented in the form of bar graph (mean ± SE). (**d**) The products of mean absolute NIR brightness to mean fluorescence half-time in (i) Cy5-LP and (ii) Cy5.5 are presented in the form of bar graph (mean ± SE). (**e**) Comparison of selected NIR FPs in proExM. (**e**) Representative images of NIR FPs in PFA-fixed and proExM treated HEK cells acquired in Cy5-LP (NIR FP) and FITC (GFP) channels (n > 61 cells for each NIR FP from one independent transfection). The dynamic brightness range was adjusted independently to facilitate visualization of transfected cells in fixed and proExM processes for each NIR FPs. Images were obtained through single-plane scanning and without projection processing. (**f**) Fluorescence retention of NIR FPs in HEK cells upon PFA fixation presented as bar graph (mean of NIR retention for each protein) (Cy5-LP, n > 1974 cells for each NIR FP from two independent transfections). Black dots indicate ratio of mean brightness before and after fixation for two transfections. (**g**) Absolute NIR fluorescence of fixed (brown box plots with notches) and proExM treated (orange box plots with notches) HEK cells (n > 61 cells for each NIR FP from one independent transfection). (**h**) Retention of GFP and NIR FPs' fluorescence in fixed HEK cells after proExM treatment (n > 61 cells for each NIR FP from one independent transfection). See Supplementary Table 2 and Supplementary Dataset 1 for the detailed descriptive statistics and exact p-values.

https://doi.org/10.1038/s41592-023-01975-z

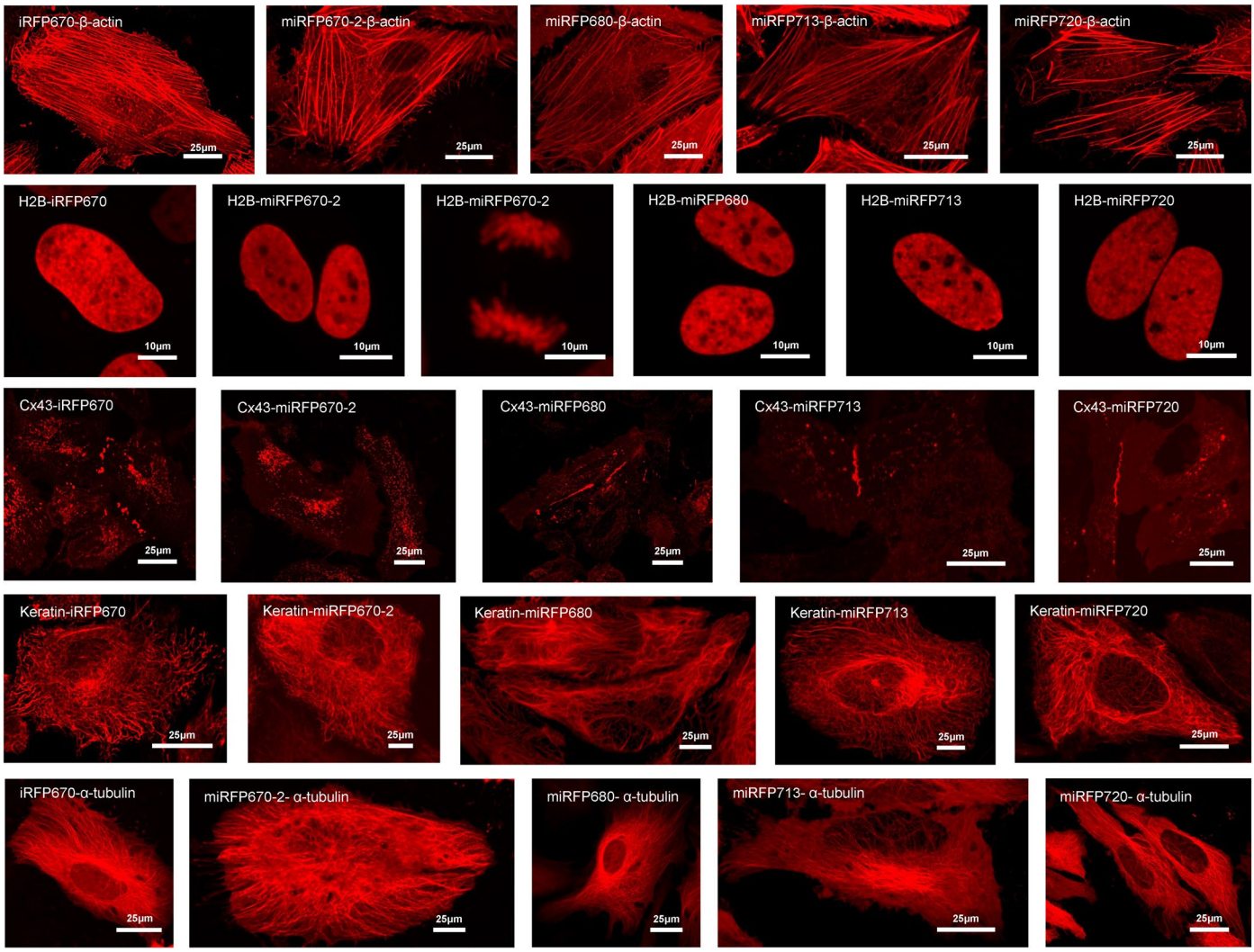

Extended Data Fig. 4 | Fluorescence imaging of NIR FPs fusions in live HeLa cells. Representative images of (from top left) iRFP670-actin, miRFP670-2-actin, miRFP680-actin, miRFP713-actin, miRFP720-actin, H2B-iRFP670, H2B-miRFP670-2, H2B-miRFP680, H2B-miRFP713, H2B-miRFP720, Cx43-iRFP670, Cx43-miRFP670-2, Cx43-miRFP680, Cx43-miRFP713, Cx43-miRFP720, keratin-iRFP670, keratin-miRFP670-2, keratin-miRFP680, keratin-miRFP713, keratin-miRFP720, iRFP670-tubulin, miRFP670-2-tubulin, miRFP680-tubulin, miRFP713-tubulin, miRFP720-tubulin (n > 15 cells for each construct from two independent transfection). For each image the dynamic range was adjusted independently to facilitate visualization and images were generated through maximum projection.

https://doi.org/10.1038/s41592-023-01975-z

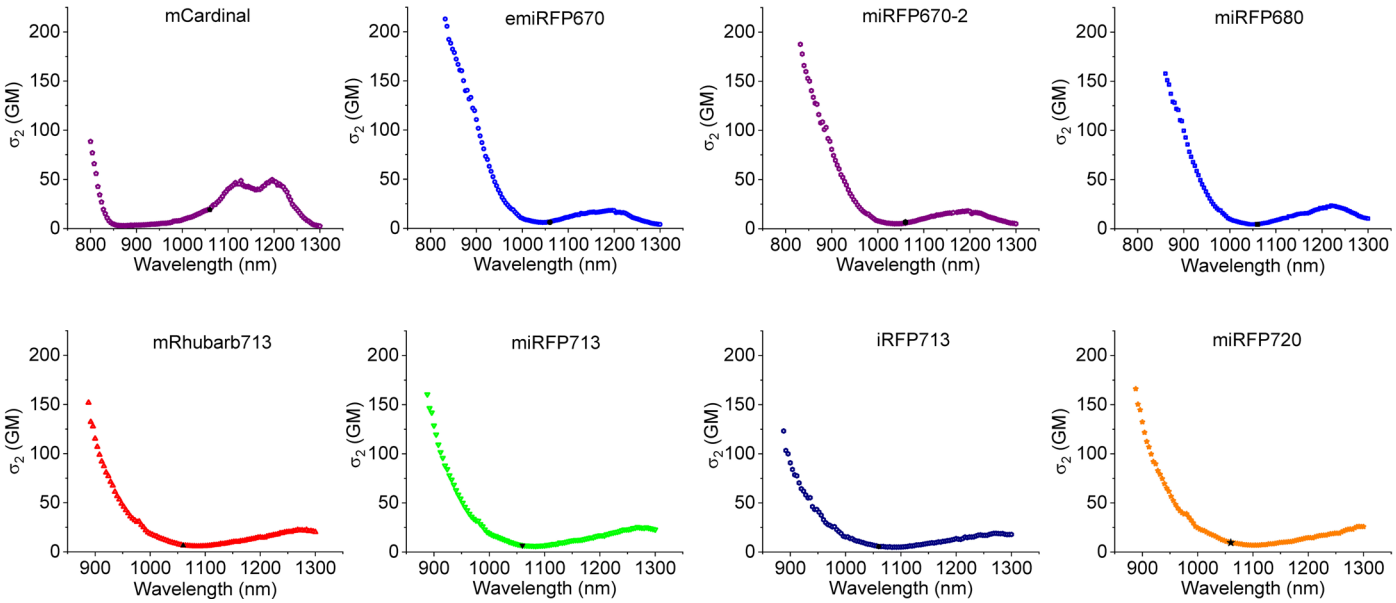

Extended Data Fig. 5 | Two-photon cross-section spectra of selected NIR-FPs. Two-photon cross-section spectra of mCardinal, emiRFP670, miRFP670-2, miRFP680, mRhubarb713, miRFP713, iRFP713, and miRFP720 presented versus laser wavelength used for excitation (GM, Goeppert-Mayer units).

https://doi.org/10.1038/s41592-023-01975-z

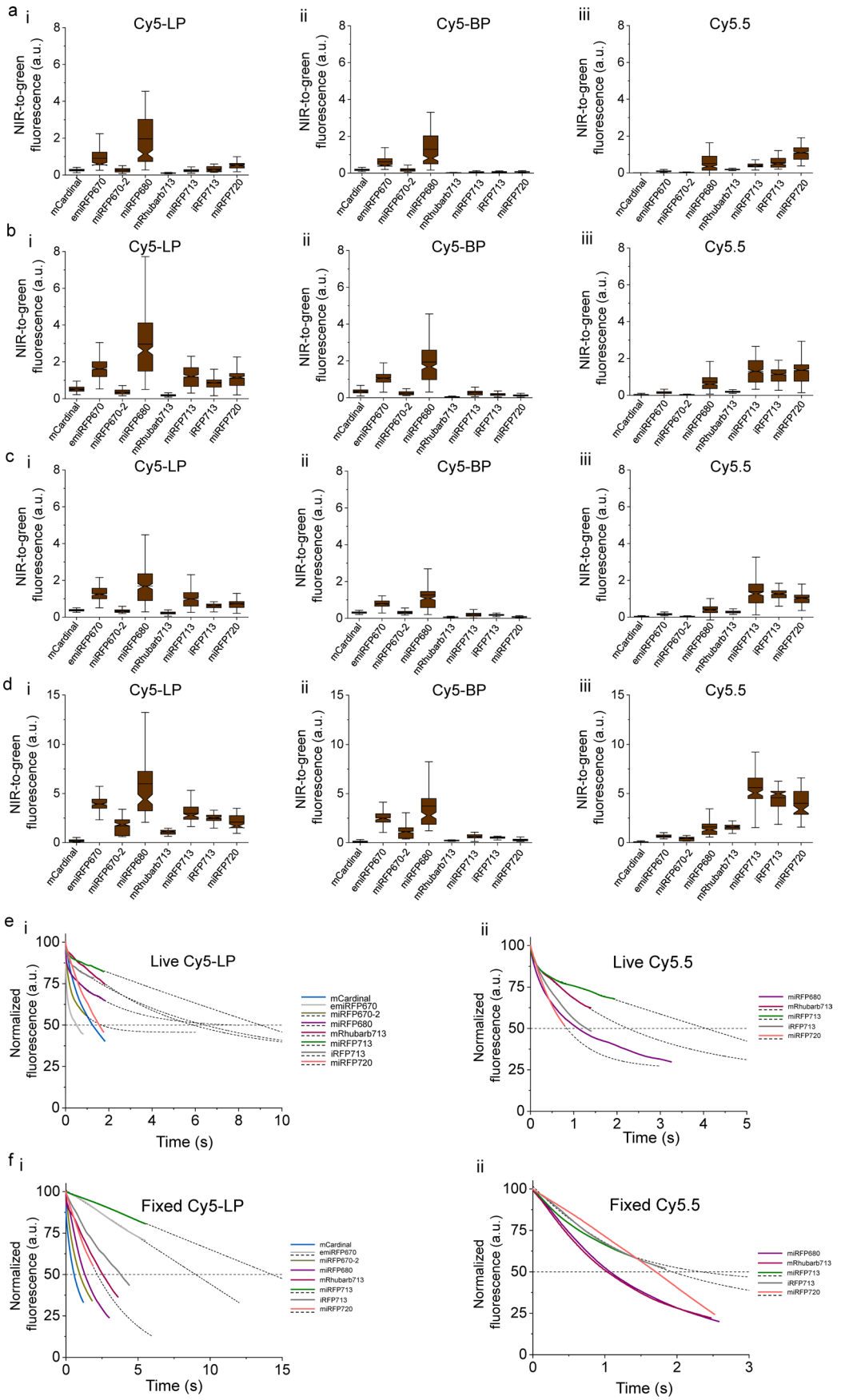

Extended Data Fig. 6 | See next page for caption.

https://doi.org/10.1038/s41592-023-01975-z

Extended Data Fig. 6 | Quantitative characterization of the selected NIR FPs expressed in L2/3 cortical neurons in mouse brain tissue. (**a, b, c**) Intracellular normalized brightness of NIR FPs imaged in acute brain slices from (a) one-month, (b) two-month, (c) three-month old mice in (i) Cy5-LP, (ii) Cy5-BP, (iii) Cy5.5 channels (excitation power 55 mW/mm2; n ≥ 100 neurons from 3 mice for each protein in each channel). Brightness for each FP was normalized to the EGFP signal (here and in panel d). (**d**) Intracellular normalized brightness of NIR-FPs imaged in PFA-fixed brain slices from one-month old mice in (i) Cy5-LP, (ii) Cy5-BP, (ii) Cy5.5 (excitation power 55 mW/mm2; n > 90 neurons from 2 mice for each protein in each channel). (**e, f**) Normalized photobleaching curves of NIR-FPs measured in (e) acute brain slices and (f) PFA-fixed brain slices in (i) Cy5-LP and (ii) Cy5.5 channels (excitation power 55 mW/mm2; n > 40 neurons from 2 mice for each protein for each channel). Fluorescence was normalized to the intensity value of corresponding FP at t = 0 s. See Supplementary Dataset 1 for the detailed descriptive statistics and exact p-values.

https://doi.org/10.1038/s41592-023-01975-z

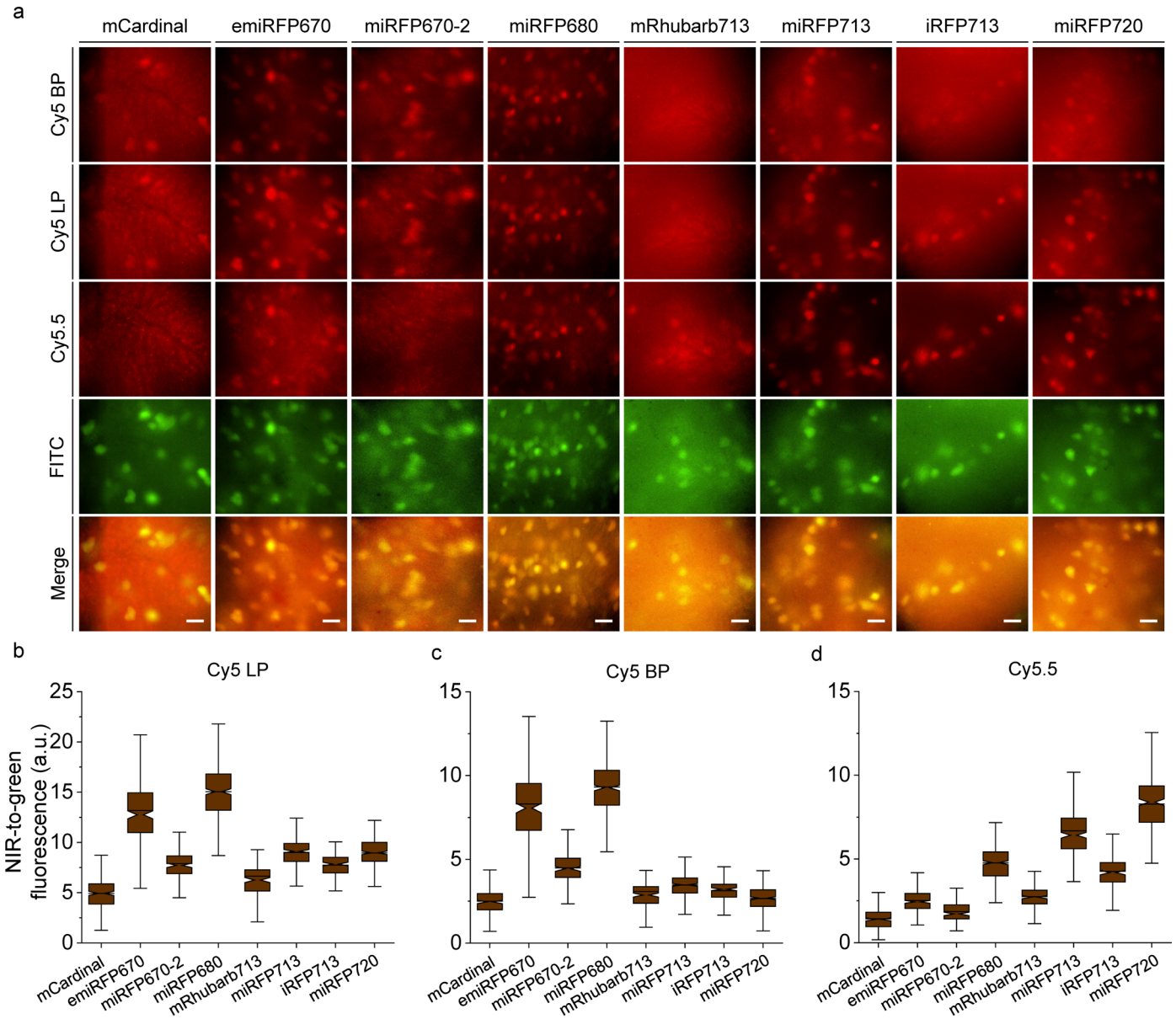

Extended Data Fig. 7 | Quantitative characterization of the selected NIR FPs expressed in mouse liver in vivo. ((**a**) Representative wide-field fluorescence images of NIR FPs expressed in mouse liver acquired in Cy5-LP, Cy5-BP, Cy5.5, and FITC channels (excitation power 55 mW/mm^2 for Cy5 and Cy5.5 channels; $n = 3$ liver slices from 3-4 mice for each protein). (**b**,**c**,**d**) Intracellular normalized brightness of NIR FPs imaged in fresh liver tissue from three-month-old mice in (**b**) Cy5-LP, (**c**) Cy5-BP, (**d**) Cy5.5 channels (excitation power 55 mW/mm^2; n > 154 cells from 3-4 mice for each protein in each channel). Brightness for each FP was normalized to the EGFP signal. See Supplementary Dataset 1 for the detailed descriptive statistics and exact p-values.

https://doi.org/10.1038/s41592-023-01975-z

Extended Data Table 1 | List of the NIR FPs selected for quantitative assessment in cultured cells[56–59]

Protein	Excitation maximum (nm)	Emission maximum (nm)	Extinction coefficient ($M^{-1}cm^{-1}$)	Quantum yield	Molecular brightness	Ref.
mNeptune2.5	599	643	95,000	0.24	22.8	4
mCardinal	604	659	87,000	0.19	16.53	4
E2-Crimson	611	646	126,000	0.23	28.98	59
smURFP	642	670	180,000	0.18	32.4	60
BDFP1.6	642	666	100,000	0.197	19.7	61
emiRFP670	642	670	87,400	0.14	12.24	62
miRFP670-2	643	670	103,000	0.136	14.01	62
iRFP670	643	670	114,000	0.11	12.54	5
miRFP680	661	680	94,000	0.145	13.63	62
iRFP682	663	682	90,000	0.11	9.9	5
emiRFP703	674	703	90,900	0.086	7.82	62
BDFP1.8	678	702	77,027	0.061	4.7	24
miRFP2	676	706	55,600	0.043	2.39	6
mIFP	683	704	82,000	0.08	6.56	18
IFP2.0	690	711	86,000	0.08	6.88	63
mRhubard713	690	713	113,457	0.0763	8.66	64
miRFP713	690	713	99,000	0.07	6.93	62
iRFP713	690	713	105,000	0.06	6.3	3
SNIFP	697	720	149,200	0.022	3.28	11
mRhubarb719	700	719	83,769	0.068	5.7	64
mRhubarb720	701	720	94,941	0.0646	6.13	64
miRFP720	702	720	98,000	0.061	5.98	9

https://doi.org/10.1038/s41592-023-01975-z

Extended Data Table 2 | Spectroscopic and biochemical properties of the selected NIR FPs measured in this study

Protein	Abs (nm)	Em (nm)	ε_{max} ($mM^{-1}\cdot cm^{-1}$)[a]	ε_{max} ($mM^{-1}\cdot cm^{-1}$)[b]	φ	τ (ns)	$\tau_R = \tau/\varphi$ (ns)	$S_0 \rightarrow S_n$ σ_2 (GM) (λ, nm)	$S_0 \rightarrow S_1$ σ_2 (GM) (λ, nm)	pK_a
mCardinal	603	645 [659[d]]	79[c] [87[d]]	75.4	0.21 [0.19[d]]	1.38 [1.3[e]]	6.6	88 (800 nm)	48 (1200 nm)	5.4 [5.3[d]]
emiRFP670	385,643	667 [670[f]]	81 [87.4[f]]	46	0.16 [0.14[f]]	1.53	9.6	200 (832 nm) 132 (880 nm)	17 (1196 nm)	3.4, 10.3 [4.5[f]]
miRFP670-2	387,645	669 [670[f]]	82 [103[f]]	49	0.16 [0.136[f]]	1.42	8.9	188 (832 nm) 109 (880 nm)	18 (1196 nm)	3.7 [4.5[f]]
miRFP680	381,663	677 [680[f]]	88 [94.0[f]]	48	0.16 [0.145[f]]	1.67	10.4	158 (860 nm) 116 (890 nm)	23 (1220 nm)	3.9 [4.5[f]]
mRhubarb713	389,690	710 [713[g]]	77 [113.5[g]]	53	0.069 [0.0763[g]]	0.78	11.3	142 (890 nm)	22 (1280 nm)	4.2
miRFP713	391,690	709 [713[f]]	93 [99.0[f]]	52	0.079 [0.07[f]]	0.89	11.3	154 (890 nm)	25 (1284 nm)	4.3, 10.9 [3.5[f]]
iRFP713	390,690	710 [713[h]]	92 [98.0[h]]	56	0.073 [0.063[h]]	0.78 [0.63[e]]	10.7	113 (890 nm) [446 (890 nm)[i]]	19 (1276 nm) [74 (1280 nm)[i]]	4.3 [4.5[h]]
miRFP720	393,703	718 [720[j]]	95 [98.0[j]]	52	0.064 [0.061[j]]	0.81	12.7	166 (888 nm) 132 (900 nm)	26 (1300 nm)	4.3, 10.7 [4.5[j]]

ε_{max}, extinction coefficient; φ, quantum yield; τ, fluorescence lifetime; σ_2, two-photon cross-section; λ, wavelength. [a]Calculated based on the Soret band peak; [b]Calculated based on the Strickler–Berg equation. [c]Measured using alkaline denaturation. [d]Data from ref. 4. [e]Data from ref. 46. [f]Data from ref. 13. [g]Data from ref. 60. [h]Data from ref. 10. [i]Data from ref. 16. [j]Data from ref. 9.

nature research

Corresponding author(s): Kiryl D. Piatkevich

Last updated by author(s): May 31, 2023

Reporting Summary

Nature Research wishes to improve the reproducibility of the work that we publish. This form provides structure for consistency and transparency in reporting. For further information on Nature Research policies, see our Editorial Policies and the Editorial Policy Checklist.

Statistics

For all statistical analyses, confirm that the following items are present in the figure legend, table legend, main text, or Methods section.

n/a	Confirmed	
☐	☒	The exact sample size (*n*) for each experimental group/condition, given as a discrete number and unit of measurement
☐	☒	A statement on whether measurements were taken from distinct samples or whether the same sample was measured repeatedly
☐	☒	The statistical test(s) used AND whether they are one- or two-sided *Only common tests should be described solely by name; describe more complex techniques in the Methods section.*
☐	☒	A description of all covariates tested
☐	☒	A description of any assumptions or corrections, such as tests of normality and adjustment for multiple comparisons
☐	☒	A full description of the statistical parameters including central tendency (e.g. means) or other basic estimates (e.g. regression coefficient) AND variation (e.g. standard deviation) or associated estimates of uncertainty (e.g. confidence intervals)
☐	☒	For null hypothesis testing, the test statistic (e.g. *F*, *t*, *r*) with confidence intervals, effect sizes, degrees of freedom and *P* value noted *Give P values as exact values whenever suitable.*
☒	☐	For Bayesian analysis, information on the choice of priors and Markov chain Monte Carlo settings
☒	☐	For hierarchical and complex designs, identification of the appropriate level for tests and full reporting of outcomes
☐	☒	Estimates of effect sizes (e.g. Cohen's *d*, Pearson's *r*), indicating how they were calculated

Our web collection on statistics for biologists contains articles on many of the points above.

Software and code

Policy information about availability of computer code

Data collection	Data was collected using NIS-Elements Advance Research software (version 5.21.00), Leica Application Suite X Office v3.5.5, Olympus FV3000-IX83, ZEN blue v3.5, ZEN black v2.3, CytExpert v2.4, Amersham Imager 680. Data collection for fluorescence spectra of NIR FPs were done using https://www.fpbase.org.
Data analysis	Data was analyzed offline using NIS-Elements Advance Research software (version 5.21.00 and 5.30.00), Excel (Microsoft), OriginPro (2019b, OriginLab), GraphPad Prism v8, Fiji 2.9.01/1.53t ImageJ, the Microscope online application (https://www.fpbase.org/microscope), CytExpert v2.4, Amersham Imager 680 analysis software.

For manuscripts utilizing custom algorithms or software that are central to the research but not yet described in published literature, software must be made available to editors and reviewers. We strongly encourage code deposition in a community repository (e.g. GitHub). See the Nature Research guidelines for submitting code & software for further information.

Data

Policy information about availability of data

All manuscripts must include a data availability statement. This statement should provide the following information, where applicable:

- Accession codes, unique identifiers, or web links for publicly available datasets
- A list of figures that have associated raw data
- A description of any restrictions on data availability

The mass spectrometry proteomics data generated in this study have been deposited to the iProX database with the dataset identifier IPX0005767000. The total size of the files acquired for this study was about 2 TB, which exceeds the limit of the fileshare repository, therefore only the most essential raw datasets including raw images supporting results in Fig. 1-5, Extended Data Fig. 1-7, Supplementary Fig. 2, 3, 5, 7, 9, 11 are available at FigShare [https://figshare.com/authors/

Hanbin_Zhang/14524646]. The rest of the files are available from the corresponding author upon request. Source data files are provided with this paper. All plasmids used in this study are available from Addgene and WeKwikGene (https://wekwikgene.wllsb.edu.cn/).

Field-specific reporting

Please select the one below that is the best fit for your research. If you are not sure, read the appropriate sections before making your selection.

☒ Life sciences ☐ Behavioural & social sciences ☐ Ecological, evolutionary & environmental sciences

For a reference copy of the document with all sections, see nature.com/documents/nr-reporting-summary-flat.pdf

Life sciences study design

All studies must disclose on these points even when the disclosure is negative.

Sample size	For cell culture experiments we performed power based on the pilot data reported in the Stage 1 manuscript to identify the lowest number of cells needed for the experiments. For in vivo experiments we did not perform a power analysis because prior information on mean and standard deviation of brightness for tested NIR FPs in neurons in model organism is lacking, as noted in Dell at al., Sample Size Determination, 2003: "It is not possible to compute a sample size for certain types of experiments because prior information is lacking or because the success of the experiment is highly variable, such as in producing a transgenic animal" (for C. elegans and zebrafish in vivo experiments we produced transgenic animals). Therefore the sample size for in vivo experiments was based on our past experience in characterizing neurotechnologies. The suggested number of samples for in vivo assessment was approved during Stage 1 of the manuscript preparation. Full statistical analysis for the performed experiments are summarized in Supplementary Table 1, 2 and Supplementary Dataset 1.
Data exclusions	P7. Several NIR FPs (smURFP, miRFP2, mIFP, IFP2, mRhubarb719, and mRhubarb720) were either too dim or did not form classical whorl structures and thus were excluded from further assessment. P22. According to Cranfill et al. recommendations, positive cells selected for analysis will have overall similar fluorescence brightness, and cells that are significantly brighter will be excluded (indications of unhealthy or highly stressed cells). Cells with non-spherical nuclei, ER sheet architectures, or condensed nuclei will be excluded from the assay. P18. The data were excluded from the analysis if cells died after transfection or cell culture was contaminated with bacteria or yeast. P18 and P19. Cells that detached or died during photobleaching experiments were excluded from data analysis. P26. Animals that show no GFP fluorescence were excluded from the study, the exclusion criterion was pre-established. P28. The data were excluded from the analysis if zebrafish moved during image recording.
Replication	All attempts at replication were successful. For live HEK imaging, all experiments were performed independently three times except for photostability experiments, which were reproduced four times independently. For fixed HEK cells, all experiments were reproduced twice independently, except for the ExM measurements, which were performed only once. For OSER assay, all experiments performed twice independently. For fusion imaging in HeLa cells including multicolor imaging, the experiments were performed once with three replicates for each tested fusion. For live neuronal culture imaging, all experiments were reproduced twice independently with 20 replicates for each experiment. rAAV injections for brain tissue in mice were performed once with 5-7 replicates for each protein. AAV injections for liver tissue in mice were performed once with 3-4 replicates for each protein. C. elegans experiments were performed once with 30 replicates for each protein. Zebrafish experiments were performed once with 4 replicates for each protein, except for multicolor imaging in zebrafish, which was performed once with 10 replicates.
Randomization	All cell culture experiments were performed in random order. AAV injections, animal dissections, and tissue imaging were preformed in random order.
Blinding	The researchers were blinded to the sample identities during data collection and analysis

Reporting for specific materials, systems and methods

We require information from authors about some types of materials, experimental systems and methods used in many studies. Here, indicate whether each material, system or method listed is relevant to your study. If you are not sure if a list item applies to your research, read the appropriate section before selecting a response.

Materials & experimental systems

n/a	Involved in the study
☐	☒ Antibodies
☐	☒ Eukaryotic cell lines
☒	☐ Palaeontology and archaeology
☐	☒ Animals and other organisms
☒	☐ Human research participants
☒	☐ Clinical data
☒	☐ Dual use research of concern

Methods

n/a	Involved in the study
☒	☐ ChIP-seq
☐	☒ Flow cytometry
☒	☐ MRI-based neuroimaging

Antibodies

Antibodies used	Primary antibodies: rabbit anti-GFP (clone D5.1, dilution 1:1000, 2956T, Cell Signaling Technology, USA), mouse anti-P2A (clone 3H4, dilution 1:1000, NBP2-59627SS, Novus Biologicals, USA).
Validation	All antibodies in the study were used according to the user manuals and validation statements can be found on the respective manufacture website (https://www.cellsignal.com/products/primary-antibodies/gfp-d5-1-rabbit-mab/2956 and https://www.novusbio.com/products/2a-peptide-antibody-3h4_nbp2-59627). In the current study the antibodies performed as expected (Supplementary Figure 5).

Eukaryotic cell lines

Policy information about cell lines

Cell line source(s)	HEK293FT (Invitrogen) and HeLa (ATCC CCL-2)
Authentication	Cells were authenticated by the manufacturer using STR profiling, and reauthenticated in our lab by inspecting stereotypical morphological features under widefield microscope and tested negative for mycoplasma contamination to their standard levels of stringency and were here used because they are common cell lines for testing new tools.
Mycoplasma contamination	Cells were authenticated by and tested negative for mycoplasma contamination using KIT NAME VENDOR NUMBER to their standard levels of stringency and were here used because they are common cell lines for testing new tools.
Commonly misidentified lines (See ICLAC register)	No commonly misidentified lines were used in the study.

Animals and other organisms

Policy information about studies involving animals; ARRIVE guidelines recommended for reporting animal research

Laboratory animals	For neuronal culture, about 25 P0 pubs were sacrificed to get the dissociated neurons regardless of gender. For brain slice imaging, at least 15 pubs from two mother mice were injected with AAVs at P0 for each protein regardless of gender. For the brightness obtained from live brain slice, total 9 mice were sacrificed for each protein at P20-30, 2 months and 3 months (3 mice at each time point). For the photostability obtained from live brain slice, 3 mice were sacrificed for each protein at P20-30. For the brightness and photostability obtained from fixed brain slice, 2 mice were sacrificed for each protein at P20-30. For the brightness obtained from live liver slice, 3 three-month-old male mice were sacrificed for each protein. 3-4 three-month-old male mice were injected with AAVs through tail vein injection for each protein. All the mice in the experiment were C57BL/6J. Mice were maintained at strict barrier facilities with macroenvironmental temperature and humidity ranges of 20-26 °C and 40-70%, respectively. Food and water were provided ad libitum. The rooms had a 12 h light/12 h dark cycle. The housing conditions were closely monitored and controlled. The pigmentation-compromised zebrafish brass strain and homozygous nacre embryos of the pan-neuronal expressing Gal4 line (tg(elavl3:GAL4-VP16)nns6) at 33 hours post fertilization and 4-5 days post fertilization regardless of sex, since sex cannot be specified at these stages, were used for proteins expression in zebrafish. Transgenic [tag-168::wNIR-FPs-T2A-HO1, tag-168::wmNeonGreen] C. elegans worms on wild-type N2 background were used at the L4 developmental stage disregarding sex.
Wild animals	No wild animals were used in the study
Field-collected samples	No field-collected samples were used in the study
Ethics oversight	All animal maintenance and experimental procedures for mice were conducted according to the Westlake University Animal care guidelines, and all animal studies were approved by the Institutional Animal Care and Use Committee (IACUC) of Westlake University, Hangzhou, China under animal protocol #19-044-KP. All experiments involving zebrafish at Technische Universität Braunschweig were conducted in accordance with protocols approved by German legislation following European Union guidelines (EU Directive 2010_63).

Note that full information on the approval of the study protocol must also be provided in the manuscript.

Flow Cytometry

Plots

Confirm that:

☒ The axis labels state the marker and fluorochrome used (e.g. CD4-FITC).

☒ The axis scales are clearly visible. Include numbers along axes only for bottom left plot of group (a 'group' is an analysis of identical markers).

☒ All plots are contour plots with outliers or pseudocolor plots.

☒ A numerical value for number of cells or percentage (with statistics) is provided.

Methodology

Sample preparation	To perform cytotoxicity assay of the NIR FPs, HEK293FT (Invitrogen) cells were transiently transfected with pAAV-CAG-NIR-FPs plasmids and dummy DNA (pUC19) as negative control using Hieff Trans Liposomal Transfection Reagent (40802ES02, Yeasen Biotechnology, China) and assessed at 36-48 h post transfection using Annexin V, Alexa Fluor™ 568 conjugate (A13202, ThermoFisher, USA) and Live/Dead reagent (L34958, Viability/Vitality Kit, ThermoFisher) according to the manufacture protocol with minor changes. Annexin V conjugates are designed to detect the externalization of phosphatidylserine, one of the earliest indicators of apoptosis. Briefly, we prepared annexin-binding buffer: 10 mM HEPES, 140 mM NaCl, and 2.5 mM CaCl2, pH 7.4, and added dyes indicating live and dead into the buffer making the dyes at working concentration. The HEK cells were harvested at a concentration of 1x106 cells/mL in each 1.5 ml tube using EDTA-free Trypsin (BL527A, Biosharp) and washed in cold phosphate-buffered saline (PBS). The washed cells were recentrifuged and removed the supernatants. One tube of the untransfected cell pellets was heated at 50℃ for 10 minutes to obtain the heat-killed cells as positive control for apoptotic cells and dead cells. The HEK cells including heat-killed cells were resuspended in 100 ul annexin-binding buffer containing Live/Dead reagent. After incubating the cells on ice for 15 minutes, 5 µl of the annexin V conjugate were added into each 100 µl of cell suspension. Then incubated the cells at room temperature for 15 minutes. After the incubation period, added 400 µl of annexin-binding buffer without Live/Dead reagent, mixed gently, then kept the samples on ice. As soon as possible, the stained cells were analyzed using a flow cytometer (CytoFLEX LX, Beckman Coulter) equipped with a 405 nm laser and 450/45 bandpass for calcein violet–labeled live cells (Live V450-PB-A) and 525/40 bandpass for the aqua-fluorescent reactive dye-labeled dead cells (Dead V525-KrO-A); a 561 nm laser and 585/42 bandpass (Apoptosis Y585-PE-A) for Annexin V-labeled live cells. The channels of Cy5-BP R660-APC-A and Cy5-LP R712-APCA700-A with a 638 nm laser of the flow cytometer were used to analyze the NIR-FPs positive cells. The cytotoxicity was quantified as fraction of dead cells and cells in early stage of apoptosis from the total transfected cells. Since the signal of NIR FPs exhibited crosstalk into the channels used for detection of dyes signals, their signals were compensated correspondingly.
Instrument	CytoFLEX LX flow cytometer, Beckman Coulter
Software	CytExpert v2.4 software was used data collection and analysis
Cell population abundance	No cell collection was performed, only cell population analysis, see Supplementary Table 5 for abundance of relevant cell populations.
Gating strategy	First, cells were gated out using forward and side scatter area (FCS-A and SSC-A), and then cell aggregates were gated out using forward scatter area and height (FSC-A, FSC-H) before desired fluorescence channels were used to analyze cells (lower left FACS dot-plot). See Supplementary Figure 7 for plots reflecting gating strategy.

☒ Tick this box to confirm that a figure exemplifying the gating strategy is provided in the Supplementary Information.

nature methods

Registered Report

https://doi.org/10.1038/s41592-023-01975-z

Quantitative assessment of near-infrared fluorescent proteins

In the format provided by the authors and unedited

Supplementary Note 1.

According to the FPbase.org, there are more than 60 FPs with NIR fluorescence (emission peak ≥640 nm) reported to date (as of December 2021). We decided to select top-performing NIR FPs for this study. The major selection criterion was theoretical brightness in Cy5-LP and Cy5.5 channels (as described in the Methods section) calculated based on the fluorescence spectra and molecular brightness of FPs. To perform the brightness analysis, we used the Microscope function on the FPbase.org website. We created corresponding optical configurations and ran Fluorophore Efficiency Report for all available in the database basic FPs (we provided the report in the form of source data with all used parameters and calculated efficiencies, see Source Data file **for Extended Data Table 1**). The created optical configurations are available at the following link Wide-field NIR-FPs (https://www.fpbase.org/microscope/AGNs5RmoK5TeQyhTCdQ6bJ/?c=NIR-637-LP&l=spectra-iii-cy5&d=hamamatsu-orca-flash40-v3) at the FPbase.org. We set up the cut-off for selection as an order of magnitude difference compared to the top variants in Cy5-LP and Cy5.5 channels (see NIR-FPs KP collection at https://www.fpbase.org/collection/1301/). According to the used selection criteria NIR FPs that are dimmer than mCardinal in Cy5-LP and Cy5.5 channels were not selected. We further refined the list based on the literature data reporting performance of the qualified NIR FPs in mammalian cells and *in vivo*. For example, the miRFP670nano was above the cut-off line but it was excluded due to the low performance in HEK cells as it was 10-fold dimmer than mCardinal in HEK cells in our hands reported in the previous study[1]. We also excluded IFP1.4, iRFP703, and iRFP720 as they demonstrated lower performance in cultured cells including neurons compared to other dimeric NIR FPs, such as iRFP670, iRFP682, and iRFP713 (*refs.*[2,3]). We also excluded TDsmURFP as it is a tandem version of smURFP. We added recently reported enhanced monomeric miRFPs (emiRFP670, miRFP670-2, emiRFP703, and miRFP2), which were not included in the analysis due to missing spectral data in the FPbase.org database but reported to have improved brightness in mammalian cells[4,5]. As a final result, we selected 22 NIR FPs listed in **Extended Data Table 1** for quantitative assessment in cultured mammalian cells.

Supplementary Note 2.

Since the expression level can vary a lot from plasmid to plasmid as well as from cell to cell even within the same transfection it is very important to establish an expression system that can normalize such variations. The co-expression of a reference FP is the most straightforward approach for expression-level normalization. There are several ways to co-express two genes using bicistronic systems, such as internal ribosome entry site (IRES), self-cleaving peptides, *e.g.*, P2A, and direct fusion of two FPs via an amino acid linker. The optimal expression system would provide: i) high co-expression correlation; ii) high reproducibility between independent transfection; iii) minimal variability of fluorescence ratios for individual cells within one transfection. To select the optimal co-expression system, we assembled four constructs, namely, miRFP680-P2A-EGFP, miRFP680-IRES2-EGFP, miRFP680-Linker-EGFP, and miRFP680-Linker-EGFP-P2A-FusionRed, which were cloned into the same expression vector under the CAG promoter. We carried out two independent transfections for each plasmid and assessed fluorescence intensity according to the intracellular brightness measurements protocol described in the Methods section. We compared absolute fluorescence intensity, fluorescence intensity correlation between two channels, and variability and reproducibility of fluorescence ratios (**Supplementary Figure 1**). Based on the quantitative analysis the miRFP680-P2A-EGFP construct demonstrated the highest performance among tested plasmids and, most importantly, it showed high reproducibility between independent transfections and minimal variability of fluorescence ratios (range of the miRFP680-to-EGFP fluorescence ratios for miRFP680-P2A-EGFP was 0.27-2.5, for miRFP680-IRES2-EGFP was 1.5-27, for miRFP680-Linker-EGFP was 0.17-3.0, for miRFP680-Linker-EGFP-P2A-FusionRed was 0.5-5.3, and range of the miRFP680-to-FusionRed fluorescence ratios was 0.18-25). The miRFP680-P2A-EGFP plasmid was the only construct to show no statistically significant difference between two independent transfections despite of almost 2-fold difference in the mean of fluorescence intensity, while other constructs showed a statistically significant difference between two independent transfections despite the matching level of fluorescence intensity. We should also note that the constructs containing fusion of miRFP680 with EGFP via amino acid linker exhibited significant aggregation in HEK cells which makes these constructs suboptimal for the intracellular brightness quantification. Therefore, we selected the NIR-FP-P2A-EGFP construct for the proposed experiments, and will be used for intracellular brightness assessment of all selected NIR FPs. We also think that P2A has another advantage like small size allowing to pack more genes into AAVs. We hope the plasmids generated in the course of this work will be used by others since P2A is widely adopted and well-validated.

Supplementary Table 1. Statistics on expression cassette performance comparison for vector selection in HEK293 cells.

Descriptive Statistics on raw data for outlier determination.

	P2A		IRES2		Linker		Linker-P2A	
Transf	**1**	**2**	**1**	**2**	**1**	**2**	**1**	**2**
N total	1536	1997	2357	1932	2287	2622	1043	806
Mean	1.43032	1.14317	18.97242	17.04187	1.53422	1.40054	2.61548	2.38888
SD	1.48412	0.68081	197.89486	140.52814	1.04619	0.95032	1.53127	1.32561
SE	0.03787	0.01523	4.07619	3.19713	0.02188	0.01856	0.04741	0.04669
Var.	2.20262	0.46351	39162.37379	19748.15822	1.09452	0.9031	2.34478	1.75725
Q1	0.72823	0.73694	6.74484	6.29574	0.96041	0.87435	1.59872	1.45746
Median	0.96034	0.96531	9.82828	9.04427	1.31212	1.20134	2.13556	1.96598
Q3	1.47355	1.31057	14.71206	14.36979	1.79859	1.60428	3.10526	2.92625
IQR	0.74532	0.57362	7.96721	8.07405	0.83818	0.72993	1.50654	1.46879

All outliers were determined by calculating 1.5*IQR and Ratios>1.5*IQR were discarded.

Descriptive statistics of analyzed data.

	P2A		IRES2		Linker		Linker-P2A	
Transf	**1**	**2**	**1**	**2**	**1**	**2**	**1**	**2**
N total	1374	1878	2169	1789	2153	2358	885	724
Mean	1.0337	1.01356	10.35834	9.89473	1.36281	1.16695	2.31222	2.13342
SD	0.47511	0.38762	5.1682	5.20988	0.57164	0.44155	1.02142	0.98285
SE	0.01282	0.00894	0.11097	0.12317	0.01232	0.00909	0.03433	0.03653
Var.	0.22573	0.15025	26.71034	27.14284	0.32677	0.19497	1.0433	0.966
Q1	0.70634	0.72095	6.43309	6.08956	0.94223	0.84418	1.55623	1.4324
Median	0.91208	0.93218	9.23451	8.61247	1.26684	1.13524	2.03347	1.83546
Q3	1.23204	1.23593	13.22465	12.62524	1.68227	1.43156	2.81007	2.66748
IQR	0.5257	0.51498	6.79156	6.53568	0.74004	0.58738	1.25384	1.23508

Pearson's correlation between infrared and green fluorescence for P2A, IRES2, Linker and Linker-P2A.

	N total	R	p-value
P2A	3252	0.4422	8.83377e-156
IRES2	3958	0.33787	2.79326e-106
Linker	4511	0.23922	9.92599e-60
Linker-P2A (CY5-LP with GFP)	1609	0.73764	2.08564E-276
Linker-P2A (CY5-LP with RFP)	1609	0.51051	1.68411E-107

Shapiro-Wilk normality test on distribution of ratios for P2A, IRES2, Linker, Liker-P2A.

	Transfection	DF	Statistic	p-value	Decision (α=0.05)
P2A	1	1374	0.8971	0	Reject normality
	2	1878	0.94636	0	Reject normality
IRES2	1	2169	0.93754	0	Reject normality
	2	1789	0.92938	0	Reject normality
Linker	1	2153	0.95555	0	Reject normality
	2	2358	0.9807	0	Reject normality
Linker-P2A (Cy5-LP with GFP)	1	885	0.9103	0	Reject normality
	2	724	0.905	0	Reject normality
Linker-P2A (Cy5-LP with GFP)	1	885	0.8642	0	Reject normality
	2	724	0.95402	2.9754E-14	Reject normality

Kolmogorov-Smirnov pairwise comparison between biological replicates of P2A, IRES2, Linker, Linker-P2A.

	D	Z	p-value
P2A	0.04591	1.29315	0.06645

	D	Z	p-value
IRES2	0.0614	1.92241	0.00114

	D	Z	p-value
Linker	0.14519	4.8708	4.04404E-21

	D	Z	p-value
Linker-P2A (CY5-LP with GFP)	0.10766	2.14835	1.69504E-4

	D	Z	p-value
Linker-P2A (CY5-LP with RFP)	0.65021	12.97529	4.87479E-147

Power and Sample Size

Descriptive Statistics on expression of 5 proteins in HEK cells under Cy5-LP; 3 independent transfections

	mNeptune2.5	iRFP670	miRFP680	mRhubarb720	miRFP720
N total	146	6322	5545	3388	4088
Mean	4.52132	10.51965	6.0095	0.20929	2.67664
SD	4.38497	10.76024	5.33823	0.13926	1.74865
SE	0.3629	0.13533	0.07169	0.00239	0.02735
Var.	19.22792	115.7828	28.4967	0.01939	3.05778
Q1	1.78149	1.66833	2.55726	0.11192	1.25887
Median	2.73673	6.27865	4.17333	0.17071	1.83404
Q3	5.34493	17.54405	7.41001	0.26655	3.99887
IQR	3.56344	15.87572	4.85275	0.15463	2.74

	N total	Mean	SD	Sum	CSS	Minimum	Median	Maximum
Mean	5	4.78728	3.86773	23.93639	59.83737	0.20929	4.52132	10.51965

PSS One-way ANOVA

Alpha	Sample Size	Power
0.05	20	1
0.05	30	1
0.05	40	1
0.05	50	1
0.05	100	1
0.05	200	1

Supplementary Table 2. Descriptive statistics for cell culture experiments.
Sample Size

Protein	Live HEK cells								Fixed HEK cells				
	Brightness						Photostability		Brightness			Photostability	
	Cy5-LP	After BV	Cy5-BP	After BV	Cy5.5	After BV	Cy5-LP	Cy5.5	Cy5-LP	Cy5-BP	Cy5.5	Cy5-LP	Cy5.5
mNeptune2.5	1945	2204	1945	2204	1705	1824	99	ND	3540	3540	2312	40	40
mCardinal	4841	4236	4841	4236	4841	4235	100	88	3670	3670	3343	40	40
E2-Crimson	3562	2097	3562	2097	3562	2097	94	83	3494	3494	3491	40	40
smURFP	5930	4950	6163	6165	6163	6165	100	101	5642	5642	5642	40	40
BDFP1.6	6230	4751	6230	4751	6230	4751	113	96	3511	3511	3511	40	40
emiRFP670	6658	4531	6658	4531	6658	4531	117	100	2610	2610	2610	40	40
miRFP670-2	6035	5374	6035	5374	6035	5374	111	88	3437	3437	3437	40	40
iRFP670	8911	6383	8911	6383	8911	6383	110	96	4554	4554	4554	40	40
miRFP680	4770	4723	4770	4723	4770	4723	98	88	2372	2372	2372	40	40
iRFP682	5118	5273	5118	5273	5118	5273	113	104	4525	4525	4525	40	40
emiRFP703	3325	2463	3326	2463	3326	2463	98	93	4328	4328	4328	40	40
BDFP1.8	5970	2346	5970	2346	5970	2346	98	90	4596	4596	4596	40	40
miRFP2	4417	2871	4417	2871	4417	2871	110	104	1974	1976	1976	40	40
mIFP	5439	4380	5439	4380	5439	4380	101	100	5483	5483	5483	40	40
IFP2	6060	5200	6060	5200	6060	5200	110	105	3291	3291	3291	40	40
mRhubarb713	4831	3477	4831	3477	4831	3477	97	95	5539	5539	5539	40	40

miRFP713	4819	2039	4819	2039	4819	2039	103	101	2364	2364	2364	40	40
iRFP713	5771	4865	5771	4865	5771	4865	96	104	3297	3297	3297	40	40
SNIFP	5965	6555	5965	6555	5965	6555	110	110	4958	4958	4958	40	40
mRhubarb719	6192	6019	5754	5833	6203	6019	107	102	2997	2921	3005	40	40
mRhubarb720	4619	4823	4425	4753	4620	4823	114	93	2351	2340	2351	40	40
miRFP720	4116	4429	4116	4429	4116	4429	108	97	2309	2309	2309	40	40

From 3 independent transfections for brightness, 4 for photostability for each protein for live cells, and 2 independent transfections for fixed cells.

Supplementary Table 3. Intracellular brightness and photostability of NIR FPs in live HEK cells.

Protein	Relative brightness vs mCardinal in Cy5-LP (%)[a,b]						Photostability (s)[a,b]	
	Cy5-LP		Cy5-BP		Cy5.5		Cy5	Cy5.5
	No BV[c]	BV (fold)[d]	No BV[c]	BV (fold)[d]	No BV[c]	BV (fold)[d]		
mNeptune2.5	31.8	1.2	20.5	1.2	0.15[e]	2.0	477 ± 11	ND
mCardinal	100	1.1	66.9	1.0	0.21[e]	1.0	338 ± 5	NA
E2-Crimson	69.7	1.0	46.8	0.9	0.15[e]	1.0	155 ± 3	NA
smURFP	16.5	1.7	12.8	2.3	0.43[e]	3.3	425 ± 22	NA
BDFP1.6	27.1	2.5	19.3	2.5	1.39[e]	2.6	427 ± 7	NA
emiRFP670	44.2	1.9	29.5	1.9	3.96[e]	1.8	490 ± 11	NA
miRFP670-2	52.1	1.9	35.2	1.9	3.27[e]	1.8	246 ± 4	NA
iRFP670	44.2	1.9	29.8	1.8	3.06[e]	1.8	271 ± 3	NA
miRFP680	60.5	1.7	39.9	1.7	12.80	1.7	1277 ± 23	2312 ± 27
iRFP682	32.6	1.8	20.8	1.7	8.82	1.7	800 ± 29	1219 ± 21
emiRFP703	43.7	1.6	16.0[e]	1.6	34.28	1.6	571 ± 12	723 ± 9
BDFP1.8	11.3	2.9	5.1	2.9	8.36	2.9	2864 ± 65	1765 ± 41
miRFP2	27.0	1.9	10.1	1.9	21.2	1.9	817 ± 21	898 ± 12
mIFP	18.9	1.7	6.4[e]	1.7	16.1	1.9	251 ± 8	215 ± 4
IFP2	21.4	2.1	5.0[e]	2.0	29.47	2.2	188 ± 4	81 ± 1
mRhubard713	9.2[e]	2.0	1.9[e]	1.9	13.17	2.1	3409 ± 45	2059 ± 19
miRFP713	17.9	2.2	3.7[e]	2.2	26.0	2.3	3291 ± 49	1400 ± 22
iRFP713	21.3	1.7	4.2[e]	1.7	30.84	1.7	2169 ± 64	1388 ± 25
SNIFP	23.9	1.6	3.7[e]	1.6	36.97	1.5	507 ± 6	309 ± 2
mRhubarb719	1.4[e]	2.1	0.3[e]	1.4	1.82[e]	2.3	1587 ± 28	NA
mRhubarb720	2.5[e]	2.1	0.5[e]	1.8	3.49	2.2	1034 ± 24	913 ± 15
miRFP720	13.2	1.7	1.4[e]	1.6	21.31	1.7	1344 ± 16	1114 ± 11

[a]56-58 mW/mm^2 illumination power;
[b]performed in live HEK cells imaged 36-48 h post transfection, 3 independent transfections each (4 for photostability measurements);
[c]relative to intracellular brightness of mCardinal in Cy5-LP channel;
[d]represented as a fold increase of fluorescence upon administration of 25 μM relative to no BV value on the left;
[e]signal-to-background ≤ 2.0.
ND – not determined;
NA – not applicable.

Supplementary Table 4. Intracellular brightness and photostability of NIR FPs in live primary cultured mouse neurons.

Protein	Relative brightness vs emiRFP670 in Cy5-LP (%)						Photostability (s)[a]	
	Cy5-LP		Cy5-BP		Cy5.5		Cy5	Cy5.5
	No BV[b]	BV (fold)[c]	No BV[b]	BV (fold)[c]	No BV[b]	BV (fold)[c]		
mNeptune2.5	4.8	1.2	3.4	1.2	0.1	4.1	600 ± 10	ND
mCardinal	12.6	1.2	9.9	1.1	0.3	1.6	471± 5	ND
E2-Crimson	21.3	1.0	15.3	1.0	0.2	1.0	146± 5	ND
smURFP	5.0	21.7	4.0	20.4	0.4	12.0	359 ± 8	ND
BDFP1.6	17.0	8.6	13.0	8.5	0.7	12.7	716 ± 9	ND
emiRFP670	100	1.7	69.9	1.7	7.7	1.6	699 ± 30	ND
miRFP670-2	66.4	2.0	46.2	2.0	4.5	2.1	350 ± 7	ND
iRFP670	50.9	2.5	36.4	2.6	3.3	2.9	362 ± 7	ND
miRFP680	72.9	2.4	49.0	2.4	16.6	2.5	1496 ± 18	2528 ± 44
iRFP682	17.9	4.3	11.4	4.7	5.4	5.5	1057 ± 19	1244 ± 26
emiRFP703	35.3	1.9	13.2	1.8	31.9	1.8	888 ± 10	963 ± 15
BDFP1.8	6.9	4.7	3.4	4.3	4.9	4.6	2102 ± 42	1905 ± 36
miRFP2	3.0	2.6	1.5	2.1	2.0	3.1	888 ± 19	1153 ± 26
mIFP	9.7	4.2	3.0	5.0	10.6	4.0	492 ± 5	387 ± 8
IFP2	7.6	5.0	1.7	4.6	12.4	4.6	222 ± 9	119 ± 5
mRhubard713	17.5	4.6	3.6	4.7	24.9	4.6	3991 ± 48	2134 ± 23
miRFP713	63.7	1.6	13.3	1.6	88.5	1.6	3123 ± 54	1986 ± 21
iRFP713	36.3	2.9	6.4	3.3	55.8	2.8	2429 ± 33	1975 ± 64
SNIFP	21.5	1.9	3.8	1.8	31.5	1.9	639 ± 6	519 ± 6
mRhubarb719	2.9	7.7	0.8	4.6	3.4	8.9	2067 ± 21	ND
mRhubarb720	6.2	6.0	2.2	2.4	10.5	5.0	1612± 32	1049 ± 9
miRFP720	45.1	2.3	4.4	2.2	72.2	2.2	1898 ± 36	1265 ± 32

[a]56-58 mW/mm^2 illumination power;
[b]relative to intracellular brightness of emiRFP670 in Cy5-LP channel;
[c]represented as fold increase of fluorescence upon administration of 25 μM relative to no BV value on the left;
ND – non determined, fluorescence was not detectable or too low.

Supplementary Table 5. Cytotoxicity of NIR FPs in HEK cells.

Protein	Apoptotic cell ratio (%)		Ratio (fold)		Dead cell ratio (%)
	NIR-FP positive	NIR-FP negative	NIR-FP positive/ NIR-FP negative	NIR-FP positive/ Dummy DNA	
mNeptune2.5	15.99	5.00	3.20	3.72	2.81
mCardinal	13.62	5.54	2.46	3.17	2.84
E2-Crimson	11.93	6.75	1.77	2.77	7.20
smURFP	27.40	8.31	3.30	6.37	6.35
BDFP1.6	8.00	5.10	1.57	1.86	1.96
emiRFP670	6.03	5.28	1.14	1.40	3.55
miRFP670-2	5.84	3.50	1.67	1.36	1.79
iRFP670	6.54	5.86	1.12	1.52	3.92
miRFP680	3.35	3.64	0.92	0.78	2.49
iRFP682	5.97	5.82	1.03	1.39	3.37
emiRFP703	5.65	5.23	1.08	1.31	3.37
BDFP1.8	6.51	3.83	1.70	1.51	2.19
miRFP2	26.48	10.50	2.52	6.16	5.53
mIFP	9.43	5.17	1.82	2.19	2.34
IFP2	4.73	3.84	1.23	1.10	2.33
mRhubarb713	5.50	6.73	0.82	1.28	4.36
miRFP713	5.63	5.59	1.01	1.31	3.66
iRFP713	4.47	6.31	0.71	1.04	4.20
SNIFP	6.66	3.65	1.82	1.55	1.75
mRhubarb719	9.92	3.59	2.76	2.31	1.81
mRhubarb720	11.19	4.79	2.34	2.60	2.43
miRFP720	4.44	5.47	0.81	1.03	3.85
Dummy DNA	NA	4.30	NA	NA	2.95

See **Supplementary Figure 7** and **Methods** section for experimental details.

Supplementary Table 6. Top 5 NIR FPs in live HEK cells and live neurons in three spectral channels.

Live HEK					
Cy5-LP		**Cy5-BP**		**Cy5.5**	
Protein	Product±SEM	Protein	Product±SEM	Protein	Product±SEM
miRFP680	3199±6	miRFP680	2105±4	iRFP713	1770±3
miRFP713	2448±4	mCardinal	935±1	miRFP713	1504±2
iRFP713	1918±6	iRFP682	687±2	miRFP680	1224±2
mCardinal	1397±2	BDFP1.8	609±1	mRhubarb713	1121±1
BDFP1.8	1344±3	emiRFP670	598±1	emiRFP703	1025±1
Live neurons					
Cy5-LP		**Cy5-BP**		**Cy5.5**	
Protein	Product±SEM	Protein	Product±SEM	Protein	Product±SEM
miRFP713	63865±653	miRFP680	23547±147	miRFP713	56422±560
miRFP680	35006±224	emiRFP670	15674±358	iRFP713	35353±662
iRFP713	28274±486	miRFP713	13310±143	miRFP720	29310±392
miRFP720	27483±361	miRFP670-2	5196±35	mRhubard713	17076±299
mRhubard713	22469±382	iRFP713	4989±86	miRFP680	13500±105
emiRFP670	22431±511				

Supplementary Table 7. Fluorescence retention, intracellular brightness, and intracellular photostability of NIR FPs in fixed HEK cells.

Protein	Fluorescence retention (%)[a]		Relative brightness vs miRFP680 in Cy5-LP (%)			Photostability (s)[b]	
	Cy5	Cy5.5	Cy5-LP	Cy5-BP	Cy5.5	Cy5	Cy5.5
mNeptune2.5	45 ± 27	34 ± 7[c]	26.1	16.8	0.0	632 ± 15	NA
mCardinal	26 ± 0.3	21 ± 5[c]	30.1	20.7	0.1	743 ± 23	NA
E2-Crimson	65 ± 3	54 ± 9[c]	92.1	62.5	0.1	119 ± 1	NA
smURFP	90 ± 15	92 ± 16[c]	33.2	23.5	0.9	436 ± 6	NA
BDFP1.6	65 ± 4	69 ± 4[c]	44.5	31.7	2.5	434 ± 7	NA
emiRFP670	70 ± 20	81 ± 24	58.0	40.2	6.6	831 ± 57	2985[d]
miRFP670-2	82 ± 3	93 ± 11[c]	40.4	28.6	3.3	524 ± 14	NA
iRFP670	79 ± 27	82 ± 23[c]	77.3	54.4	6.5	405 ± 6	NA
miRFP680	96 ± 45	98 ± 45	100.0	68.8	23.4	1401 ± 17	2256 ± 23
iRFP682	88 ± 2	92 ± 1	42.8	27.4	13.0	856 ± 13	1552 ± 22
emiRFP703	69 ± 22	72 ± 23	28.6	10.3	26.1	740 ± 12	791 ± 9
BDFP1.8	102 ± 8	115 ± 17	15.0	5.9	15.8	5007[d]	4514[d]
miRFP2	102 ± 55	104 ± 56	23.8	9.0	20.1	886 ± 11	937 ± 9
mIFP	61 ± 2	62 ± 3	34.1	11.2	38.0	398 ± 5	369 ± 8
IFP2	59 ± 13	60 ± 13	27.8	7.1	41.3	185 ± 6	93 ± 4
mRhubarb713	83 ± 10	99 ± 3	14.5	5.3	18.6	3734[d]	2042 ± 22
miRFP713	73 ± 19	72 ± 20	36.8	7.4	56.6	2899[d]	1518 ± 19
iRFP713	80 ± 1	83 ± 0.3	32.3	6.5	50.9	2207 ± 26	1403 ± 18
SNIFP	100 ± 33	103 ± 33	57.1	8.5	93.0	829 ± 15	475 ± 9
mRhubarb719	54 ± 4[c]	71 ± 14[c]	1.8	0.2	2.9	2421[d]	1505 ± 19
mRhubarb720	69 ± 18[c]	66 ± 15	3.2	0.3	5.4	1563 ± 37	1117 ± 4
miRFP720	73 ± 5	75 ± 6	80.8	7.8	138.3	1707 ± 18	1149 ± 13

[a]percentage of absolute brightness retention compared to brightness in live cells;
[b]mean half-times ± SEM;
[c]signal-to-background ≤ 2.0 based on absolute NIR brightness of fixed cells;
[d]50% photobleaching calculated via extrapolation;
NA – non applicable due to signal-to-background ≤ 2.0.

Supplementary Table 8. Intracellular brightness of the selected NIR FPs in acute brain slice, fixed brain slice, and fresh liver tissue.

Protein	Relative brightness in acute brain slice (%)									Relative brightness in fixed brain slice (%)			Relative brightness in fresh liver tissue (%)		
	Cy5-LP			Cy5-BP			Cy5.5			Cy5-LP	Cy5-BP	Cy5.5	Cy5-LP	Cy5-BP	Cy5.5
	1st month	2nd month	3rd month	1st month	2nd month	3rd month	1st month	2nd month	3rd month	1st month	2nd month	3rd month	5 days	5 days	5 days
mCardinal	8.6	18.0	12.5	6.0	11.7	10.4	0.3	1.2	1.2	3.2	1.9	1.0	32.7	16.6	9.4
emiRFP670	30.5	54.3	42.7	20.7	36.2	27.0	3.2	5.1	5.4	65.8	41.9	10.8	87.6	55.2	16.7
miRFP670-2	8.6	12.3	11.1	6.4	8.6	11.0	0.9	1.2	1.5	28.3	19.4	6.6	52.5	29.8	12.3
miRFP680	66.1	**100.0**	57.2	43.6	65.1	42.6	17.0	24.7	14.9	**100.0**	62.2	26.6	**100.0**	61.9	31.6
mRhubard713	3.5	6.5	7.8	0.8	1.6	2.3	6.4	6.8	9.4	17.9	3.6	26.1	44.1	20.4	18.3
miRFP713	8.3	39.9	33.9	2.0	9.4	6.8	14.2	43.7	46.7	49.4	10.5	93.3	59.9	23.0	44.4
iRFP713	10.6	29.0	20.5	2.0	6.5	6.2	18.6	37.9	41.6	40.7	8.5	76.2	51.5	20.8	28.3
miRFP720	18.9	37.1	24.2	2.3	4.4	2.7	36.6	45.5	36.0	34.8	4.7	66.6	59.5	17.7	55.0

Relative brightness in acute brain slices, fixed brain slices, and fresh liver tissue was normalized independently.

Supplementary Table 9. Intracellular photostability of the selected NIR FPs in acute and fixed brain slices.

Protein	Photostability in Cy5-LP (s)		Photostability in Cy5.5 (s)[a]	
	Acute brain slice	Fixed brain slice	Acute brain slice	Fixed brain slice
mCardinal	1250	570	ND	ND
emiRFP670	510	9025[b]	ND	ND
miRFP670-2	1684[b]	960	ND	ND
miRFP680	7827[b]	1310	1100	1070
mRhubarb713	5905[b]	2550	2237[b]	1030
miRFP713	9028[b]	14322[b]	4032[b]	2324[b]
iRFP713	6409[b]	3800	1300	1937[b]
miRFP720	1560	2188[b]	845[b]	1710

[a]56-58 mW/mm^2 illumination power;
[b]50% photobleaching estimated via extrapolation.

Supplementary Table 10. Intracellular brightness and photostability of the selected NIR FPs in zebrafish larvae.

Protein	**Relative brightness (%)**				**Photostability (s)**		**Product**
	Hindbrain		**Spinal cord**		**Spinal cord**		**Spinal cord**
	with HO1-H25A	**with wtHO1**	**with HO1-H25A**	**with wtHO1**	**with HO1-H25A**	**with wtHO1**	**with wtHO1**
mCardinal	56.6[a]	ND	47.4[a]	ND	257.8[a]	ND	52.2[a]
emiRFP670	25.6	76.2	38.7	95.6	114.4	245.2	100.0
miRFP670-2	17.9	33.3	31.2	37.3	22.1	46.1	7.3
miRFP680	22.6	81.7	26.2	**100.0**	29.3	87.4	37.3
mRhubarb713	3.7	6.6	4.4	7.8	199.7	200.6	6.7
miRFP713	4.9	5.9	6.7	7.7	276.9	488.4	16.1
iRFP713	5.4	7.2	6.7	12.3	245.6	407.0	21.4
miRFP720	18.6	31.0	19.5	37.7	161.6	280.2	45.1
emiRFP2	6.0	24.5	8.1	26.6	128.1	145.6	16.5

[a]mCardinal expressed without HO1-H25A, see **Supplementary Figure 14** for details.

Supplementary Table 11. Intracellular brightness and photostability of the selected NIR FPs in *C. elegans*.

Protein	Relative Brightness (%) vs miRFP680			Photostability (s)[a]	
	Cy5-LP	Cy5-BP	Cy5.5	Cy5-LP	Cy5.5
mCardinal	16.7	12.4	0.04	9,155[b]	NA
emiRFP670	65.7	45.6	9.5	1,836[b]	1,756[b]
miRFP670-2	25.8	17.9	2.0	620	2,244[b]
miRFP680	**100**	69.4	31.9	NA	NA
mRhubarb713	21.5	4.2	33.8	NA	NA
miRFP713	33.3	6.9	50.7	NA	NA
iRFP713	29.6	5.9	45.0	6,271[b]	NA
miRFP720	10.2	1.1	13.8	NA	NA

[a]12.5 mW/mm^2 illumination power;
[b]values calculated via extrapolation;
NA – not applicable due to the fluorescence intensity decrease was less than 10% from initial value.

Supplementary Figure 1. Selection of the expression vector for intracellular brightness comparison in mammalian cells.

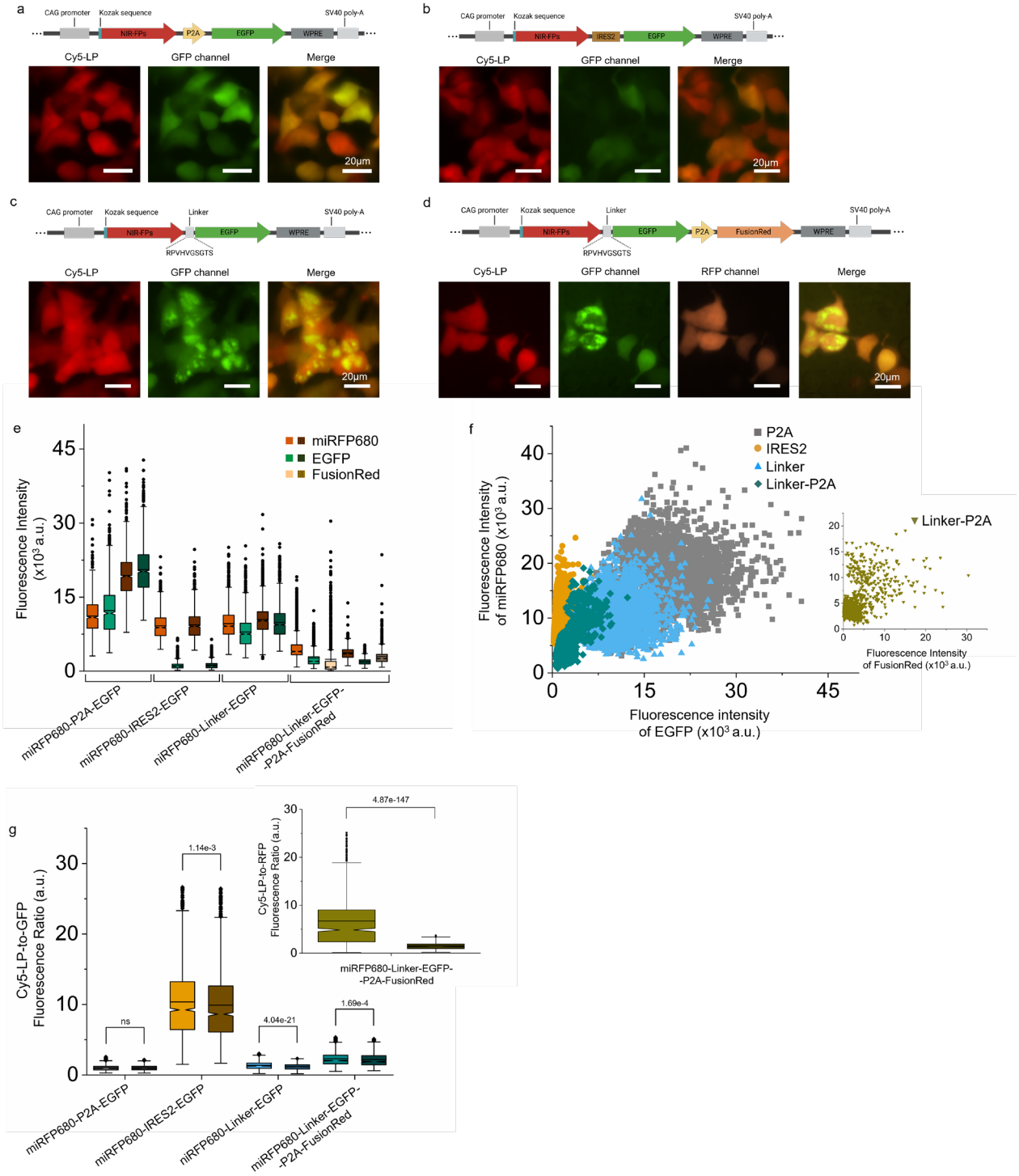

Comparison of four expression cassettes for intracellular brightness evaluation of NIR FPs in HEK293 cells. (**a-d**) Linear map of four expression cassettes (top) NIR-FPs-P2A-EGFP (P2A), NIR-FPs-IRES2-EGFP (IRES2), NIR-FPs-linker-EGFP (Linker), NIR-FPs-linker-EGFP-P2A-FusionRed (Linker-P2A), respectively. The genes are cloned under control of chicken beta-actin

(CAG) promoter followed by the woodchunk hepatitis virus post-translation regulatory element (WPRE) and SV40 sequence for transcription termination in all cassettes. Representative images of HEK293 cells expressing miRFP680 (NIR-FPs in linear map) with abovementioned cassettes (bottom) in the Cy5-LP and GFP channels (**a**-**c**), and under RFP channel (**d**) and merged. Imaging conditions were kept constant throughout imaging of all constructs. The dynamic range of all images was adjusted independently to facilitate visualization. Scale bars, 20 μm. (**e**) Notched box plot of absolute intracellular fluorescence of live HEK293 cells in Cy5-LP, GFP and RFP channels corresponding to each expression cassette (two independent transfections for each construct; per transfection n=1374, 1878 ROIs for P2A; n=2169, 1789 ROIs for IRES2; n=2153, 2358 ROIs for Linker; n=885, 724 ROIs for Linker-P2A). Box plots throughout: narrow part of notch, median; top and bottom of the notch, 95% confidence interval for the median; top and bottom horizontal lines, 25% and 75% percentiles for the data; whiskers extend 1.5× the interquartile range from the 25th and 75th percentiles; horizontal line, mean; dots, outliers. (**f**) Correlation of intracellular brightness between Cy5-LP and EGFP fluorescence intensity and Cy5-LP and FusionRed (inset) (n=3252, 3958, 4511, and 1609 ROIs for P2A, IRES2, Linker and Linker-P2A, respectively; two independent transfections each). Pearson's correlation coefficients: r_{P2A}=0.44 (p-value=8.83e-156), r_{IRES2}=0.33 (p-value=2.76e-106), r_{Linker}=0.24 (p-value=9.92e-60), $r_{Linker\text{-}P2A}$=0.73 Cy5-LP with GFP (p-value=2.08e-276) $r_{Linker\text{-}P2A}$=0.51 Cy5-LP with RFP (p-value=1.68e-107). Grey squares, P2A; yellow circles, IRES2; blue upright triangles, Linker; cyan diamonds, Linker-P2A (Cy5-LP, GFP); dark yellow down-pointing triangles, Linker-P2A (Cy5-LP, RFP). (**g**) Comparison of intracellular Cy5-LP-to-GFP ratios and Cy5-LP-to-RFP ratios (inset) in live HEK293 cells expressing miRFP680 using P2A, IRES2, Linker and Linker-P2A constructs from two independent transfection each (n=1374, 1878 ROIs for P2A; n=2169, 1789 ROIs for IRES2; n=2153, 2358 ROIs for Linker; n=885, 724 ROIs for Linker-P2A; two-sided Kolmogorov-Smirnov two-sample test results for pairwise comparison of ratios between transfections in **Supplementary Table 1**; p-values shown in graph).

Supplementary Figure 2. Fluorescence imaging of live HEK cells co-expressing NIR FPs with GFP.

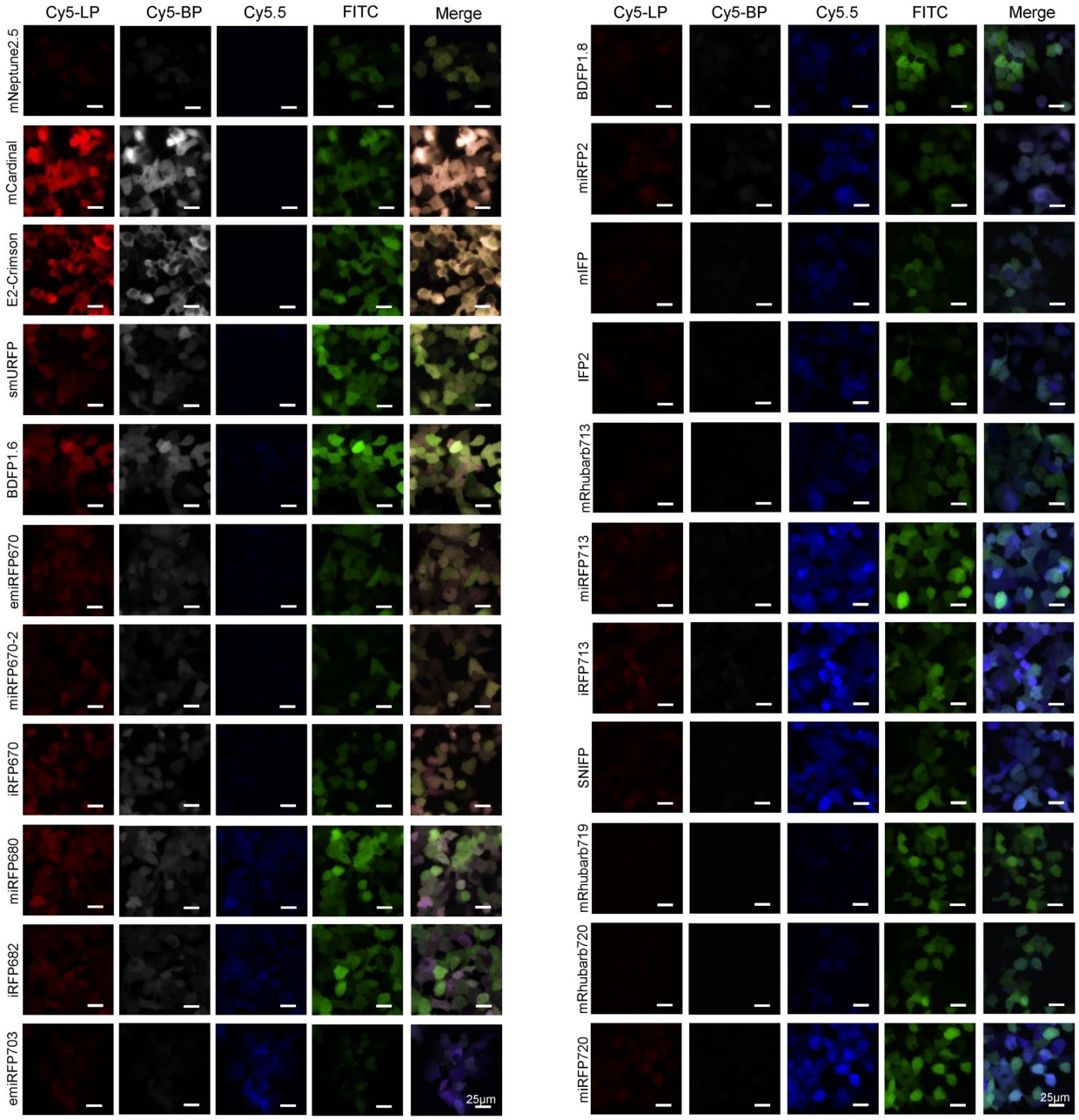

Representative fluorescence images of live HEK cells transiently transfected with pAAV-CAG-NIR-FPs-P2A-EGFP plasmids in Cy5-LP, Cy5-BP, Cy5.5 and FITC channels (n>1945 cells for each NIR FP from two independent transfections; see **Supplementary Table 2** for the detailed descriptive statistics). All images for the same channel are presented with identical LUT settings. Scale bar, 25 μm.

Supplementary Figure 3. Fluorescence imaging of live primary cultured mouse neurons co-expressing NIR FPs with GFP.

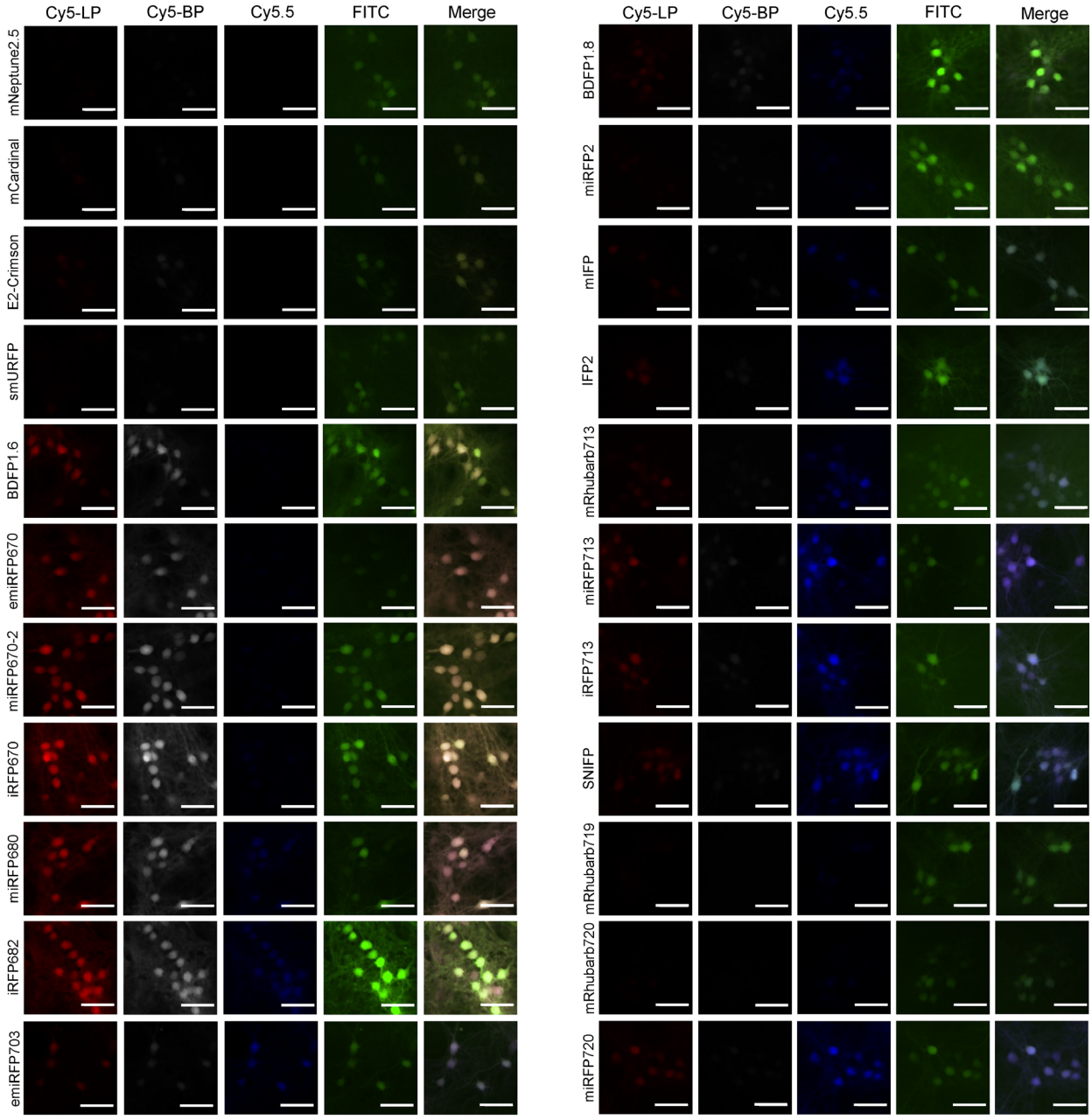

Representative fluorescence images of live primary culture mouse neurons transduced with rAAV2/9-CAG-NIR-FPs-P2A-EGFP in Cy5-LP, Cy5-BP, Cy5.5, and FITC channels (n>44 neurons for each NIR FP from two independent transductions; see **Supplementary Table 2** for the detailed descriptive statistics). All images for the same channel are presented with identical LUT settings. Scale bar, 50 μm.

Supplementary Figure 4. Correlations of quantitative characteristics of NIR FPs.

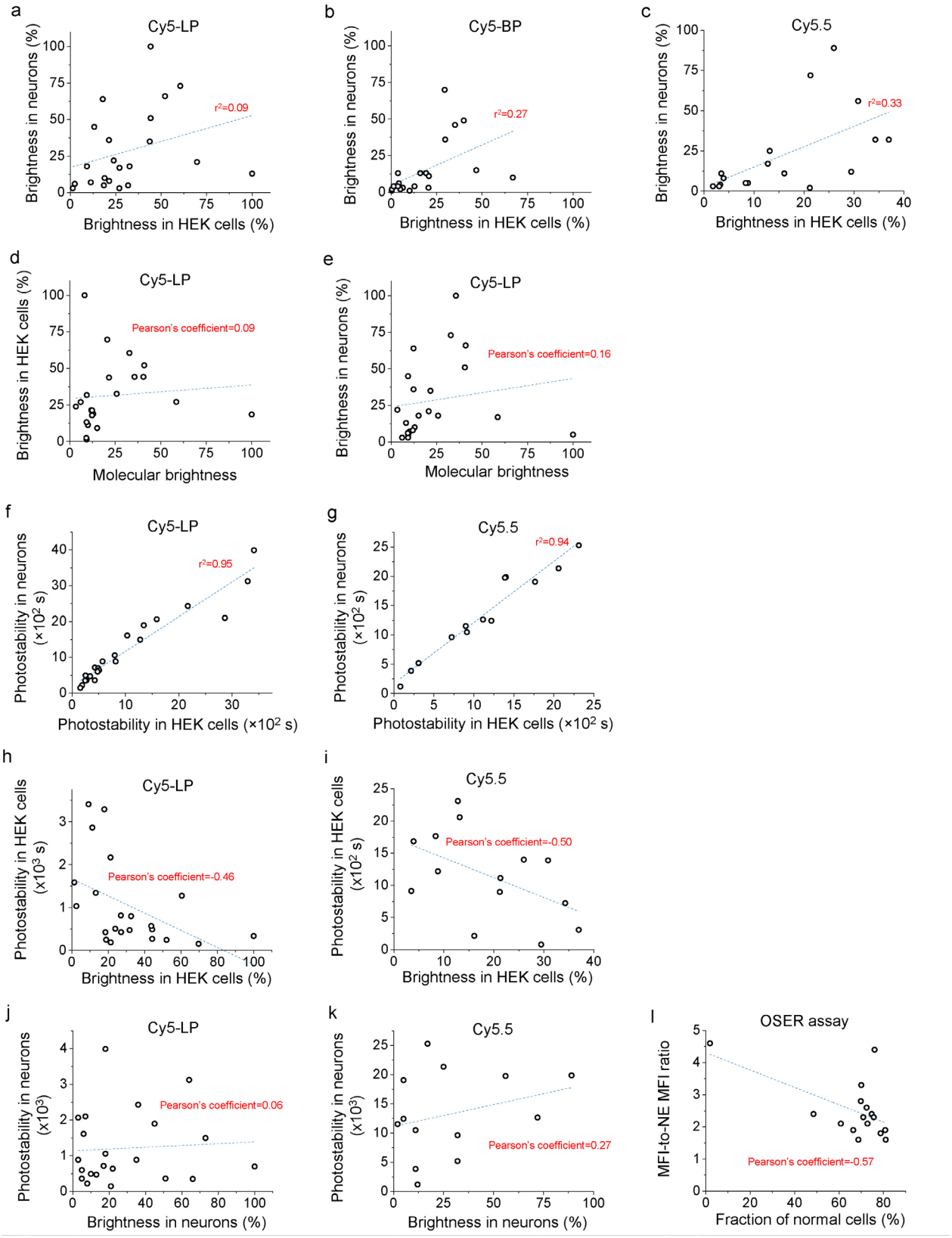

(**a**, **b**, **c**) Correlation of intracellular brightness in live HEK cells and neurons in (**a**) Cy5-LP, (**b**) Cy5-BP, and (**c**) Cy5.5 channels. (**d**) Correlation of molecular brightness and intracellular brightness in live HEK cells in Cy5-LP channel (molecular brightness was corrected for excitation and emission efficiency in Cy5-LP channel). (**e**) Correlation of molecular brightness and intracellular brightness in live neurons in Cy5-LP channel (molecular brightness was corrected for excitation and emission efficiency in Cy5-LP channel). (**f**, **g**) Correlation of intracellular photostability in live HEK cells and neurons in (**f**) Cy5-LP, (**g**) Cy5.5 channels. (**h**, **i**) Correlation of intracellular brightness and photostability in live HEK cells in (**h**) Cy5-LP and (**i**) Cy5.5 channels. (**j**, **k**) Correlation of intracellular brightness and photostability in live neurons in (**j**) Cy5-LP and (**k**) Cy5.5 channels. (**i**) Correlation of fraction of normal cells and MFI-to-NE ratio in live HeLa cells.

Supplementary Figure 5. Western blot analysis of NIR FPs co-expression with GFP.

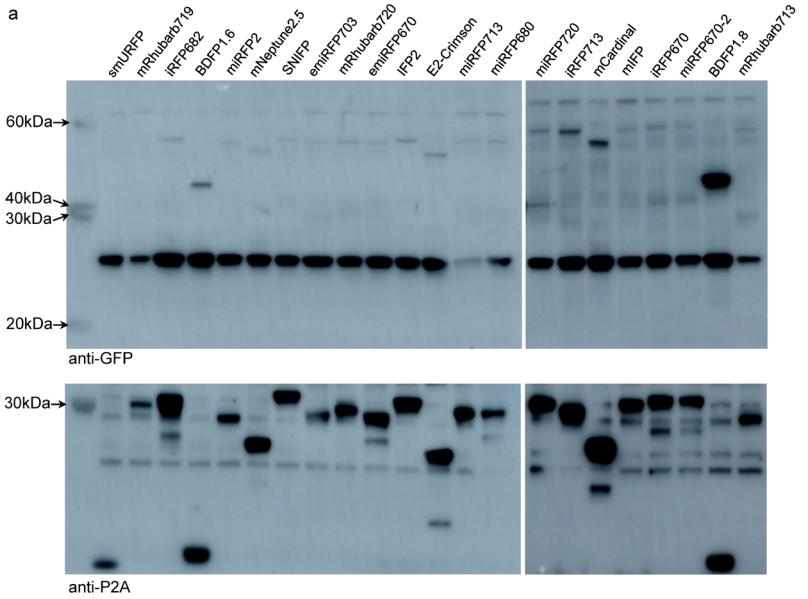

b

Construct	Cleavage rate (%)	P2A to GFP ratio
pAAV-CAG-smURFP-P2A-GFP	99	0.39
pAAV-CAG-mRhubarb719-P2A-GFP	99	0.48
pAAV-CAG-iRFP682-P2A-GFP	98	1.01
pAAV-CAG-BDFP1.6-P2A-GFP	92	0.47
pAAV-CAG-miRFP2-P2A-GFP	97	0.37
pAAV-CAG-mNeptune2.5-P2A-GFP	98	1.12
pAAV-CAG-SNIFP-P2A-GFP	97	1.04
pAAV-CAG-emiRFP703-P2A-GFP	97	0.31
pAAV-CAG-mRhubarb720-P2A-GFP	96	0.72
pAAV-CAG-emiRFP670-P2A-GFP	98	0.66
pAAV-CAG-IFP2-P2A-GFP	95	1.17
pAAV-CAG-E2-Crimson-P2A-GFP	94	1.11
pAAV-CAG-miRFP713-P2A-GFP	77	6.25
pAAV-CAG-miRFP680-P2A-GFP	91	0.84
pAAV-CAG-miRFP720-P2A-GFP	92	0.87
pAAV-CAG-iRFP713-P2A-GFP	87	0.50
pAAV-CAG-mCardinal-P2A-GFP	89	1.09
pAAV-CAG-mIFP-P2A-GFP	95	0.50
pAAV-CAG-iRFP670-P2A-GFP	96	0.39
pAAV-CAG-miRFP670-2-P2A-GFP	95	0.38
pAAV-CAG-BDFP1.8-P2A-GFP	53	0.30
pAAV-CAG-mRhubard713-P2A-GFP	90	0.69

c

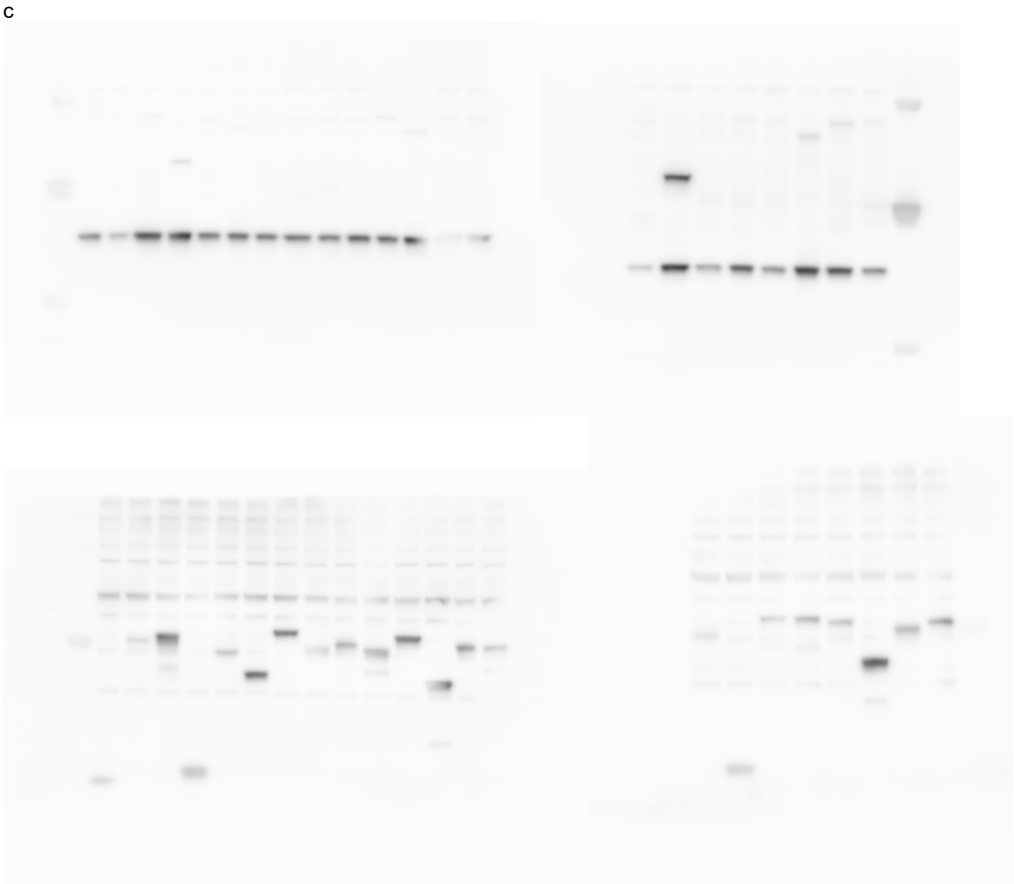

(**a**) Western blot analysis of cleavage efficiency of P2A and co-expression ratio of FPs in HEK cells using staining with anti-GFP antibodies (upper images) and anti-P2A antibodies (lower images). (**b**) Quantitation of cleavage rate of P2A calculated as cleavage rate = cleaved form/

(cleaved form + uncleaved form) using anti-GFP staining and co-expression ratio calculated as ratio = cleaved form stained with anti-P2A/cleaved form stained with anti-GFP. (**c**) Raw images of Western blot gels shown in panel a. The raw Western blot files are available for download at FigShare (https://figshare.com/authors/Hanbin_Zhang/14524646).

Supplementary Figure 6. Post-translational modifications and sequence coverage of the selected NIR FPs identified using MS analysis.

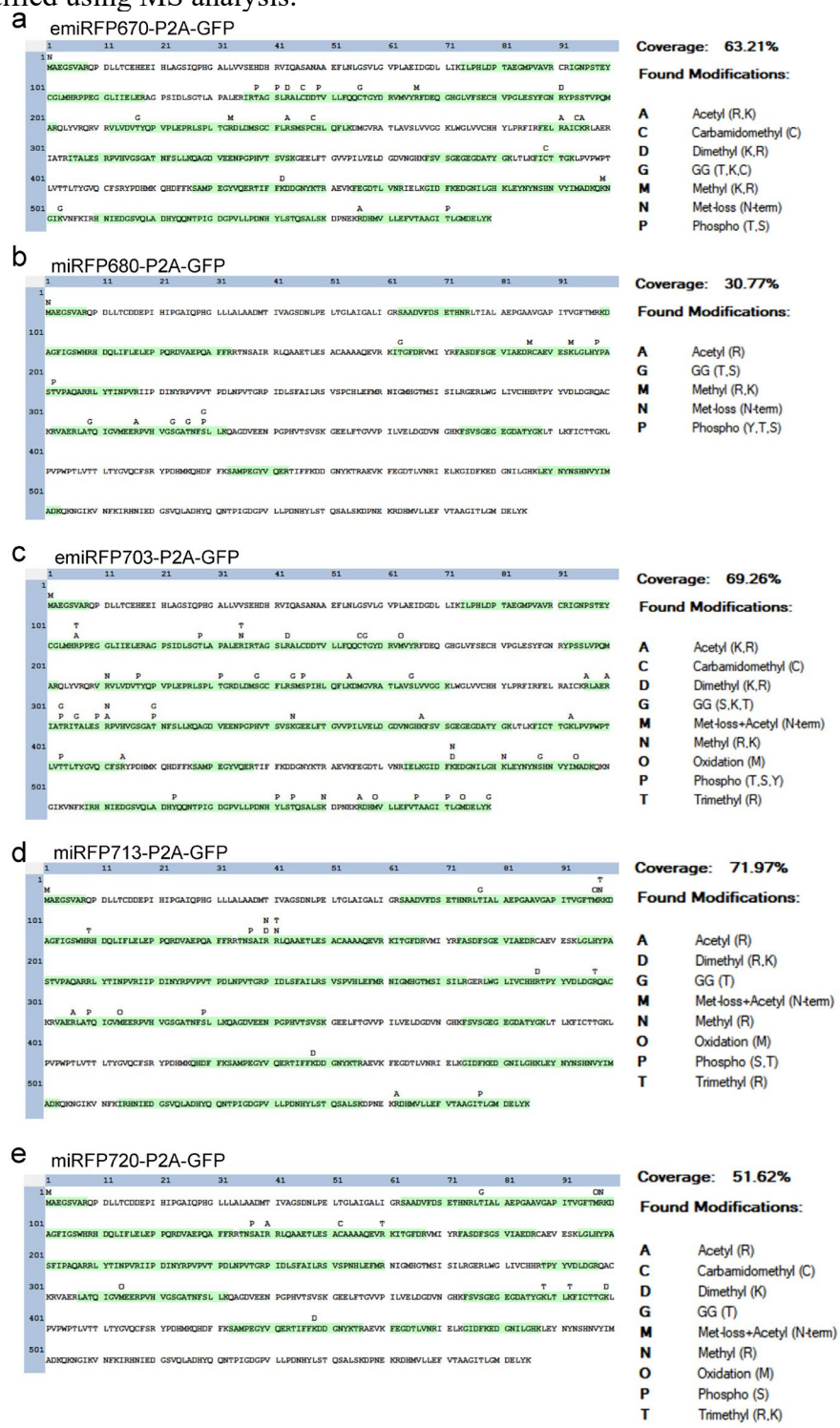

(**a-e**) Post-translational modifications and sequence coverage of (**a**) emiRFP670-P2A-GFP, (**b**) miRFP680-P2A-GFP, (**c**) emiRFP703-P2A-GFP, (**d**) miRFP713-P2A-GFP, (**e**) miRFP720-P2A-GFP identified using MS analysis (see **Method** section for experimental details). Amino acid sequences highlighted with green correspond to the identified peptides.

Supplementary Figure 7. Gating strategy applied for analysis of cytotoxicity in HEK cells using flow cytometry.

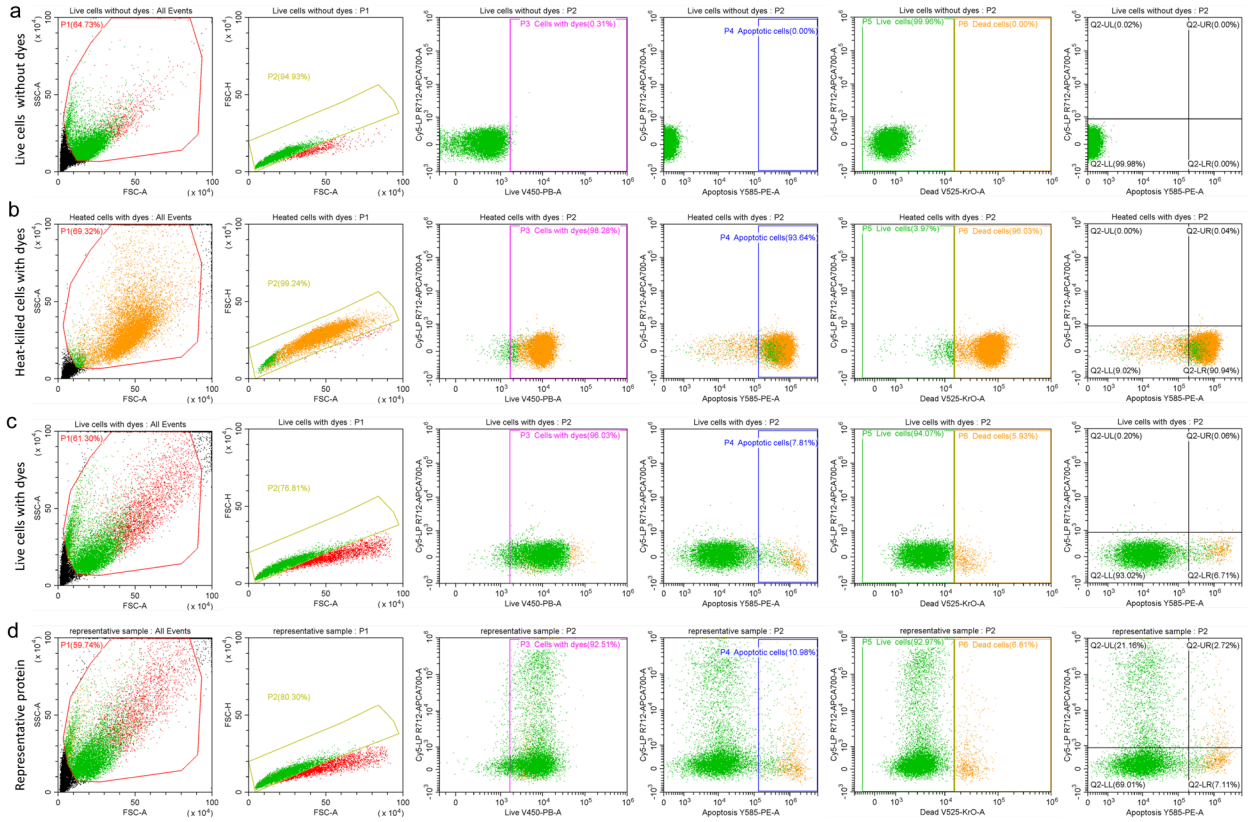

Figure illustrates the gating strategy used to analyze the live cells, dead cells and apoptotic cells using flow cytometry. (**a**) Live HEK cells without staining, (**b**) heat-treated HEK cells and (**c**) live HEK cells stained with the dyes indicating live, dead and apoptotic, according to the protocols in the LIVE/DEAD Violet Viability/Vitality kit (L34958, ThermoFisher) and the Alexa Fluor™ 568 conjugate kit (A13202, ThermoFisher) with minor changes (see **Methods** for details). Compared to gate P3 of panel **a**, cells stained with dyes from other samples (panels **b-d**) can be well separated from unstained cells in Live V450-PB-A channel, which indicates that calcein can label cells, but the Live V450-PB-A channel cannot distinguish live and dead cells. Comparison of P4 gate in panel **b** with that in other panels indicates that heat-treated sample have a higher percentage of apoptotic cells thus annexin V conjugate can well distinguish apoptotic cells in Apoptosis Y585-PE-A channel. In Dead V525-KrO-A channel, P6 in panel **b** shows that aqua-fluorescent reactive dye can well stain dead cells and gate out of live cells effectively compared to the P6 of other panels. So, the value of P4, P5 and P6 can indicate the percentage of apoptotic, live and dead cells, respectively. In panel **d**, channel Cy5-LP R712-APCA700-A was used to gate out of HEK cells transfected with NIR-FPs from non-transfected cells.

Supplementary Figure 8. Fluorescence imaging of fixed HEK cells co-expressing NIR FPs with EGFP.

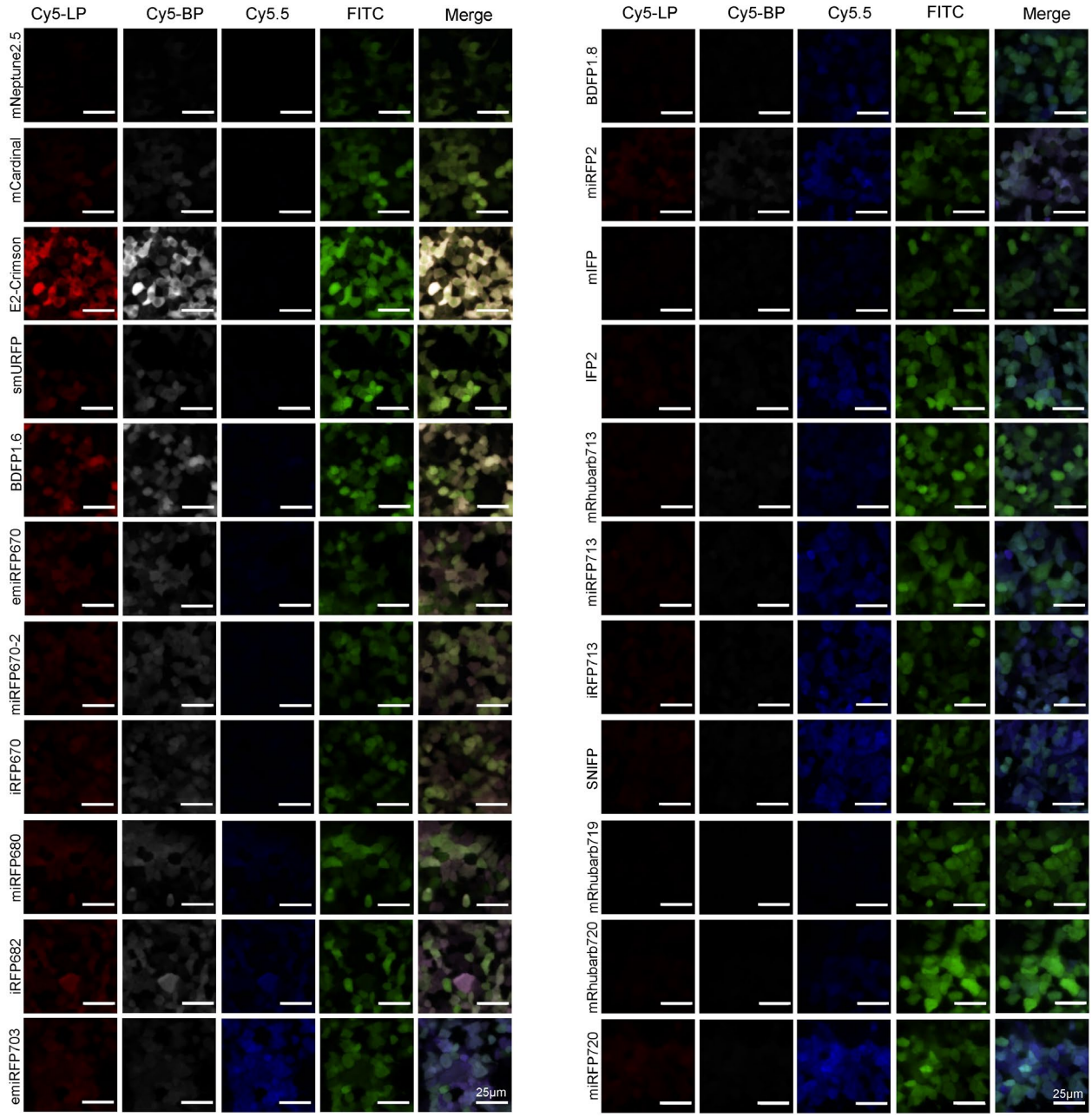

Representative fluorescence images of PFA-fixed HEK cells transiently transfected with pAAV-CAG-NIR-FPs-P2A-EGFP plasmids in Cy5-LP, Cy5-BP, Cy5.5, and FITC channels (n>1974 cells for each NIR-FP from two independent transfections). All images for the same channel are presented with the identical LUT settings. Scale bar, 25 μm.

Supplementary Figure 9. Representative live HeLa cells expressing CytERM-NIR-FPs fusions.

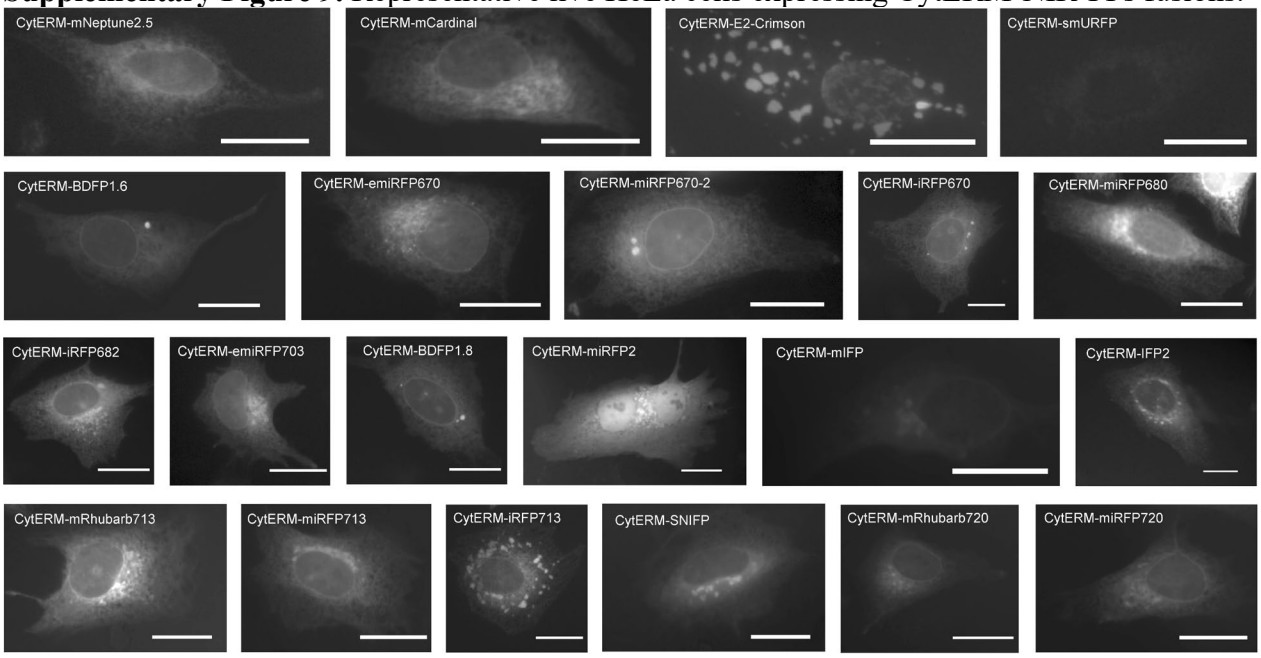

Representative wide-field fluorescence images of transiently transfected HeLa cells (n>250 cells for each construct from two independent transfection). The images of cells expressing corresponding proteins are ordered from top left to bottom right by increasing excitation maximum as in **Extended Data Table 1**. mRhubarb719 is not shown due to poor performance in this fusion. See **Supplementary Dataset 1** for detailed descriptive statistics for both assays. The dynamic range of the images was adjusted independently to facilitate visualization and images were generated through maximum projection. Scale bars: 25μm.

Supplementary Figure 10. Representative live HeLa cells expressing CytERM fusions of NIR-FPs excluded from or used in OSER assay and MFI ratio calculation.

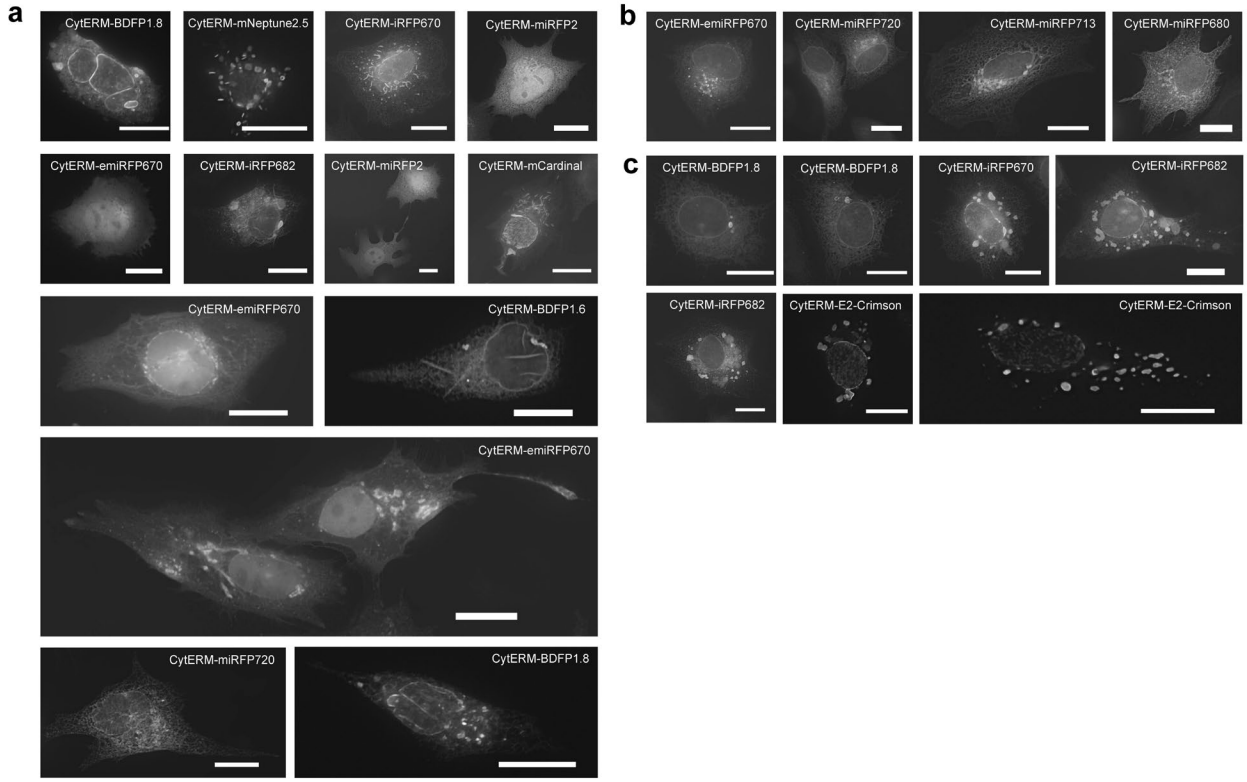

(**a**) Cells excluded from analysis. Stressed cells, cells with multilobed nuclei, cells with high cytoplasmic fraction or mislocalized fusions, cells with distorted ER architecture, needle-like structures, or non-whorl structures (n>2000 cells for each construct from two independent transfection). (**b**) Representative HeLa cells with normal ER architecture. In CytERM-emiRFP670 and CytERM-miRFP713 the visible structures in the proximity of the nucleus were not considered as whorl structures (n>250 cells for each construct from two independent transfection). (**c**) Representative HeLa cells with whorls included in the analysis (n>250 cells for each construct from two independent transfection). Only lamellae were used in analysis; regions of nuclear envelope presenting high brightness were excluded from MFI ratio analysis according to Costantini *et al.*[6]. In all images the dynamic ratio was adjusted independently to facilitate visualization and images were generated through maximum projection; scale bars represent 25µm.

Supplementary Figure 11. Absorbance and steady-state fluorescence spectra of the selected NIR FPs.

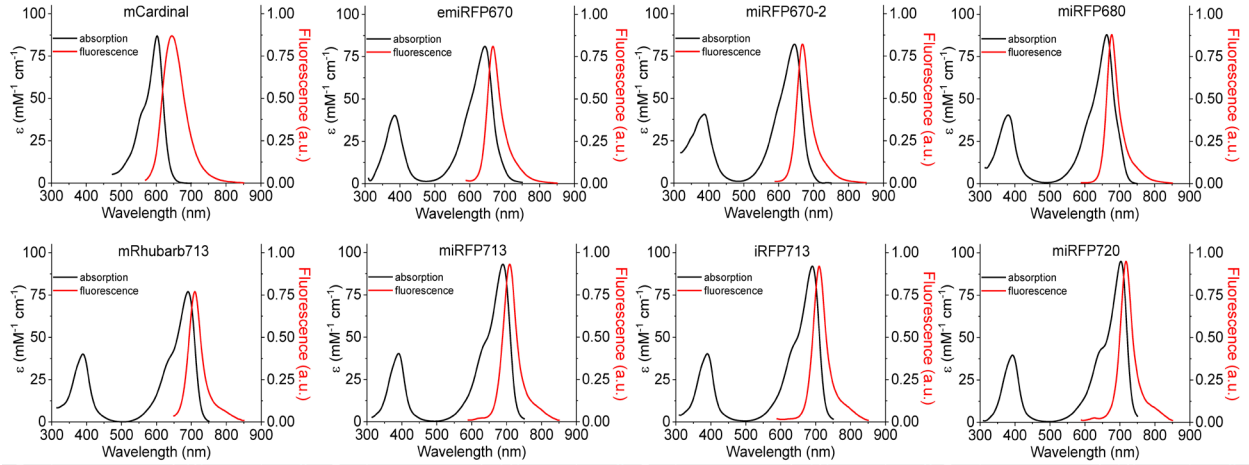

Absorbance (black line) and steady-state fluorescence spectra of mCardinal, emiRFP670, miRFP670-2, miRFP680, mRhubarb713, miRFP713, iRFP713, and miRFP720 measured in PBS at pH 7.4.

Supplementary Figure 12. pH dependence of fluorescence for the selected NIR FPs.

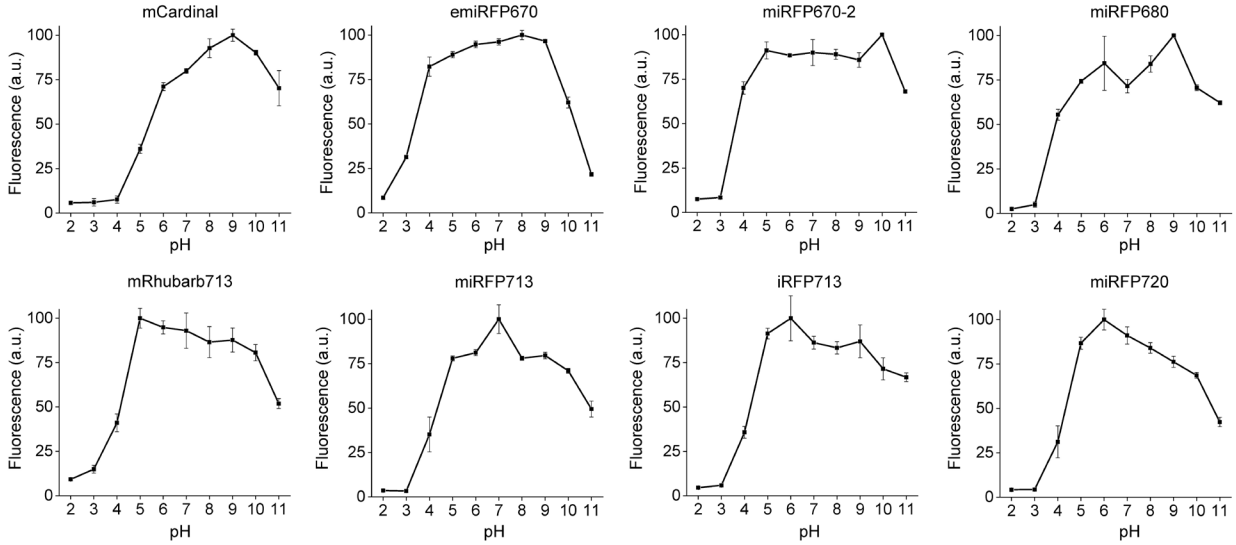

Equilibrium pH dependence of fluorescence of mCardinal, emiRFP670, miRFP670-2, miRFP680, mRhubarb713, miRFP713, iRFP713, and miRFP720 measured in the range of pH from 2 to 11 (n=3 technical replicates for each protein; squares, mean; bars, SEM).

Supplementary Figure 13. Confocal imaging of NIR FPs in PFA-fixed brain slices.

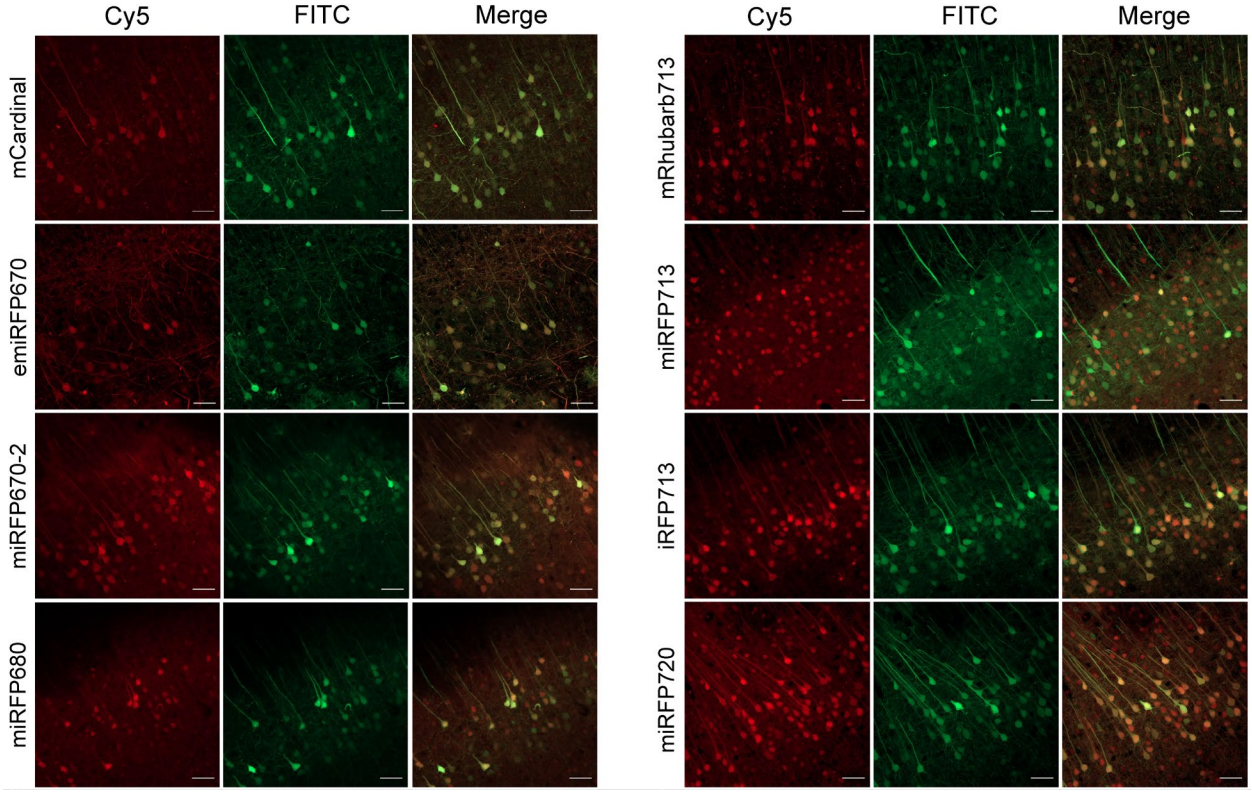

Representative confocal fluorescence images of fixed brain slices expressing NIR-FPs-P2A-GFP in L2/3 cortical neurons (n=2 slices from one or two mice for each protein). Imaging conditions, Cy5: excitation 639 nm, emission 655-735 nm; FITC: excitation 488 nm, emission 500-550 nm. The NIR FP expression was achieved via the rAAV2/9-CAG-NIR-FPs-P2A-GFP injection at the neonatal stage followed by fixed brain slice preparation at 1-month post injection. To facilitate visual comparison of FPs' localization, the dynamic range was adjusted independently for each image and images were generated through maximum projection. Scale bars, 50 μm.

Supplementary Figure 14. Validation of the neuron-specific polycistronic expression vectors in zebrafish larvae.

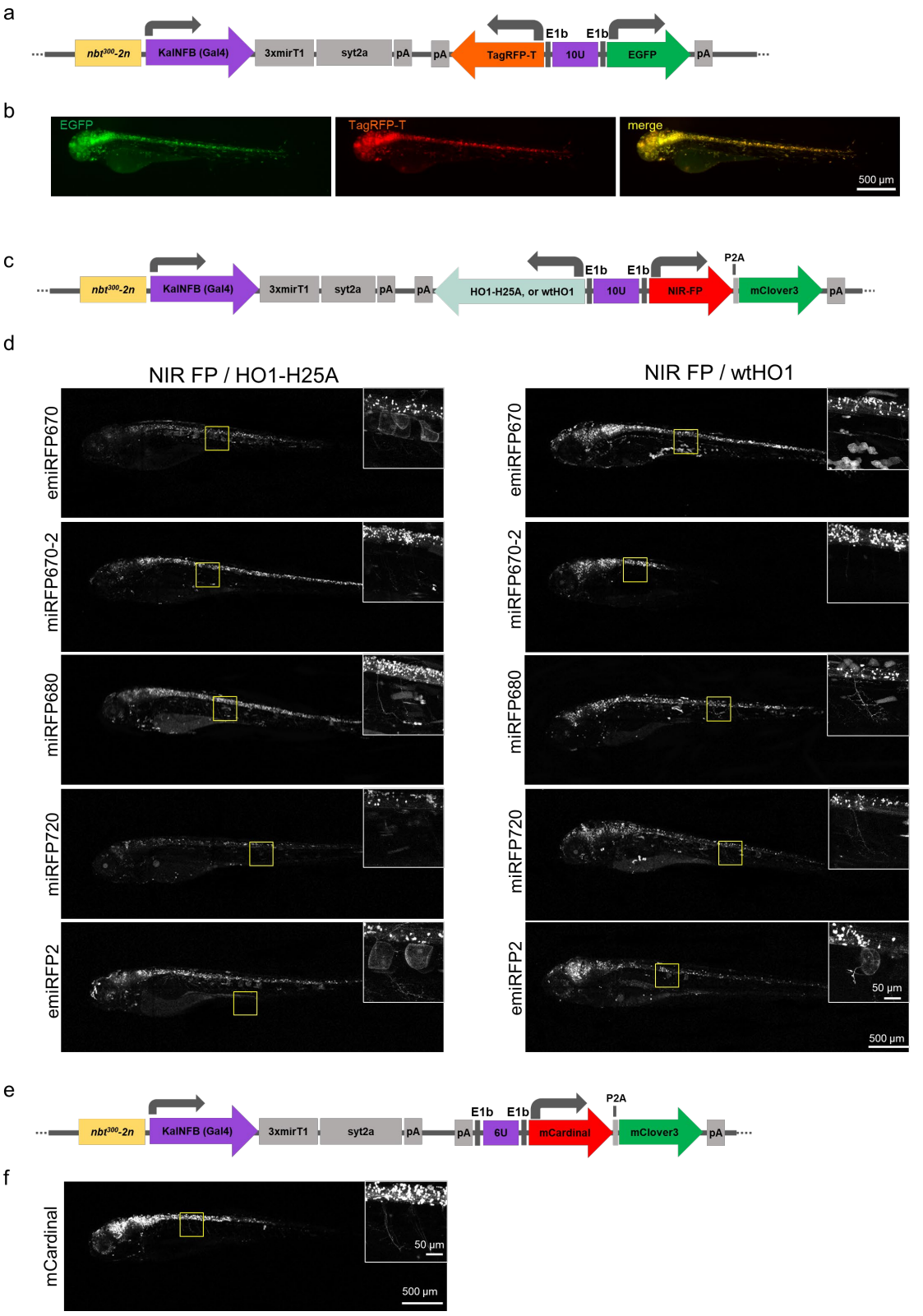

(**a**) Schematic representation of polycistronic expression cassette designed for neuron-specific expression of target FPs in zebrafish larvae (see **Methods** section for the details of the vector design). (**b**) Validation of neural expression of EGFP and TagRFP-T controlled by bidirectional promoter in zebrafish larvae at 4 dpf (representative image from n=4 fish). Imaging conditions: Leica stereomicroscope (MZ205FA); GFP3: excitation, 450-490nm, emission, 500-550; Texas Red: excitation, 540-580nm, emission, 610LP. The dynamic range of each image was adjusted independently and processed to show different colors for each. Scale bar, 500μm. (**c**) Schematic representation of polycistronic expression cassette used for neuron-specific co-expression of NIR FPs, mClover3, and wtHO1/HO1-H25A (wild-type HO1/enzymatically inactive HO1 mutant) in zebrafish larvae (see **Methods** section for the details of the vector cloning). (**d**) Representative images of 4 dpf zebrafish larvae co-expressing selected NIR FPs with HO1-H25A (left) or wtHO1 (right) (n=4 fish for each protein). Imaging conditions: Leica SP8; excitation, 633 nm, emission 645-780 nm. Scale bars: 500 μm, 50 μm (inset). (**e**) Schematic representation of polycistronic expression cassette used for co-expression of mCardinal and mClover3 without HO1 expression. (**f**) Representative images of 4 dpf zebrafish larvae co-expressing mCardinal and mClover3 without HO1 expression (n=4 fish). Imaging conditions: Leica SP8; excitation, 633 nm, emission 645-780 nm. Scale bars: 500 μm, 50 μm (inset). For (**d**, **f**) Z-stack projected images were generated, followed by applying the same dynamic range to all images.

Supplementary Figure 15. Representative images of zebrafish hindbrain neurons co-expressing selected NIR FPs with mClover3.

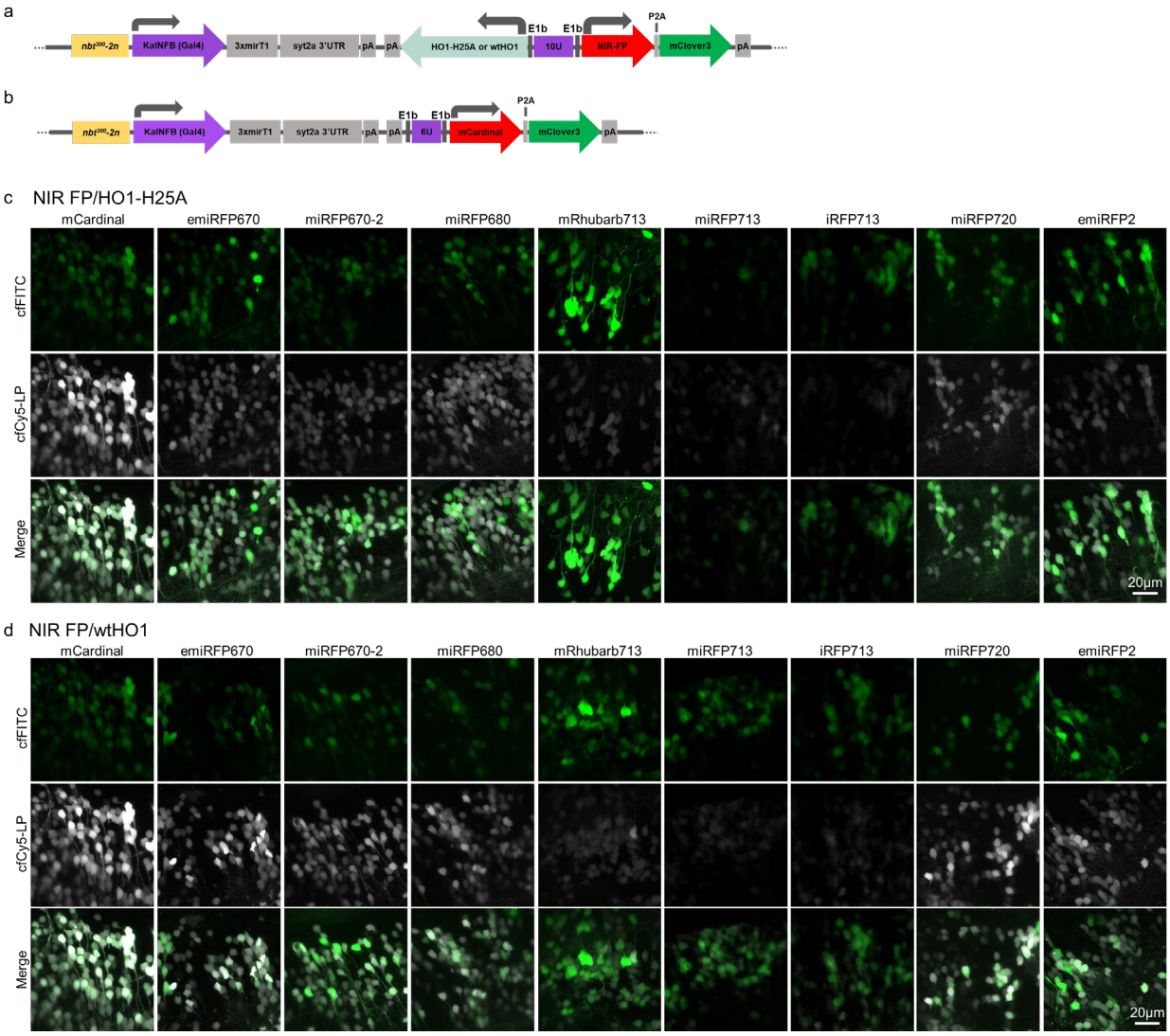

(**a**) Schematic representation of polycistronic expression cassette used for neuron-specific co-expression of NIR FPs, mClover3, and wtHO1/HO1-H25A (wild-type HO1/enzymatically inactive HO1 mutant) in zebrafish larvae. (**b**) Schematic representation of polycistronic expression cassette used for co-expression of mCardinal and mClover3 without HO1 (see **Methods** section for the details of the vector design). (**c**) Representative confocal fluorescence images of 4 dpf larval hindbrain neurons co-expressing each NIR FP with mClover3 and HO1-H25A (n=120 neurons form 4 fish for each protein). Z-stack projected images were generated, followed by applying the same dynamic range to all images for each channel. The images are further processed to show their signals detected in 2 different channels as different colors (Fiji software). (**d**) Representative confocal fluorescence images of 4 dpf larval hindbrain neurons co-expressing each NIR FP with mClover3 and wtHO1 (n=120 neurons form 4 fish for each protein). Imaging conditions: Leica SP8: cfFITC, excitation 488 nm, emission 496-530 nm; cfCy5-LP, excitation 633 nm, emission 645-780 nm. Scale bars, 20 μm.

Supplementary Figure 16. Representative images of zebrafish spinal cord neurons co-expressing selected NIR FPs with mClover3.

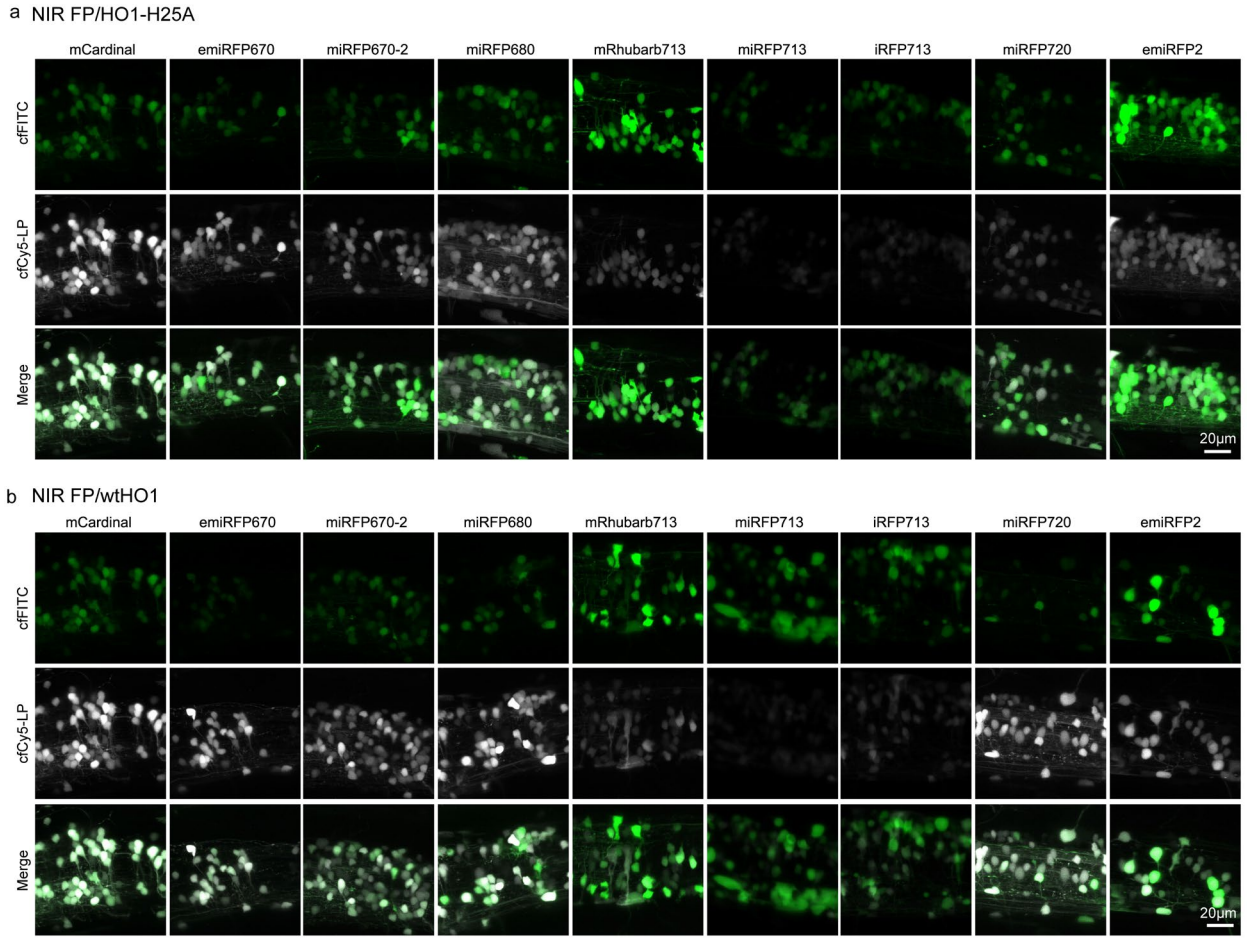

(**a**) Representative confocal fluorescence images of 4 dpf spinal cord neurons co-expressing each NIR FP with mClover3 and an inactive variant of HO1 (HO1-H25A, n=120 neurons from 4 fish for each protein). (**b**) Representative confocal fluorescence images of spinal cord neurons co-expressing each NIR FP with mClover3 and wild-type HO1 (wtHO1, n=120 neurons from 4 fish for each protein). Imaging conditions: Leica SP8; cfFITC, excitation: 488 nm; emission 496-530 nm; cfCy5-LP, excitation 633 nm, emission 645-780 nm. Z-stack projected images were generated, followed by applying the same dynamic range to all images for each channel. The images are further processed to show their signals detected in 2 different channels as different colors (Fiji software). Scale bars, 20 μm.

Supplementary Figure 17. Photobleaching of selected NIR FPs in spinal cord neurons in zebrafish larvae.

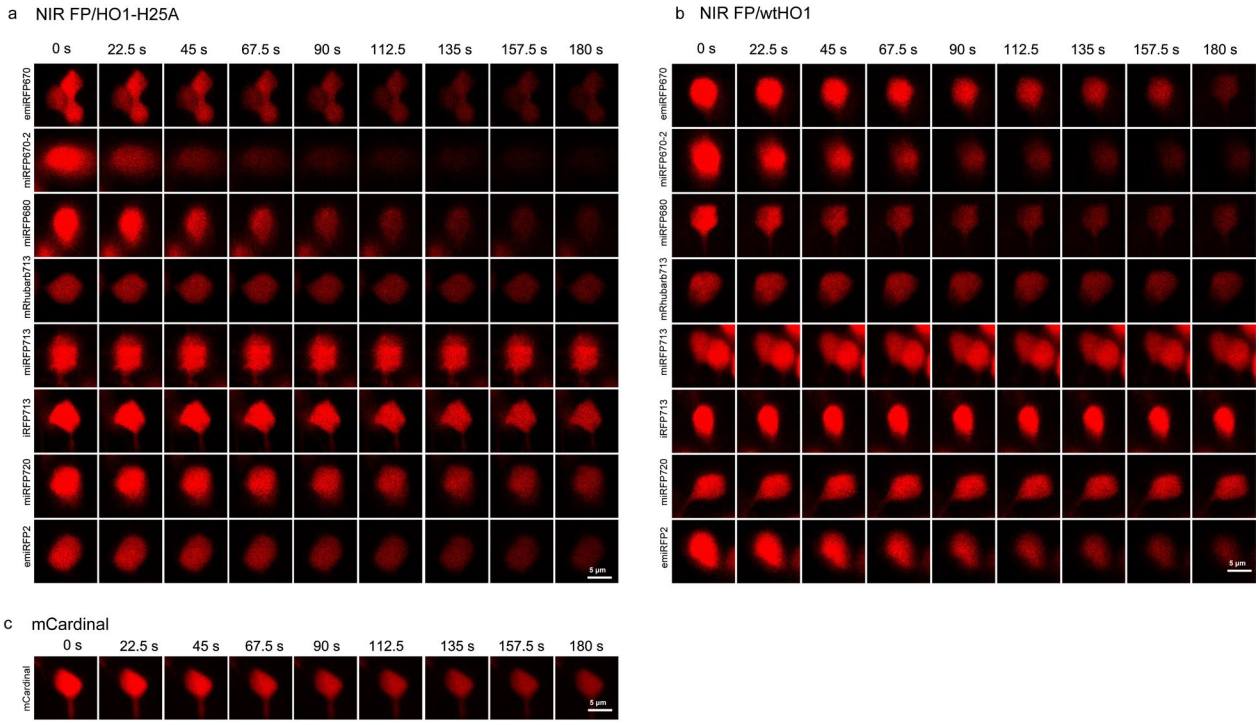

(**a**) Representative time series images of neurons co-expressing selected NIR FPs with an inactive variant of HO1 (HO1-H25A) in spinal cord neurons under continuous confocal illumination (n=40 neurons from 4 fish for each protein). (**b**) Representative time series images of neurons co-expressing selected NIR FPs with wild-type HO1 (wtHO1) in spinal cord neurons under continuous confocal illumination (n=40 neurons from 4 fish for each protein). (**c**) Representative time series images of neurons expressing mCardinal without HO1 expression in spinal cord neurons under continuous confocal illumination (n=40 neurons from 4 fish). Imaging conditions: Leica SP8 with a 40x NA1.1; cfCy5-LP, excitation 633 nm at 70% laser power, emission 645-780 nm. The same dynamic range was used for all single plain images (Fiji software). Scale bars, 5 µm.

Supplementary Figure 18. Co-expression of the selected NIR FPs with mNeonGreen in neurons in *C. elegans*.

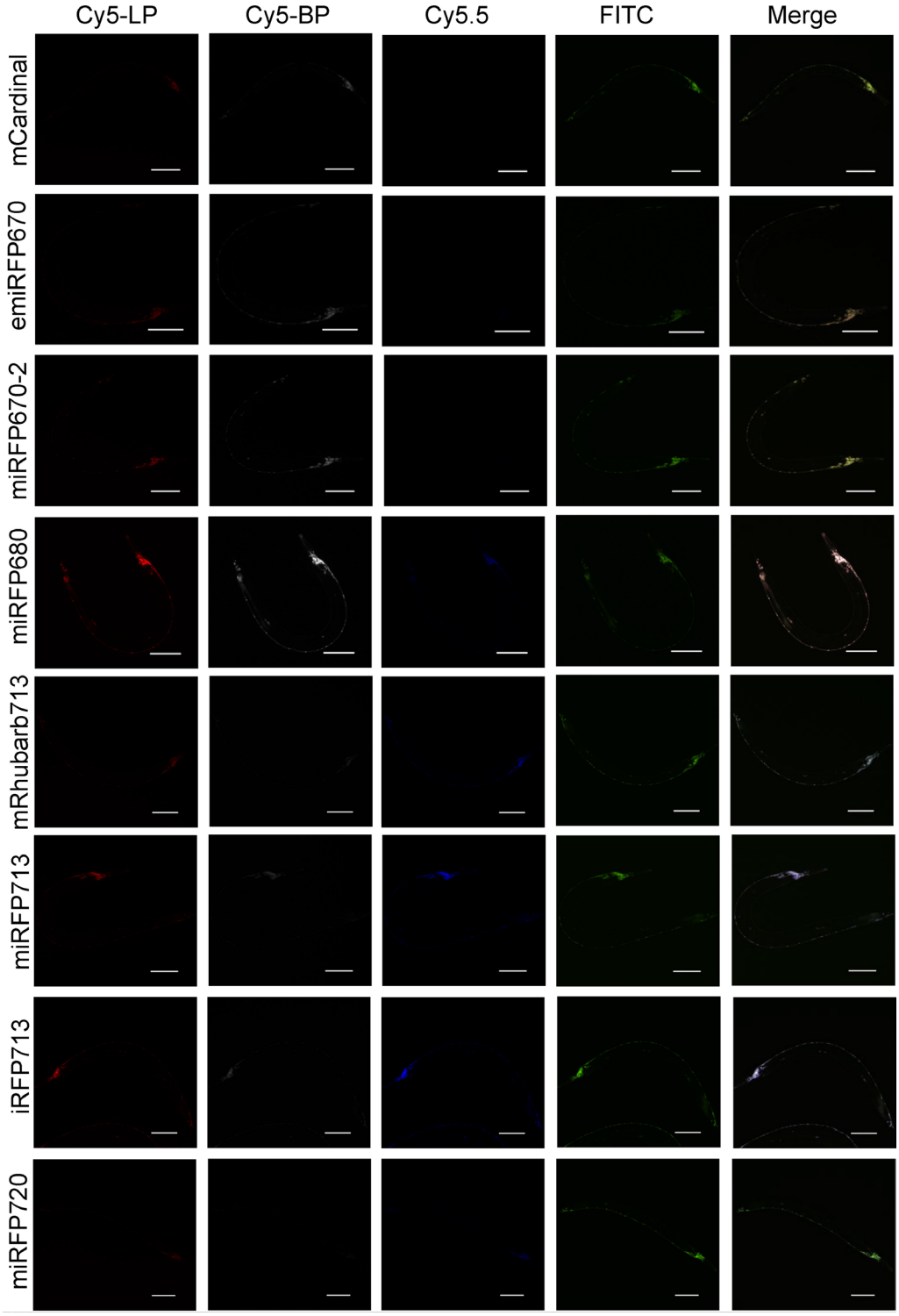

Representative wide-field fluorescence images of *C. elegans* at L4 stage co-expressing selected NIR FPs with mNeonGreen in neurons (n=30 worms for each protein in each channel). All images for the same channel are presented with the identical LUT settings; images were generated through maximum projection. Scale bars, 50 μm.

Supplementary Figure 19. Dual-color NIR imaging in live HeLa cells.

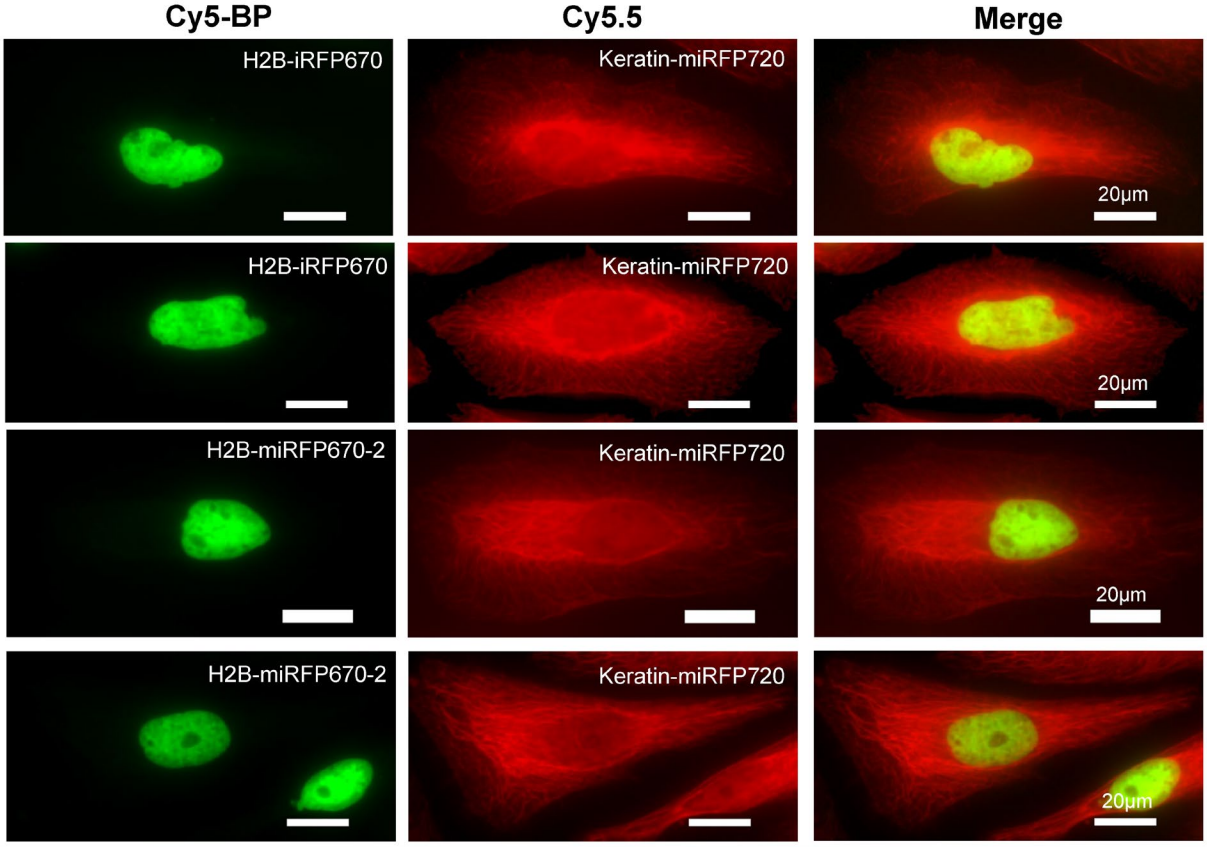

Dual color imaging of fixed HeLa cells co-expressing H2B-iRFP670/keratin-miRFP720 and H2B-miRFP670-2/keratin-miRFP720. Imaging conditions for Cy5-BP: excitation 635/22 nm, emission 679/41 nm; for Cy5.5: excitation 680/13 nm, emission 710LP; n=30 cells from 2 independent transfections. Dynamic range was adjusted independently for each channel to facilitate visualization; images were generated through maximum projection. Slight crosstalk was observed in both channels regardless of the protein pair. Scale bars, 20 μm.

Supplementary Figure 20. Validation of Rapalink-1 for induction of autophagy in PCs of larval zebrafish.

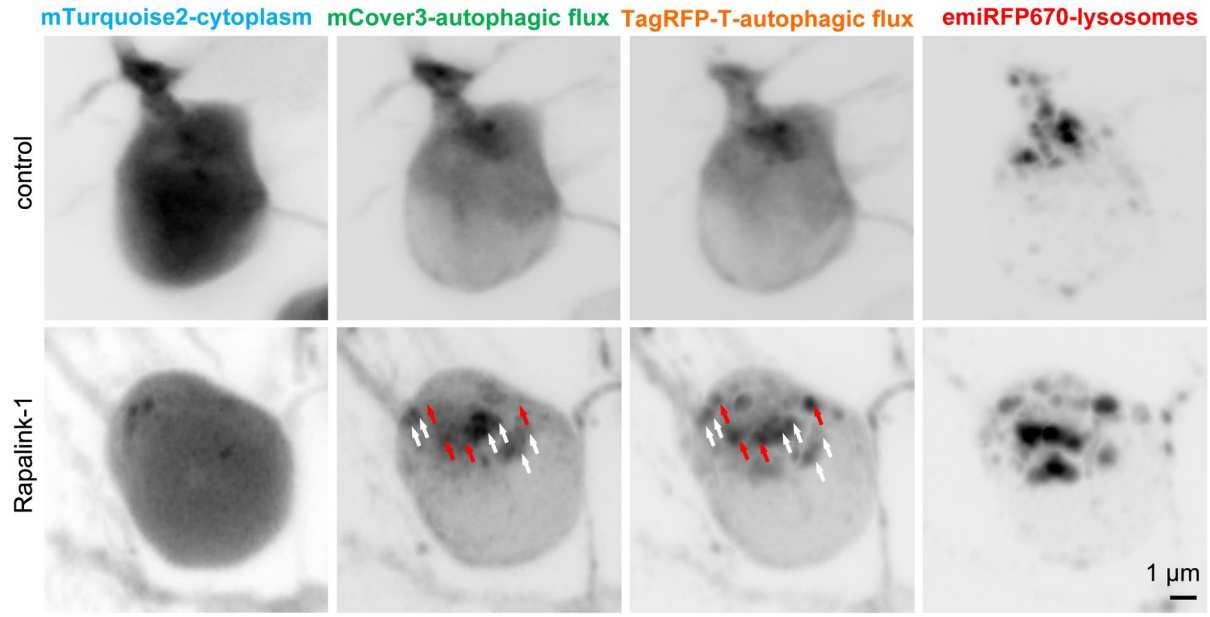

Imaging of autophagy-lysosomal vesicles in cerebellar Purkinje cell (PC) expressing lysosomal membrane protein LAMP1 fused to emiRFP670, cytoplasmic mTurqoise2, and autophagic flux sensor, TagRFP-T-mClover3LC3 identifying mClover3^{+}/TagRFP-T^{+} autophagosome and mClover3^{-}/TagRFP-T^{+} autolysosome. (Upper) images show 4 dpf zebrafish PC expressing cytoplasmic mTurquoise2 (left, cyan channel), TagRFP-T-mClover3 LC3 (2nd, and 3rd from left, green, and red channels, respectively), and Lamp1-emiRFP670 (right, NIR channel) (n=8 fish). (Lower) When the zebrafish larva was treated with an mTOR inhibitor, Rapalink-1 (1.5μM) for 4 h, TagRFP-T-mClover3 LC3 signals in PC are significantly increased in numbers of autophagosomes (mClover3^{+}/TagRFP-T^{+}, white arrows) and autolysosomes (mClover3^{-}/ TagRFP-T^{+}, red arrows) (2nd and 3rd from left), indicating an autophagic flux enhancement in this neuron (n=8 fish). Imaging conditions: ZEISS LSM 880 with Airyscan, cyan, excitation 405 nm, emission BP465-505 and LP 525 nm; green 488 nm; emission: BP495-550nm + LP 570nm; red, excitation: 561 nm, emission BP570-620nm + LP 645nm; NIR, excitation 633 nm, emission BP570-620nm + LP 645nm. Each image was processed directly using the Zeiss Airyscan image processing algorithm in the Zen black software (linear deconvolution with the Wiener filter and alignment of each offset detector to the central element). Z-stack projected images were generated, followed by adjusting the dynamic range independently. Scale bar, 1 μm.

Supplementary Figure 21. Synaptic labeling of PCs in larval zebrafish.

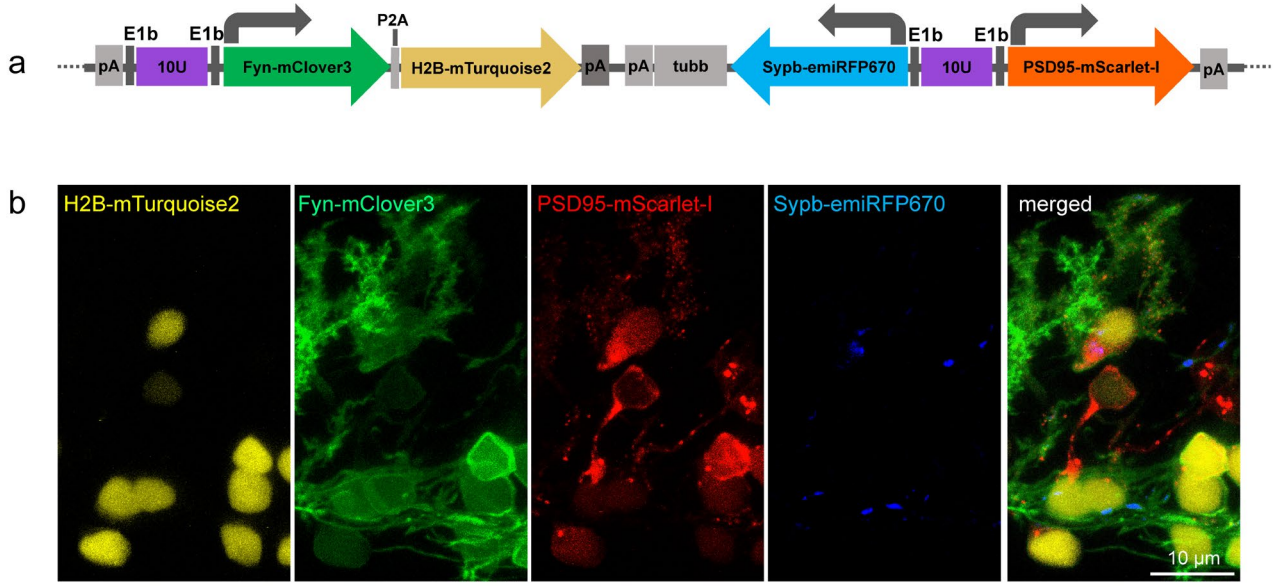

(**a**)Schematic representation of the expression cassette used for co-expression of four reporters: H2B-mTurquoise2, Fyn-mClover3, PSD95-mScarlet-I, and Synaptophysin b (Sypb)-emiRFP670 (see **Methods** section for the details of the vector design). (**b**) Representative overview images of 5 dpf zebrafish cerebellar Purkinje cells (PCs) expressing Sypb fused to emiRFP670 (blue) together with three additional fluorescent reporters labeling nucleus (H2B-mTurqoise2, yellow), plasma membrane (Fyn-mClover3, green), and excitatory post-synapses (PSD95-mScarlet-I, red) (n=8 fish). Signals of PSD95-mScarlet-I (red) are colocalized with Fyn-mClover3 (green) in the dendritic spine structure, whereas the synaptic vesicles labeled with Sypb-emiRFP670 (blue) are transported along the axons of PCs. Imaging conditions: Leica SP8; cyan, excitation 405 nm, emission 421-482 nm; green, excitation: 488 nm, emission 496-530 nm; red, excitation 561 nm, emission 570-616 nm; NIR, excitation 633 nm, emission 645-780 nm. Z-stack projected images were generated and dynamic range was adjusted independently for each image from 4 different channels. The images were further processed to show their signals detected in 4 different channels as different colors (Fiji software).
Scale bar, 10 µm.

References

1. Babakhanova, S. *et al.* Rapid directed molecular evolution of fluorescent proteins in mammalian cells. *Protein Sci.* **31**, 728–751 (2022).
2. Filonov, G. S. *et al.* Bright and stable near-infrared fluorescent protein for in vivo imaging. *Nat. Biotechnol.* **29**, 757–761 (2011).
3. Piatkevich, K. D. K. D. *et al.* Near-Infrared Fluorescent Proteins Engineered from Bacterial Phytochromes in Neuroimaging. *Biophys. J.* **113**, 2299–2309 (2017).
4. Matlashov, M. E. *et al.* A set of monomeric near-infrared fluorescent proteins for multicolor imaging across scales. *Nat. Commun.* **11**, (2020).
5. Babakhanova, S. *et al.* Rapid Directed Molecular Evolution of Fluorescent Proteins in Mammalian Cells. *bioRxiv* 2021.08.02.454744 (2021) doi:https://doi.org/10.1101/2021.08.02.454744.
6. Costantini, L. M., Fossati, M., Francolini, M. & Snapp, E. L. Assessing the Tendency of Fluorescent Proteins to Oligomerize Under Physiologic Conditions. *Traffic* **13**, 643–649 (2012).